

UCSF

UC San Francisco Electronic Theses and Dissertations

Title

Studying the Accessory Proteins and Functions of Viruses that Interact with the Host Innate Immune System

Permalink

<https://escholarship.org/uc/item/1w04m53m>

Author

Ary, Beatrice Elisabeth

Publication Date

2022

Peer reviewed|Thesis/dissertation

Studying the Accessory Proteins and Functions of Viruses that Interact with the Host
Innate Immune System

by
Beatrice Ary

DISSERTATION
Submitted in partial satisfaction of the requirements for degree of
DOCTOR OF PHILOSOPHY

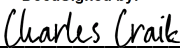
in

Chemistry and Chemical Biology

in the

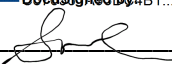
GRADUATE DIVISION
of the
UNIVERSITY OF CALIFORNIA, SAN FRANCISCO

Approved:

DocuSigned by:

6F8EED39591F4A0... Charles Craik
Chair

DocuSigned by:

John Gross

DocuSigned by:

8BD0E7DC6FB141A... Seemay Chou

Committee Members

Dedication

I dedicate this thesis to my partner Christian Omar Figueroa Ocasio and our three cats Nia, Ella and Katya for providing constant love, encouragement, and simultaneous distraction.

Acknowledgements

This thesis would not have been possible without the significant support of my many mentors, friends, and family. I would like to thank my thesis advisor Charly Craik who continually paved the way for me to follow my passion of studying virology and collaborating with many other labs at UCSF in pursuit of this training. Your unflagging enthusiasm through my many projects and a global pandemic enabled me to press on in challenging projects and entirely new fields. I will treasure my time and experiences at UCSF both pre and post pandemic. However, I will probably most especially cherish my research during the early pandemic when the Craik lab came together under Charly's leadership and were able to accomplish so much in a foreign field of virology and add to the global understanding of a new disease. Your undying optimism taught me to continually look for the fun in science and appreciate the opportunity to try many new techniques and to never stop learning.

I would like to thank my thesis committee members Dr. John Gross and Dr. Seemay Chou for providing their great minds to bounce ideas off and refocusing me on the big picture of my projects. I did not come to either of you enough and I encourage all my fellow graduate students to communicate more often with their thesis committee.

I must thank many Craik Lab alumni and current members for their help and advice on a daily basis. I would like to thank Markus Bohn for teaching me that the best thing to do on a Friday is run a gel and for always balancing out my mood, not to mention his superior taste in coffee and beer. I would like to thank Andre Luis Pinedo Lourenco for reminding me of the importance of cordiality and taking time to engage with the human and not only the science. I would like to thank Natalia Sevillano, Jennifer Binning, Koli Basu, and Dong Hee Chung for their experimental training, advice and their problem-solving over coffee. I would like to thank

my lab mate Peter Rohweder for being on this journey with me from the beginning and always offering a shoulder to suffer together. His knowledge and appreciation of reality TV is unrivaled.

I need to especially thank my rotation mentee Emily Connelly for teaching me so much more than I taught her and pushing me to follow my passions in virology. I owe her a lifetime of boba and baked goods that I plan on repaying.

Much of my thesis would not have been possible without the support, training, and input of Dr. David Gordon now at Emory University. His passion for science and work ethic in pursuit of good data continues to inspire me.

I must also thank my parents and brother for their emotional support and advice from their experiences of navigating academia. I need to thank my dad especially for always asking the important questions. My ride or die colleagues Gracie Gordon, Kaitlyn Tsai, Taylor Arhar, Lisa Kirkemo, and Susanna Elledge got me through many a trying time and always gave me an outlet for my frustration at science. Finally, I would like to thank my boyfriend Christian Omar Figueroa Ocasio. While he has not always understood the specifics of my challenges, he has always appreciated the difficulty. He has also indulged my love of animals in quarantine which greatly aided my mental health. I admire his self-discipline and benefit from his laser focus. Perhaps a thesis can be completed without feline companions but I do not wish to find out.

Contributions

Several chapters of this thesis contain material from previously published work. They do not represent the final published forms and have been edited slightly.

Chapter 1

The work discussed in Chapter 1 was based off the experimental efforts of Dr. Ruth Hüttenhain and Dr. Braden Lobingier who provided significant input and guidance. Dr. Jennifer Binning, Dr. Markus Bohn, Dr. Xi Liu, and Dr. Jiewei Xu provided training in protein production, cell culture, and fluorescence polarizations assays.

Chapter 2

Dr. Cathal Mahon began this project and did the initial experimental work shown in figure 1 and 2 of this work. Dr. Oliver Julien preformed the N-terminomics experiment in table supplemental 1. Dr. Markus Bohn, Dr. David Gordon, Emily Connelly, Michael McGregor, Dr. Mauricio Montano aided in the progress and training of cell culture, HIV infection, and work in BSL3.

Chapter 3

This work was done in collaboration with Dr. Markus Bohn, Nicholas Young, and Conner Bardine. Design and production of the SARS-CoV-2 Replicon was done in collaboration with Emily Connelly.

Chapter 4 of this dissertation is a reprint of a previous publication:

Boyce, J. H., Dang, B., **Arv, B.**, Edmondson, Q., Craik, C. S., DeGrado, W. F., Seiple, I. B. Platform to Discover Protease-Activated Antibiotics and Application to Siderophore–Antibiotic Conjugates. *Journal of the American Chemical Society* **2020** *142* (51), 21310-21321. DOI: 10.1021/jacs.0c06987.

B. A. performed initial studies of research and developed and consulted on the research plan. J. H. B. conceived the research, designed and performed experiments, analyzed data, and wrote the manuscript.

Chapter 5 of this dissertation is a reprint of a previous publication:

Asarnow, D., Wang, B., Lee, W.H., Hu, Y., Huang, C.W., Faust, B., Ng, P.M.L., Ngoh, E.Z.X., Bohn, M., Bulkley, D., Pizzorno, A., **Ary, B.**, Tan, H.C., Lee, C.Y., Minhat, R.A., Terrier, O., Soh, M.K., Teo, F.J., Yeap, Y.Y.C., Seah, S.G.K., Chan, C.E.Z., Connelly, E., Young, N.J., Maurer-Stroh, S., Renia, L., Hanson, B.J., Rosa-Calatrava, M., Manglik, A., Cheng, Y., Craik, C.S., Wang, C. Structural insight into SARS-CoV-2 neutralizing antibodies and modulation of syncytia, *Cell* (2021), doi: <https://doi.org/10.1016/j.cell.2021.04.033>.

B. A. expressed and purified proteins in mammalian expression systems for determination of the spike-antibody structure by Cryo-EM. B. A. expressed and purified spike (S) protein from ExpiCHOs. B.A. expressed and purified recombinant Fabs and IgGs of 5A6, 3D11, and 2H4 from Expi293s. D. A. and B. L. W. cowrote the manuscript. D. A. performed structural analysis of the Cryo-EM data. B. L. W. performed the biopanning to isolate 5A6, 3D11, and 2H4 antibodies and the pseudovirus neutralization and cell-cell fusion assays.

Studying the Accessory Proteins and Functions of Viruses that Interact with the Host

Innate Immune System

By Beatrice Ary

Abstract

Cells have evolved proteins that detect foreign DNA, RNA, or proteins which then activate cellular pathways to combat bacterial or viral infection.¹⁻⁴ Apolipoprotein B editing complex 3 (APOBEC3 or A3) is a host cytidine deaminase that deaminates cytidine to uridine in viral DNA in the cytoplasm causing hyper G→A mutation leading to destabilization and degradation of the viral genome.⁵⁻⁸ HIV viral infectivity factor (vif) has evolved to regulate A3 degradation of viral DNA.⁹ Vif hijacks host ubiquitination machinery to degrade A3s and prevent packaging of A3 into the viral particle.^{10,11} Vif hijacks the cotranscription factor core factor binding unit b (CBF-β), Elongin B (ELOB) and Elongin C (ELOC) to form the VCBC complex.¹²⁻¹⁵ VCBC binds A3s and Cullin 5 (Cul5) for ubiquitination and degradation of A3 thereby preventing packaging.^{12,16} Antigen binding fragments (Fabs) were generated against VCBC using a naïve B-cell Fab phage display library to isolate biological tools that are specific for the host-virus interaction.¹⁷ Two high affinity Fabs were found to bind at distinct epitopes on VCBC and produced distinct phenotypes when expressed in cells as single chain variable fragments (scFvs).¹⁷ The Fab 3C9 shields A3F from ubiquitination and restores packaging of A3F into the viral particle. The Fab 1D1 blocks binding of Cul5 and ubiquitination *in vitro*. The scFv 1D1 prevented ubiquitination of A3F but did not restore packaging. Affinity purification mass spectroscopy (AP-MS) in HEK293Ts with 3C9 scFv and 1D1 scFv showed different interactomes in the presence of vif. AP-MS with 1D1 scFv did not interact with CBF-β.

TABLE OF CONTENTS

CHAPTER 1	1
UNDERSTANDING THE INTERACTION OF VIF AND APOBEC3F	1
1.1 ABSTRACT	2
1.2 INTRODUCTION	3
1.3 RESULTS	5
<i>1.3.1 Cul5 binding to VCBC does not change A3F binding affinity</i>	5
<i>1.3.2 AP-MS with 1D1 and 3C9 reveal different PPIs</i>	6
<i>1.3.3 Establishment of 3C9-scFv and 1D1-scFv HEK293T cell lines</i>	7
1.4 DISCUSSION	8
1.5 MATERIALS AND METHODS	10
1.6 REFERENCES	17
CHAPTER 2	23
DETERMINING THE EFFECTS OF HIV PROTEASE CLEAVAGE OF HOST PROTEINS	23
2.1 ABSTRACT	24
2.2 INTRODUCTION	24
2.3 RESULTS	27
<i>2.3.1 Identifying possible interactions between host proteins and HIV PR</i>	27
<i>2.3.2 Evaluation of HIV PR Substrates in HEK293Ts</i>	29
<i>2.3.3 HIV proteolytic activity in CD4⁺ T cells</i>	29
<i>2.3.4 HIV Proteolytic Activity During Latency in J-Lat10.6 cells</i>	30
<i>2.3.5 Reduced Co-localization of KAP1 with HPIγ</i>	31

2.4 DISCUSSION	31
2.5 MATERIALS AND METHODS.....	33
2.6 REFERENCES	45
CHAPTER 3	49
DEVELOPMENT OF SARS-COV-2 MAJOR PROTEASE PRODUCTION AND REPLICON	49
3.1 ABSTRACT	50
3.2 INTRODUCTION	50
3.3 RESULTS.....	52
3.3.1 Development and production of highly active recombinant Mpro.....	52
3.3.2 SARS-CoV-2 Replicon Development	53
3.4 DISCUSSION	54
3.5 MATERIALS AND METHODS.....	56
3.6 REFERENCES	61
CHAPTER 4	63
PLATFORM TO DISCOVER PROTEASE-ACTIVATED ANTIBIOTICS AND APPLICATION TO SIDEROPHORE–ANTIBIOTIC CONJUGATES	63
4.1 ABSTRACT	64
4.2 INTRODUCTION	64
4.3 RESULTS.....	68
4.3.1 Substrate Phage Display Leads to WSPKYM-RFG and WSWC-KWASG for Periplasmic Cleavage.....	68
4.3.2 WSPKYM Conjugates Are Efficiently Cleaved without a P' Peptide.....	70

4.3.3 Design and Synthesis of SACs That Incorporate Solithromycin, Daptomycin, and Eperezolid-NH ₂	71
4.3.4 Determination of the Antibacterial Activity of SACs 7–9 and Iron-Dependent Activity.	73
4.3.5 Oxazolidinone Conjugate 8 Was Active against <i>E. coli</i> Δ bamB Δ tolC (Table 4.3).....	74
4.3.6 Daptomycin Conjugate 7 Exhibits High Activity against <i>Acinetobacter</i> Species (Table 4.4)....	76
4.4 DISCUSSION	78
4.5 MATERIALS AND METHODS	80
4.6 REFERENCES	92
CHAPTER 5	114
STRUCTURAL INSIGHTS INTO ANTIBODY INHIBITION OF SARS-COV-2 INFECTIVITY AND SYNCYTIA FORMATION	114
5.1 ABSTRACT	115
5.2 INTRODUCTION	115
5.3 RESULTS	117
5.3.1 Isolation of SARS-CoV-2 receptor-blocking antibodies from a naïve human library.....	117
5.3.2 SARS-CoV-2 neutralization by receptor blocking antibodies	118
5.3.3 Neutralizing antibodies inhibit or enhance Spike-mediated cell fusion	120
5.3.4 Structures of Spike-Fab complexes.....	121
5.3.5 2H4 is an orthosteric receptor-mimetic antibody.....	121
5.3.6 3D11 allosterically blocks ACE2 binding and triggers Spike opening	122
5.3.7 5A6 traps a pre-fusion conformation to inhibit spike-mediated fusion	123
5.4 DISCUSSION	125
5.5 MATERIALS AND METHODS	128
5.6 REFERENCES	160

LIST OF FIGURES

FIGURE 1.1 VIF HOST COMPLEX	11
FIGURE 1.2 3D NEGATIVE STAIN EM RECONSTRUCTION SHOWS FAB BINDING SURFACES ON VCBC COMPLEX.....	11
FIGURE 1.3 FLUORESCENCE ANISOTROPY OF VCBC AND CUL5 WITH FLUORESCIN TAGGED A3F.	12
FIGURE 1.4 AP-MS OF scFVs IN HEK293Ts WITH VIF.	12
FIGURE 1.5 APEX BIOTINYLATION PROTOCOL.....	13
FIGURE 1.6 BIOTINYLATION CONTOUR MAP OF THE CYTOPLASM.	13
FIGURE 1.7 GENERATION OF STABLE HEK293T scFV CELL LINES.....	14
FIGURE 2.1 THE VIRAL LIFECYCLE OF HIV-1.	38
FIGURE 2.2 IDENTIFICATION OF HIV PROTEASE INTERACTIONS WITH HOST PROTEINS.	39
FIGURE 2.3 HOST SUBSTRATE CLEAVAGE BY HIV PR IN HEK293Ts.....	40
FIGURE 2.4 EXPERIMENTAL SETUP FOR INDUCING HIV PROTEASE IN JURKAT CELLS.	41
FIGURE 2.5 SUBTILIGASE N-TERMINOMICS OF HIV PROTEASE SUBSTRATES.	41
FIGURE 2.6 EXPERIMENTAL DESIGN OF CD4 ⁺ T CELL INFECTION AND SORTING.	42
FIGURE 2.7 EVALUATION OF HOST SUBSTRATE DEGRADATION IN CD4 ⁺ T CELLS.	42
FIGURE 2.8 EVALUATION OF ENDOGENOUS HOST SUBSTRATE DEGRADATION IN J-LAT10.6.....	43
FIGURE 2.9 COLOCALIZATION OF KAP1 AND HP1G DURING REACTIVATION OF HIV IN J-LAT10.6.....	44
FIGURE 3.1 MPRO EXPRESSION CONSTRUCTS AND ACTIVITY	58
FIGURE 3.2 EXPRESSION AND PURIFICATION OF DIFFERENT MPRO CONSTRUCTS.....	58

FIGURE 3.3 DESIGN OF FOUR SARS-CoV-2 REPLICON RNA CONSTRUCTS.	59
FIGURE 3.4 SARS-CoV-2 DNA TRANSCRIPT ASSEMBLY AND IVT TRIALS.	59
FIGURE 3.5 GFP POSITIVE VERO E6 CELLS AND RT-QPCR OF BULK RNA AND GENOMIC DNA. .	60
FIGURE 4.1 PLATFORM TO DISCOVER PROTEASE ACTIVATED ANTIBIOTICS.	88
FIGURE 4.2 PROTEASE CLEAVAGE OF ACC PEPTIDE IN PERIPLASMIC EXTRACT.	88
FIGURE 4.3 COMPARISON OF INHIBITION OF BACTERIAL TRANSLATION BY SEVERAL CONJUGATES.	89
FIGURE 5.1 ISOLATION OF SARS-CoV-2 RECEPTOR-BLOCKING ANTIBODIES FROM A NAÏVE HUMAN LIBRARY	141
FIGURE 5.2 SARS-COV-2 NEUTRALIZATION BY RECEPTOR BLOCKING ANTIBODIES.	142
FIGURE 5.3 ANTI-SARS-CoV-2 SPIKE RBD IGG ANTIBODIES AFFECT TRYPSIN INDUCED CELL SYNCYTIA FORMATION.	144
FIGURE 5.4 STRUCTURES OF SPIKE-FAB COMPLEXES	145
FIGURE 5.5 BINDING MODE AND EPITOPE OF 5A6.....	146
FIGURE 5.6 SPIKE FUNCTIONAL MODULATION BY RECEPTOR-BLOCKING ANTIBODIES	147
FIGURE 5.7 BLOCKING OF ACE2/SARS-CoV-2 RBD INTERACTION BY 1F4, 2H4, 3D11, 3F11, 5A6 AND 6F8 IGGs TESTED BY COMPETITION ELISA.	148
FIGURE 5.8 BINDING AVIDITY OF 1F4, 2H4, 3D11, 3F11, 5A6 AND 6F8 IGG ANTIBODIES TO SARS-CoV-2 SPIKE RBD PROTEINS TESTED BY ELISA.	148
FIGURE 5.9 BINDING AFFINITY OF FIVE FAB CLONES TO SARS-CoV-2 SPIKE RBD PROTEIN MEASURED BY BIOLAYER INTERFEROMETRY.	149
FIGURE 5.10 BINDING AVIDITY OF SIX IGGs TO THE RBD BY BIOLAYER INTERFEROMETRY.	150

FIGURE 5.11 THE POTENCY OF 2H4, 3D11 AND 5A6 IgG ANTIBODIES IN NEUTRALIZING LIVE SARS-CoV-2 VIRUS ASSAYS DETERMINED BY MEASURING THE VIRAL GENOME COPY NUMBER (GCN).	151
FIGURE 5.12 CRYO-EM DENSITIES AND RESOLUTION ESTIMATION	153
FIGURE 5.13 ADDITIONAL STRUCTURAL DETAILS.....	154
FIGURE 5.14 CRYO-EM PROCESSING.....	156
FIGURE 5.15 ANTIBODY BINDING TO SPIKE TRIMER MEASURED BY SURFACE PLASMON RESONANCE.	158
FIGURE 5.16 NEUTRALIZATION OF THE SARS-CoV-2 PSEUDOVIRUS WITH SPIKE MUTANT D614G.....	159

LIST OF TABLES

TABLE 1.1 AP-MS PULLDOWN WITH VIF AND 3C9 scFv IN HEK293Ts.	15
TABLE 1.2 AP-MS PULLDOWN WITH VIF AND 1D1 scFv IN HEK293Ts.	16
TABLE 4.1 HIGHLY ENRICHED SEQUENCES FOUND THROUGH SUBSTRATE PHAGE DISPLAY.....	89
TABLE 4.2 MODULAR SYNTHETIC PLATFORM FOR SAC SYNTHESIS.	90
TABLE 4.3 ANTIBACTERIAL ACTIVITY (MIC IN mM) AND IN VITRO CLEAVAGE OF EPEREZOLID-NH ₂ CONJUGATE 8 AND DERIVATIVES THEREOF.	91
TABLE 4.4 ANTIBACTERIAL ACTIVITY (MIC IN mM) OF DAPTOMYCIN SAC 7 AND DERIVATIVES THEREOF.	91

Chapter 1

Understanding the Interaction of Vif and APOBEC3F

1.1 Abstract

Cells have evolved proteins that detect foreign DNA, RNA, or proteins which then activate cellular pathways to combat bacterial or viral infection.¹⁻⁴ Apolipoprotein B editing complex 3 (APOBEC3 or A3) is a host cytidine deaminase that deaminates cytidine to uridine in viral DNA in the cytoplasm causing hyper G→A mutation leading to destabilization and degradation of the viral genome.⁵⁻⁸ HIV viral infectivity factor (vif) has evolved to regulate A3 degradation of viral DNA.⁹ Vif hijacks host ubiquitination machinery to degrade A3s and prevent packaging of A3 into the viral particle.^{10,11} Vif hijacks the cotranscription factor core factor binding unit b (CBF-β), Elongin B (ELOB) and Elongin C (ELOC) to form the VCBC complex.¹²⁻¹⁵ VCBC binds A3s and Cullin 5 (Cul5) for ubiquitination and degradation of A3 thereby preventing packaging.^{12,16} Antigen binding fragments (Fabs) were generated against VCBC using a naïve B-cell Fab phage display library to isolate biological tools that are specific for the host-virus interaction.¹⁷ Two high affinity Fabs were found to bind at distinct epitopes on VCBC and produced distinct phenotypes when expressed in cells as single chain variable fragments (scFvs).¹⁷ The Fab 3C9 shields A3F from ubiquitination and restores packaging of A3F into the viral particle. The Fab 1D1 blocks binding of Cul5 and ubiquitination *in vitro*. The scFv 1D1 prevented ubiquitination of A3F but did not restore packaging. Affinity purification mass spectroscopy (AP-MS) in HEK293Ts with 3C9 scFv and 1D1 scFv showed different interactomes in the presence of vif. AP-MS with 1D1 scFv did not interact with CBF-β, an important component of the VCBC complex. Spatial and temporal elucidation of proteins interacting with the complex will further determine events effecting viral infectivity.

1.2 Introduction

Since the discovery of human immunodeficiency virus (HIV) as the causative agent of acquired immune deficiency syndrome (AIDS) an immense amount of research has been dedicated to understanding how the virus antagonizes the immune response of the human host. The HIV RNA genome encodes 15 viral proteins to attach, invade, and replicate in host immune cells.¹⁸ HIV viral infectivity factor (vif) has evolved to regulate A3 degradation of viral DNA by hijacking host ubiquitination machinery to degrade A3s and prevent packaging of A3 into the viral particle (**Figure 1.1**).^{10,15} A3s are known to also prevent integration of viral DNA into the host genome and prevent latency.^{19,20} In addition to this mechanism vif has alternate functions that regulate host machinery but the most significant impact on host restriction by the viral accessory protein is the degradation of the A3 family of host restriction factors.

Vif hijacks the CBF- β , which stabilizes RUNX1 for important transcriptional regulation of A3s on chromosome 22.¹³⁻¹⁵ The ability of vif to prevent A3 packaging is extremely important to viral proliferation. This is supported by the reduction in viral infectivity by 97% due to A3 activity in the absence of vif.⁵ The importance of maintaining vif-A3 interaction is also evidenced by the positive selection seen in evolution of both host and viral proteins, conservation of vif in other lentiviruses, and reduced disease severity in HIV infected individuals because of A3 expression profiles.^{2,9,21,22} Vif is a 23 kDa protein that has at least six protein binding domains.²³ Exposure or reorientation of vif binding domains in the VCBC complex could change vif's ability to bind A3 and prevent packaging.^{11,24}

Recombinant Fabs can be generated against specific conformations of a protein or protein complexes that are interesting in specific cellular conditions. Fabs were generated against VCBC using a naïve B-cell phage display library to isolate biological tools that are specific for the host-

virus interaction.¹⁷ The 1D1 scFv showed that binding near the vif-ELOC interface served to regulate VCBC interaction in a similar way as dominant negative mutations that inactivate ubiquitination activity of Cul5, Cullin 2 (Cul2), and ELOC.^{15,17,25,26} The study of VCBC and its interactions have not elucidated how vif is able to regulate A3 packaging without degrading A3s. Protein interactions at this interface clearly regulate packaging, but the mechanism has not been determined from the crystal structure of VCBC, mutational studies of vif and A3s, or interactome studies.^{9,12,14,16,27}

Interactome studies have produced different lists of interaction partners by isolating vif protein complexes in T cell lines and primary T cells.^{12,27,28} These studies have used AP-MS which is limited to identification of stable protein complexes.^{12,29} Inconsistencies in vif protein sequence and differential expression of innate immune factors in different cell lines adds to difficulty with validation of interaction partners.⁷ Consolidation of interactome lists through validation has resulted in the current model of vif-A3 interaction.^{8,13}

APEX is a genetically engineered ascorbate peroxidase from soybeans developed by the Ting lab.³⁰ AP-MS can capture the biological time frame of protein interactions or subcellular localization if used in conjunction with subcellular fractionation.^{29,31} APEX has been used to label the proteomes of organelles, generate contour maps of cellular compartments, parse transient PPIs, and in electron microscopy.^{31,32} APEX is a 27 kDa protein similar in size to GFP, a tag of this size will be tolerated by most proteins but the folding and function of smaller proteins may be affected.³⁰ Viral proteins like vif have been especially intolerant of modifications because they need to make use of their entire protein sequence and adopt many conformations to have maximal multifunctionality.^{21,33}

The biotinylation of proteins by APEX has been manipulated by the Ting lab to utilize biotin phenol within seconds of exposure to H₂O₂. The scFv-APEX construct will be cotransfected with vif and A3 into HEK293 cells prior to a 30-minute incubation with biotin phenol (fig. 4). The labeling of proteins by APEX is catalyzed by the addition H₂O₂ for a time window of 30 seconds to 10 minutes (fig. 4).³⁴ APEX catalyzes the one electron oxidation of biotin phenol to create a short lived biotin-phenoxy radical cloud.³⁴ The biotin-phenoxy radical makes covalent adducts with electron rich side chains like tyrosines, tryptophans, histidines, and cysteines on proteins in or passing through the cloud.^{30,34} Biotinylation of proteins can be qualitatively assessed by western blot and quantitatively assessed by mass spectrometry. The data from mass spectrometry can be evaluated in a number of ways determine the temporal and spatial nature of PPIs.

1.3 Results

1.3.1 Cul5 binding to VCBC does not change A3F binding affinity.

Fluorescence polarization monitored changes in affinity between VCBC and A3F in the presence of the C-terminus of Cul5. The addition of Cul5 to the VCBC complex did not significantly alter affinity of A3F for VCBC. Changes in affinity could be induced by conformational changes of VCBC upon binding of a protein at this interface. A low resolution (~15 Å) negative stain electron microscopy (NSEM) structure with both 3C9 and 1D1 Fabs bound to VCBC did not uncover major conformational changes to VCBC upon Fab binding. Fluorescence anisotropy data show negligible differences in affinity of VCBC for A3F when bound to Cul5 (**Figure 1.2**). Further characterization of VCBC affinity and conformation in the presence of 1D1 is needed to understand whether 1D1 recapitulates phenotypes seen with the endogenous interaction partner Cul5.

1.3.2 AP-MS with 1D1 and 3C9 reveal different PPIs.

The fabs 1D1 and 3C9 specific for VCBC were converted to scFvs. ScFvs can be expressed in the reducing environment of the cell because they lack disulfide bonds.³⁷ HEK293Ts were co-transfected with 3C9 scFv and NL4-3 vif or 1D1 scFv and NL4-3 vif (**Figure 1.4**). Anti-FLAG beads were used to pulldown the 3xFLAG tagged scFvs to identify proteins in complex with the scFvs. Transfection of HEK293Ts with only the flag tagged scFvs was used for the negative control to reduce noise from the promiscuity of FLAG AP-MS.³⁸⁻⁴⁰

The 3C9 interactome directly interacts with all components of the VCBC complex CBF- β , ELOC, and ELOB in cells (**Figure 1.4**). The 3C9 scFv interacts with the E3 ubiquitin ligases Cul5 and Cul2. AP-MS with 3C9 scFv captured the essential Cul5 E3 ligase complex proteins neural precursor cell expressed developmentally down-regulated protein 8 (NEDD8) and RING domain box 1 (RBX1). NEDD8 is a ubiquitin-like protein that NEDDylates Cul5 to recruit E2s.⁴¹ RBX1 aids in poly-ubiquitination.⁴¹ 3C9 scFv also interacts with the substrate receptors Autophagy And Beclin 1 Regulator 1 (AMBRA1) and DDB1- and CUL4-associated factor 11 (DCAF11) for another E3 RING ligase Cullin 4 (Cul4).⁴² Surprisingly, 3C9 scFv interacts with Programmed Cell Death 6 Interacting Protein (ALIX) a component of ESCRT machinery for autophagy and HIV virion budding.^{42,43} Sequestosome 1 (SQSTM1) is an autophagy receptor protein that binds ubiquitin acting as a bridge for degradation of ubiquitylated proteins and the autophagosome.⁴⁴ While 1D1 scFv binds many of the same viral host components it directly interacted with different E2 and E3 ligases (**Figure 1.4**).

AP-MS with 1D1 scFv pulled down vif, ELOC, and ELOB (**Figure 1.4**). CBF- β was not identified. The absence of CBF- β may explain why expression of 1D1 scFv in cells with vif does

not allow repackaging of A3F.¹⁷ The surface area of the interaction interface of CBF- β and vif is ~4800 Å compared to the average protein interaction interface of 1200-2000 Å, CBF- β is important for stabilizing the highly disordered and flexible structure of vif.^{14,33} Interaction between 1D1 scFv and E2 ligases that possesses both E2 and E3 ligase activities like Baculoviral IAP repeat-containing protein 6 (BIRC6) and Ubiquitin-conjugating enzyme E2O (UBE2O) is interesting considering 1D1 is blocking the E3 ligase binding interface of VCBC.⁴⁵ 1D1 scFv is much smaller than Cul5 so it may not occlude the interaction of VCBC with E2/E3 ligases (**Figure 1.2**). Other studies have shown that VCBC interacts with UBE2O but this interaction does not have a significant effect on viral fitness.^{21,42} A full list of proteins identified to interact with 3C9 scFv and 1D1 scFv are include in **Table 1.1** and **Table 1.2**.

1.3.3 Establishment of 3C9-scFv and 1D1-scFv HEK293T cell lines.

To interrogate the complexity of host-virus interactions in a tractable but relevant system we designed a new labeling technology localized to VCBC by fusing APEX to our scFvs. Using scFvs that bind different epitopes will parse interactions at different sites of the VCBC complex. The n-terminus of 3C9 scFv or 1D1 scFv was attached to the C-terminus of APEX via a glycine serine linker. These constructs were cloned into a dox inducible lentiviral vector. Initial APEX labeling experiments were attempted by co-transfecting the scFvs with vif. This proved challenging because co-transfection yields about only 40% of the cell population with expression of both plasmids.^{38,46,47} In order to achieve consistent expression of the scFv-APEX construct in conjunction with vif we developed a HEK293T cell line with integrated scFv-APEX constructs. **Figure 1.7** shows the cutting of the lentiviral plasmid with restriction enzyme and transfection into HEK293Ts. The puromycin resistance gene encoded on the scFv-APEX plasmid was used

to select for HEK293T clones expressing the 3C9 or 1D1 scFV-APEX construct. The activity of the clones was tested following dox-induction (**Figure 1.5**). A dox-inducible plasmid was used to not perturb normal cellular function by constitutive expression of scFV-APEX proteins which could bind off target proteins. The function of the APEX enzyme was not effected by integration into the genome. These cell lines provide a resource to study the transient interactions of VCBC when cells are transfected with vif.

1.4 Discussion

The goal in understanding host virus interactions is to either target the virus or leverage our knowledge of host response for better treatment of disease. I attempted to understand why disruption of ubiquitination and degradation of the host antiviral factor A3F by vif does not restore the innate immune response of the host. I determined that binding of Cul5 to VCBC does not change its affinity for A3F. In future studies the HARC center would like to probe what makes binding of the scFv 1D1 to VCBC like binding events that occur with Cul5 and Cul2 using fluorescence anisotropy and crystallography.

Biochemical characterization of protein interactions *in vitro* provide significant insight into dynamics that regulate protein interactions during viral infection. However, *in vitro* reconstruction of vif-A3 interaction limits which protein interactions can be studied. While traditional AP-MS in cells has provided a broader background of the variety and complexity of host-virus interactions made by HIV vif, transient protein interactions are not identified using this method. In future we will use APEX attached to scFvs of 3C9 and 1D1 to label the components of the VCBC complex, A3s, Cul5, and Cul2, as well as transient host interactions. APEX labeling should also pick up the host factors ARIH1, ARIH2, DCAF11, and ALIX which were identified using targeted proteomics.⁴² More factors may be uncovered because VCBC will

not be disrupted by protein tags or increased expression of endogenous host factors, especially the E3 ring ligases and potentially the E2 Ub-conjugating enzymes. Biotinylation of proteins will likely be different between scFv 3C9-APEX and scFv 1D1-APEX. The 3C9-APEX construct will biotinylate all transient interactions and nearby proteins. The 1D1-APEX construct will block proteins binding at the vif-ELOC interface which is important for ubiquitination, allowing us to further investigate the distinct phenotype caused by binding of scFv 1D1.

Kaewsapsak, et al. have modified the APEX biotinylation protocol to capture RNA protein interactions (APEX-RIP).³⁶ This could have interesting application in HIV because two viral RNA genomes are packaged into the viral particle.⁴⁸ The mechanism that A3s are thought to utilize for packaging into the viral particle is to bind viral or cellular RNA for transport into the viral particle with the nucleocapsid (NC) domain of gag.^{48,49} Vif also binds RNA for packaging into the viral particle.⁵⁰ RNA binding is an important function of these proteins and may serve a functional role in preventing or enhancing ubiquitination.

Transient PPIs and RNA-protein interactions are only two thirds of the data that can be obtained from APEX labeling. A contour map created by the diffusion of biotin-phenoxyl radicals from the localized APEX can be used to create a spatial map of proteins near VCBC. The use of compartment localized comparative APEX constructs decreases background and generates a contrasting labeling gradients to create a spatial contour map.³¹ The gold standard of validation would be to knockdown or knockout identified host factors in primary T cells and test viral fitness using single cycle infectivity assays.^{28,51}

1.5 Materials and Methods

Materials, Plasmids, and Cell lines

Mammalian cells were maintained in a humidified incubator at 37°C and 5% CO₂. HEK293T cells were obtained from the American Type Culture Collection (ATCC) and grown in DMEM (Hyclone, Gibco) supplemented with 10% Fetal Bovine Serum (Hyclone, Gibco). Cells were transfected with TransIT293 from Mirus Bio.

Fluorescence Anisotropy

Proteins and buffers generously provided by the John Gross Lab at UCSF. As previously described¹⁷ vif and CBF- β and ELOC and ELOB were co-expressed in *E. coli*. The VCBC complex was reassembled in vitro and stored at -80°C. A3F 11xCTD was expressed in *E. coli* and labeled with Fluorescein. 20 μ M A3F 11xCTD labeled Fluorescein was added to a dilution series of VCBC complex or VCBC complex bound to the n-terminal domain of Cul5 from 1 nM to 75 μ M of complex. Complexes were incubated with A3F11xCTD for 20 minutes at room temperature and polarization was measured on a Analyst AD.

Expression of vif in HEK293Ts

HEK293Ts were transfected with TransIT293 purchased from Mirus Bio following their transfection protocol.

AP-MS

Following previously described protocols in brief HEK293Ts were co-transfected with scFv and vif.¹² 1×10^6 cells were harvested 48 hours after transfection and lysed in RIPA. Anti-FLAG beads were added to the sample and incubated overnight to extract 3xFLAG tagged protein. Beads were gently washed to preserve protein complexes and then prepared for mass spectroscopy.

APEX

Following previously described protocols in brief HEK293Ts were co-transfected with scFv-APEX and vif. Cells were treated with doxycycline 24 hr post transfection. H₂O₂ was added to cells and quenched after 1 or 10 minute incubations with H₂O₂.

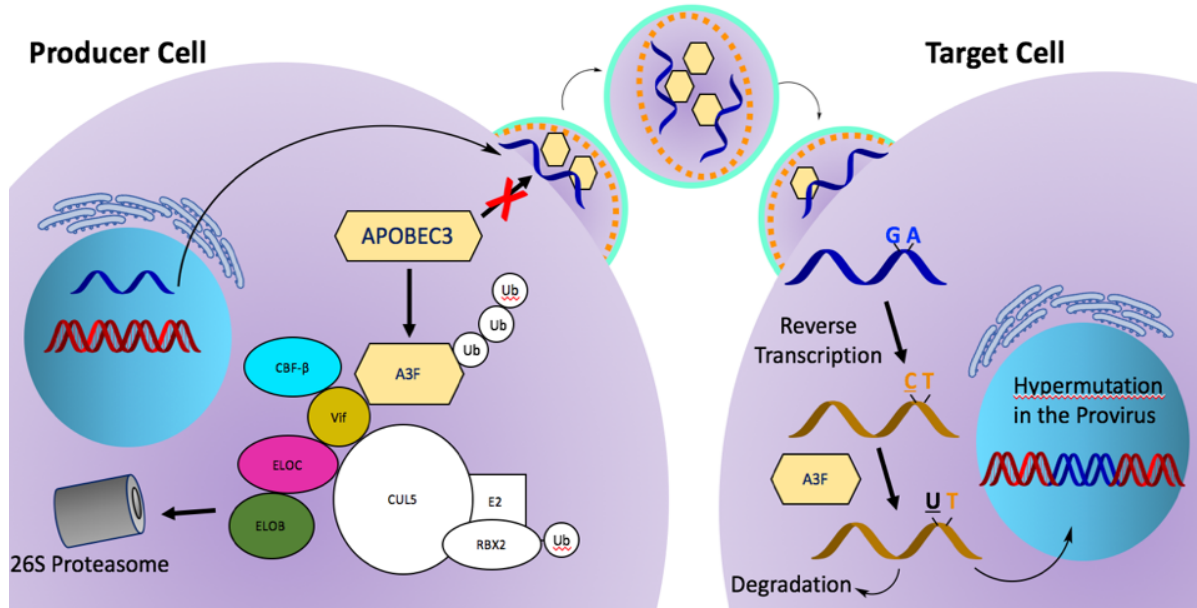


Figure 1.1| Vif Host Complex

APOBEC3 are packaged into the viral particle in the absence of vif and deaminate cytosines in the newly reverse transcribed viral DNA. This introduces numerous G → A mutations which reduces viral fitness and replication. When vif is present A3s are recruited to the VCBC complex and ubiquitinated by Cul5 for degradation by the proteasome.

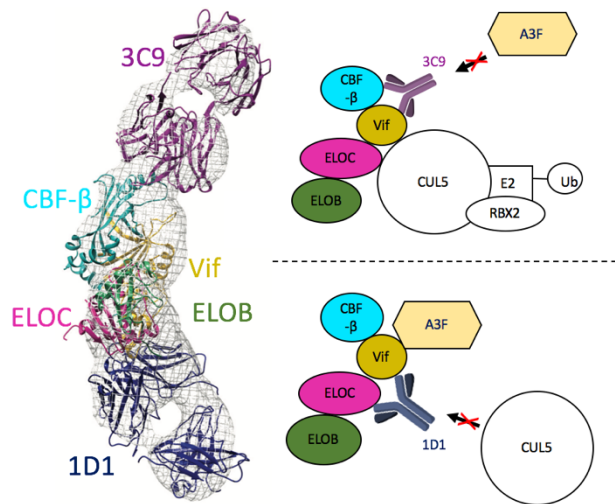


Figure 1.2| 3D negative stain EM reconstruction shows Fab binding surfaces on VCBC complex.

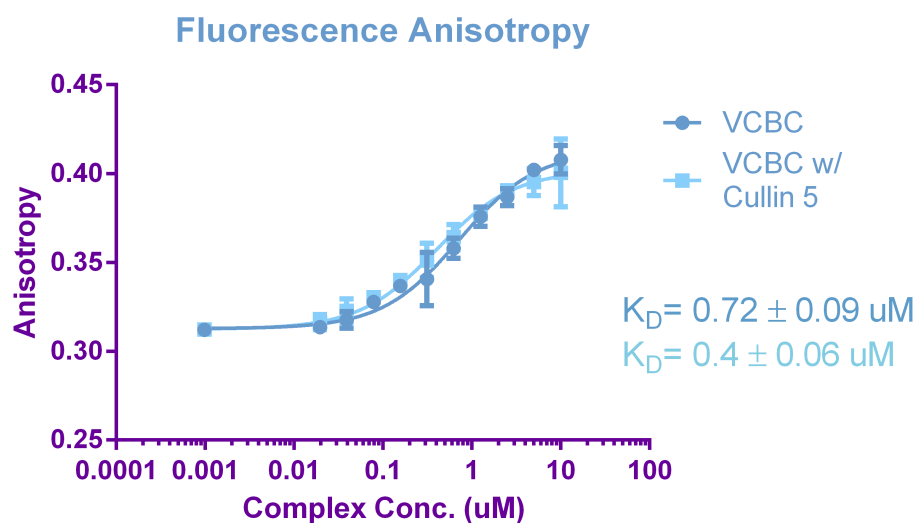


Figure 1.3| Fluorescence Anisotropy of VCBC and Cul5 with fluorescein tagged A3F.

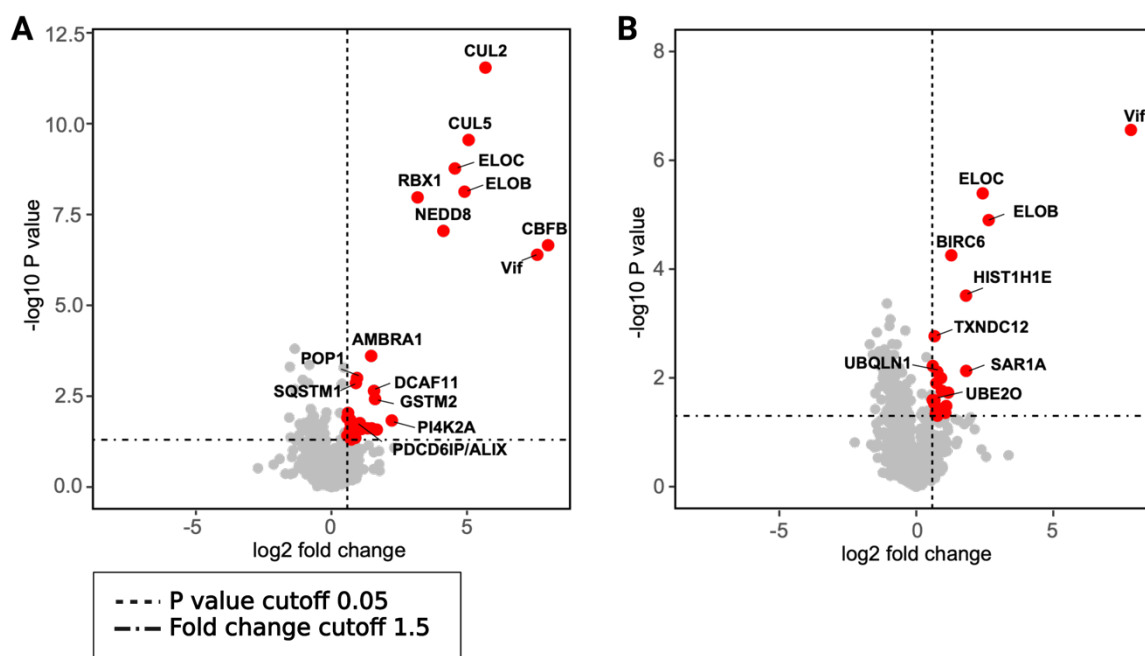


Figure 1.4| AP-MS of scFvs in HEK293Ts with Vif.

The 3C9 scFv pulls down the entire VCBC complex and E3 ubiquitination complex Cul5, RBX1, and NEDD8. B) The 1D1 scFv pulls down ELOC and ELOB. It also interacts with E2/E3 ubiquitin ligases BIRC6 and UBE20.

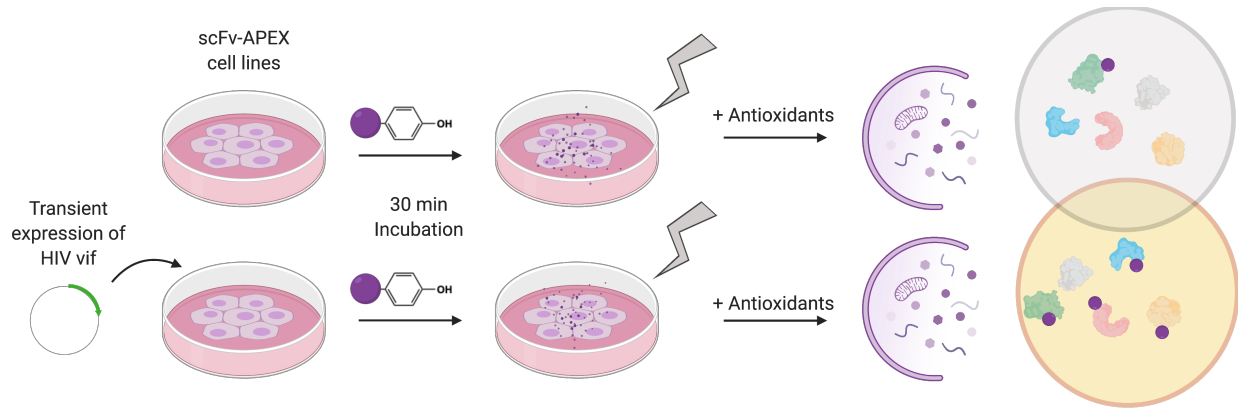


Figure 1.5| APEX Biotinylation Protocol.

(A) Workflow to biotinylated proteins. (B) Western blot analysis of cell lysate to assess functionality of the procedure. (C) Mass spectrometry workflow.

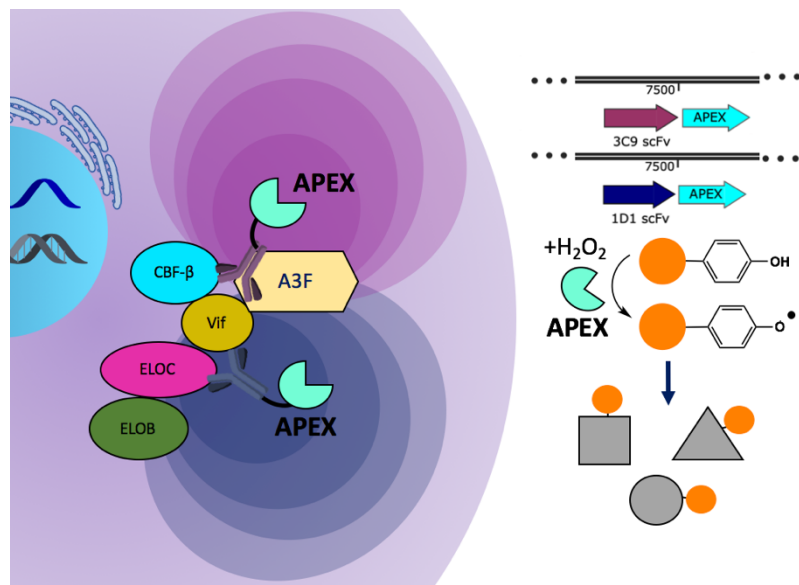


Figure 1.6| Biotinylation contour map of the cytoplasm.

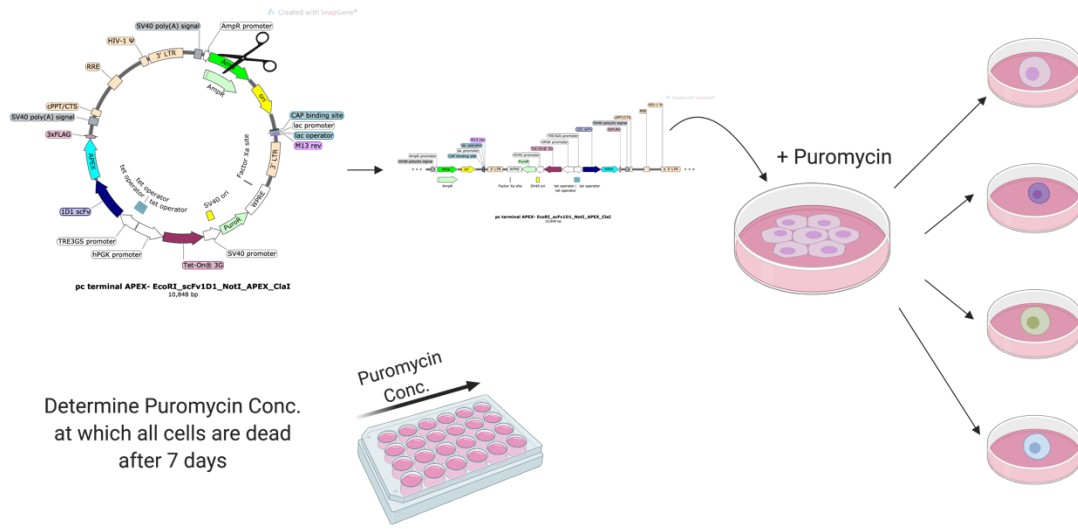


Figure 1.7| Generation of stable HEK293T scFv cell lines.

Table 1.1 | AP-MS pulldown with vif and 3C9 scFv in HEK293Ts.

Protein	Gene	Label	log2FC	pvalue
Q13951	CBFB	3C9-vif_3C9	7.99	2.2E-07
vifprotein	Vif	3C9-vif_3C9	7.59	4.1E-07
Q13617	CUL2	3C9-vif_3C9	5.68	2.9E-12
Q93034	CUL5	3C9-vif_3C9	5.06	2.8E-10
Q15370	TCEB2	3C9-vif_3C9	4.91	7.4E-09
Q15369	TCEB1	3C9-vif_3C9	4.55	1.7E-09
Q15843	NEDD8	3C9-vif_3C9	4.13	9.0E-08
P62877	RBX1	3C9-vif_3C9	3.18	1.1E-08
Q9BTU6	PI4K2A	3C9-vif_3C9	2.23	1.5E-02
O43847	NRD1	3C9-vif_3C9	1.67	2.6E-02
P28161	GSTM2	3C9-vif_3C9	1.61	3.8E-03
Q8TEB1	DCAF11	3C9-vif_3C9	1.57	2.3E-03
O60832	DKC1	3C9-vif_3C9	1.48	2.4E-02
Q9C0C7	AMBRA1	3C9-vif_3C9	1.47	2.5E-04
Q8WUM4	PDCD6IP	3C9-vif_3C9	1.33	2.4E-02
Q8N5W9	FAM101B	3C9-vif_3C9	1.11	2.5E-02
Q8IY67	RAVER1	3C9-vif_3C9	1.05	1.7E-02
Q99575	POP1	3C9-vif_3C9	0.94	1.0E-03
Q13501	SQSTM1	3C9-vif_3C9	0.90	1.4E-03
A6NNT2	C16orf96	3C9-vif_3C9	0.88	4.4E-02
P78318	IGBP1	3C9-vif_3C9	0.86	3.1E-02
Q9BPZ2	SPIN2B	3C9-vif_3C9	0.82	4.3E-02
Q96CU9	FOXRED1	3C9-vif_3C9	0.73	5.0E-02
P04792	HSPB1	3C9-vif_3C9	0.71	1.8E-02
Q9BUJ2	HNRNPUL1	3C9-vif_3C9	0.69	1.4E-02
P20700	LMNB1	3C9-vif_3C9	0.68	2.7E-02
Q9Y2Q9	MRPS28	3C9-vif_3C9	0.61	9.1E-03
P52597	HNRNPF	3C9-vif_3C9	0.59	1.2E-02
Q99615	DNAJC7	3C9-vif_3C9	0.59	3.9E-02

Table 1.2 | AP-MS pulldown with vif and 1D1 scFv in HEK293Ts.

Protein	Gene	Label	log2FC	pvalue
vifprotein	Vif	1D1-vif_1D1	7.84	2.8E-07
Q15370	TCEB2	1D1-vif_1D1	2.64	1.2E-05
Q15369	TCEB1	1D1-vif_1D1	2.43	4.0E-06
Q9NR31	SAR1A	1D1-vif_1D1	1.82	7.3E-03
P10412	HIST1H1E	1D1-vif_1D1	1.82	3.1E-04
Q9NR09	BIRC6	1D1-vif_1D1	1.28	5.6E-05
Q86SZ2	TRAPPC6B	1D1-vif_1D1	1.16	1.8E-02
Q13442	PDAP1	1D1-vif_1D1	1.09	3.3E-02
Q96TC7	RMDN3	1D1-vif_1D1	1.06	4.4E-02
P16403	HIST1H1C	1D1-vif_1D1	0.93	1.7E-02
P53004	BLVRA	1D1-vif_1D1	0.90	1.0E-02
Q9NR33	POLE4	1D1-vif_1D1	0.88	3.7E-02
Q9P2P1	NYNRIN	1D1-vif_1D1	0.77	5.0E-02
Q9UMX0	UBQLN1	1D1-vif_1D1	0.77	7.7E-03
A6NDG6	PGP	1D1-vif_1D1	0.73	1.2E-02
Q6PJT7	ZC3H14	1D1-vif_1D1	0.72	4.0E-02
O00139	KIF2A	1D1-vif_1D1	0.71	4.7E-02
O95881	TXNDC12	1D1-vif_1D1	0.67	1.7E-03
P39023	RPL3	1D1-vif_1D1	0.67	2.6E-02
Q8TD07	RAET1E	1D1-vif_1D1	0.65	2.9E-02
P55769	NHP2L1	1D1-vif_1D1	0.60	6.1E-03
Q9C0C9	UBE2O	1D1-vif_1D1	0.60	2.5E-02

1.6 References

1. Harris, R. S. & Liddament, M. T. Retroviral restriction by APOBEC proteins. *Nat. Rev. Immunol.* **4**, 868–877 (2004).
2. Duggal, N. K. & Emerman, M. Evolutionary conflicts between viruses and restriction factors shape immunity. *Nat. Rev. Immunol.* **12**, 687–695 (2012).
3. Luo, Y. *et al.* HIV–host interactome revealed directly from infected cells. *Nature Microbiology* **1**, 16068 (2016).
4. Chougui, G. & Margottin-Goguet, F. HUSH, a Link Between Intrinsic Immunity and HIV Latency. *Front. Microbiol.* **10**, 224 (2019).
5. Harris, R. S. *et al.* DNA deamination mediates innate immunity to retroviral infection. *Cell* **113**, 803–809 (2003).
6. Hultquist, J. F. *et al.* Human and rhesus APOBEC3D, APOBEC3F, APOBEC3G, and APOBEC3H demonstrate a conserved capacity to restrict Vif-deficient HIV-1. *J. Virol.* **85**, 11220–11234 (2011).
7. Refsland, E. W. *et al.* Quantitative profiling of the full APOBEC3 mRNA repertoire in lymphocytes and tissues: implications for HIV-1 restriction. *Nucleic Acids Res.* **38**, 4274–4284 (2010).
8. Jager, S. *et al.* Vif hijacks CBF- β to degrade APOBEC3G and promote HIV-1 infection. *Nature* **481**, 371–375 (2012).
9. Compton, A. A. & Emerman, M. Convergence and Divergence in the Evolution of the APOBEC3G-Vif Interaction Reveal Ancient Origins of Simian Immunodeficiency Viruses. *PLoS Pathog.* **9**, e1003135 (2013).

10. Sheehy, A. M., Gaddis, N. C., Choi, J. D. & Malim, M. H. Isolation of a human gene that inhibits HIV-1 infection and is suppressed by the viral Vif protein. *Nature* **418**, 646–650 (2002).
11. Salter, J. D., Morales, G. A. & Smith, H. C. Structural insights for HIV-1 therapeutic strategies targeting Vif. *Trends Biochem. Sci.* **39**, 373–380 (2014).
12. Jäger, S. *et al.* Global landscape of HIV–human protein complexes. *Nature* **481**, 365–370 (2012).
13. Zhang, W., Du, J., Evans, S. L., Yu, Y. & Yu, X.-F. T-cell differentiation factor CBF- β regulates HIV-1 Vif-mediated evasion of host restriction. *Nature* **481**, 376–379 (2012).
14. Matsui, Y. *et al.* Defining HIV-1 Vif residues that interact with CBF β by site-directed mutagenesis. *Virology* **449**, 82–87 (2014).
15. Salter, J. D., Lippa, G. M., Belashov, I. A. & Wedekind, J. E. Core-Binding Factor β Increases the Affinity between Human Cullin 5 and HIV-1 Vif within an E3 Ligase Complex. *Biochemistry* **51**, 8702–8704 (2012).
16. Guo, Y. *et al.* Structural basis for hijacking CBF- β and CUL5 E3 ligase complex by HIV-1 Vif. *Nature* **505**, 229–233 (2014).
17. Binning, J. M. *et al.* Fab-based inhibitors reveal ubiquitin independent functions for HIV Vif neutralization of APOBEC3 restriction factors. *PLoS Pathog.* **14**, e1006830 (2018).
18. Fraser, C. *et al.* Virulence and pathogenesis of HIV-1 infection: an evolutionary perspective. *Science* **343**, 1243727 (2014).
19. Harris, R. S. & Anderson, B. D. Evolutionary Paradigms from Ancient and Ongoing Conflicts between the Lentiviral Vif Protein and Mammalian APOBEC3 Enzymes. *PLoS Pathog.* **12**, e1005958 (2016).

20. Richards, C. M. *et al.* Reassessing APOBEC3G Inhibition by HIV-1 Vif-Derived Peptides. *J. Mol. Biol.* **429**, 88–96 (2017).
21. Faust, T. B., Binning, J. M., Gross, J. D. & Frankel, A. D. Making Sense of Multifunctional Proteins: Human Immunodeficiency Virus Type 1 Accessory and Regulatory Proteins and Connections to Transcription. *Annual review of virology* **4**, 241–260 (2017).
22. Cuevas, J. M., Geller, R., Garijo, R., López-Aldeguer, J. & Sanjuán, R. Extremely High Mutation Rate of HIV-1 In Vivo. *PLoS Biol.* **13**, e1002251 (2015).
23. Russell, R. A., Smith, J., Barr, R., Bhattacharyya, D. & Pathak, V. K. Distinct domains within APOBEC3G and APOBEC3F interact with separate regions of human immunodeficiency virus type 1 Vif. *J. Virol.* **83**, 1992–2003 (2009).
24. Binka, M., Ooms, M., Steward, M. & Simon, V. The activity spectrum of Vif from multiple HIV-1 subtypes against APOBEC3G, APOBEC3F, and APOBEC3H. *J. Virol.* **86**, 49–59 (2012).
25. Mehle, A., Thomas, E. R., Rajendran, K. S. & Gabuzda, D. A zinc-binding region in Vif binds Cul5 and determines cullin selection. *J. Biol. Chem.* **281**, 17259–17265 (2006).
26. Mahon, C., Krogan, N., Craik, C. & Pick, E. Cullin E3 Ligases and Their Rewiring by Viral Factors. *Biomolecules* **4**, 897–930 (2014).
27. Jean Beltran, P. M., Federspiel, J. D., Sheng, X. & Cristea, I. M. Proteomics and integrative omic approaches for understanding host-pathogen interactions and infectious diseases. *Mol. Syst. Biol.* **13**, 922 (2017).
28. Park, R. J. *et al.* A genome-wide CRISPR screen identifies a restricted set of HIV host dependency factors. *Nat. Genet.* **49**, 193–203 (2017).

29. Steen, H. & Mann, M. The abc's (and xyz's) of peptide sequencing. *Nat. Rev. Mol. Cell Biol.* **5**, 699–711 (2004).
30. Lam, S. S. *et al.* Directed evolution of APEX2 for electron microscopy and proximity labeling. *Nat. Methods* **12**, 51–54 (2015).
31. Lobingier, B. T. *et al.* An Approach to Spatiotemporally Resolve Protein Interaction Networks in Living Cells Resource An Approach to Spatiotemporally Resolve Protein Interaction Networks in Living Cells. *Cell* **169**, 350–360 (2017).
32. Hung, V. *et al.* Proteomic Mapping of the Human Mitochondrial Intermembrane Space in Live Cells via Ratiometric APEX Tagging. *Mol. Cell* **55**, 332–341 (2014).
33. Miller, J. H., Presnyak, V. & Smith, H. C. The dimerization domain of HIV-1 viral infectivity factor Vif is required to block virion incorporation of APOBEC3G. *Retrovirology* **4**, 81 (2007).
34. Hung, V. *et al.* Spatially resolved proteomic mapping in living cells with the engineered peroxidase APEX2. *Nat. Protoc.* **11**, 456–475 (2016).
35. Branon, T. C. *et al.* Directed evolution of TurboID for efficient proximity labeling in living cells and organisms. *bioRxiv* 196980 (2017).
36. Kaewsapsak, P., Shechner, D. M., Mallard, W., Rinn, J. L. & Ting, A. Y. Live-cell mapping of organelle-associated RNAs via proximity biotinylation combined with protein-RNA crosslinking. *Elife* **6**, e29224 (2017).
37. Vaughan, T. J., Osbourn, J. K. & Tempest, P. R. Human antibodies by design. *Nat. Biotechnol.* **16**, 535–539 (1998).
38. Morris, J. H. *et al.* Affinity purification-mass spectrometry and network analysis to understand protein-protein interactions. *Nat. Protoc.* **9**, 2539–2554 (2014).

39. Mellacheruvu, D. *et al.* The CRAPome: a contaminant repository for affinity purification-mass spectrometry data. *Nat. Methods* **10**, 730–736 (2013).
40. Li, Y. Commonly used tag combinations for tandem affinity purification. *Biotechnol. Appl. Biochem.* **55**, 73–83 (2010).
41. Metzger, M. B., Pruneda, J. N., Klevit, R. E. & Weissman, A. M. RING-type E3 ligases: master manipulators of E2 ubiquitin-conjugating enzymes and ubiquitination. *Biochim. Biophys. Acta* **1843**, 47–60 (2014).
42. Hüttenhain, R. *et al.* ARIH2 Is a Vif-Dependent Regulator of CUL5-Mediated APOBEC3G Degradation in HIV Infection. *Cell Host Microbe* **26**, 86-99.e7 (2019).
43. Goila-Gaur, R. & Strebel, K. HIV-1 Vif, APOBEC, and Intrinsic Immunity. *Retrovirology* **5**, 51 (2008).
44. GeneCards Human Gene Database. [No title]. <https://www.genecards.org/cgi-bin/carddisp.pl?gene=SQSTM1>.
45. Liu, X. *et al.* UBE2O promotes the proliferation, EMT and stemness properties of breast cancer cells through the UBE2O/AMPK α 2/mTORC1-MYC positive feedback loop. *Cell Death Dis.* **11**, 10 (2020).
46. transfection-optimization-protocol-dna (1).pdf.
47. Cells, \square . Cultured Hek. Materials required, but not supplied.
48. Apolonia, L. *et al.* Promiscuous RNA Binding Ensures Effective Encapsidation of APOBEC3 Proteins by HIV-1. *PLoS Pathog.* **11**, e1004609 (2015).
49. York, A., Kutluay, S. B., Errando, M. & Bieniasz, P. D. The RNA Binding Specificity of Human APOBEC3 Proteins Resembles That of HIV-1 Nucleocapsid. *PLoS Pathog.* **12**, e1005833 (2016).

50. Khan, M. A. *et al.* Human immunodeficiency virus type 1 Vif protein is packaged into the nucleoprotein complex through an interaction with viral genomic RNA. *J. Virol.* **75**, 7252–7265 (2001).
51. Hultquist, J. F. *et al.* A Cas9 Ribonucleoprotein Platform for Functional Genetic Studies of HIV-Host Interactions in Primary Human T Cells. *Cell Rep.* **17**, 1438–1452 (2016).

Chapter 2

Determining the effects of HIV Protease Cleavage of Host Proteins

2.1 Abstract

HIV-1 protease (HIV PR) plays an important role in virus maturation, but it can also cleave important host proteins during infection. Comparing the interactome of HIV PR with an N-terminal degradomics screen to assay activity in cells several host substrates were identified. HIV PR cleaves EIF3D, KAP1, and PTBP1 in HEK293Ts. Cleavage of KAP1 and PTBP1 was confirmed in infected primary CD4⁺ T cells. KAP1 is known to regulate endogenous retroviral elements, integration of retroviruses, and suppression of retroviral transcription in latently infected T cells.¹ Cleavage of KAP1 by HIV PR could aid integration of HIV and increase the frequency of the lytic phase.

2.2 Introduction

Viral Proteases are essential to viral infection. The essentiality of viral proteases has been exploited to combat viral infections by designing viral protease inhibitors as a first line of defense.² Viral protease inhibitors suffer from significant off target toxicity and resistance mutations.³ Viral protease inhibitors have a crucial efficacy window. Most viruses encode their own viral protease(s) and tightly regulate protease activity to function at specific times in the viral life cycle. Dysregulation of HIV PR activity has detrimental effects on viral proliferation. HIV PR activity in the cytoplasm can initiate a caspase cascade by cleaving a caspase recruitment domain 8 (CARD-8) and inducing pyroptosis.⁴ Viral proteases of other viruses like Dengue and SARS-CoV-2 have been shown to cleave host proteins which benefit viral immune evasions and proliferation.^{2,5} The extent to which viral proteases interact with the host is barely surveyed in a few highly studied viruses like HIV, Dengue, and SARS-CoV-2, there are likely many examples of viral proteases being utilized by a virus to disrupt cell function.

In an effort to understand the global landscape of HIV PR interactions in a human cell an AP-MS screen with a catalytically inactive HIV PR identified 53 proteins with the potential to be cleaved by HIV PR.⁶ These host proteins largely fall into the category of transcriptional and translational regulators. A novel screen of host proteins cleaved by active HIV PR has added excitement to the coalescing factors identified by Jager et al.⁶ However, the convergence between AP-MS and N-terminal degradomics screens with the dox-inducible HIV PR Jurkat cells is minimal.⁷ The validation of potential HIV PR interactions with host proteins is essential to gain a bigger picture of HIV-1 function. The evaluation of the protease host interactions *in vitro* demonstrate that HIV PR has the capability to cleave host proteins in addition to HIV Gag and Gag-Pol. *In vivo* experiments in CD4⁺ T cells showed that HIV PR could and does cleave these proteins during an infection although it is subject to donor variability. The verification of PTBP1 and KAP1 as host substrates of HIV PR *in vivo* requires the investigation of potential effects on the host.

PTBP1 has four RNA binding domains and recognizes the hexanucleotide sequence CUCUCU in mRNA.⁸ PTBP1 binding to mRNA represses the splicing of exons by binding adjacent introns.⁹ PTPB1 increases the stability of CD154 mRNA (or CD40L) in CD4⁺ T cells.^{10,11} CD154 expression regulates immunomodulatory pathways including expression of TNF- α , IL-2 and IL-10.⁸⁻¹³ PTBP1 regulates mRNA splicing and stability in many cell types and its degradation could result in a number of phenotypes it is unclear whether it plays a major role in HIV-1 infection. A study of proteolytic activity in SARS-CoV-2 infection⁵ found that PTBP1 cleavage by SARS-CoV-2 3Clpro caused mislocalization of PTBP1 to the cytoplasm. This cleavage of PTBP1 may aid SARS-CoV-2 by reducing the impact PTBP1 has on viral

transcription.¹⁴ Further study of HIV PR effect on PTBP1 localization could show a similarity because of a similar proximity in cleavage sites.

The degradation of KAP1 by HIV PR has two potential very important outcomes on infection. Foremost KAP1 binds acetylated HIV-1 integrase (IN) during initial infection and deacetylates thereby deactivating IN.¹⁵ KAP1 recruits Histone deacetylase 1 (HDAC1) to deacetylate IN.¹⁵ The activity of KAP1 reduces integration events by 60%¹⁵ and thus reduces the establishment of latently infected T cells. The expression of KAP1 not only reduces integration in T cells but is thought to be another factor that limits HIV infection in myeloid lineages.^{16,17} KAP1 likely works in concert with other host viral transcriptional repressors like the Human silencing hub (HUSH) complex.^{18,19}

Secondly, KAP1 acts as a transcriptional repressor in latently infected CD4⁺ T cells. apolipoprotein B mRNA editing enzyme A (APOBEC3A, A3A) recruits KAP1 to the 5' LTR of integrated HIV-1 and this leads to the recruitment of the NuRD/SETDB1 complex to deposit silencing H3K9 trimethyl marks.²⁰ Knockout of KAP1 or A3A increase the amount of both spontaneous and stimulated reactivation in both a latently infected Jurkat cell line J-Lat10.6 and primary CD4⁺ T cell latency models.²⁰ Degradation of these important host factors likely would have negative effects on the host's innate immune response. The potential cumulative effect of degradation of these host factors could explain some of the trends seen from long term treatment with protease inhibitors in infected patients.

It is now understood that the viral envelope fuses with the cell membrane and the viral capsid is transported into the cytoplasm and is transported through the nuclear envelope.²¹⁻²⁴ The capsid acts as a shield to host degradation of viral RNA and proteins.²² The capsid has structural pores that enable the transport of nucleotides into the capsid for reverse transcription of HIV

RNA to DNA within the capsid.²⁵ Following reverse transcription and entry into the nucleus the viral capsid degrades near a preferred site of integration.²² This protects both viral RNA and proteins, viral proteins contained within the capsid like HIV PR are then deposited into the nucleus. HIV PR has access to nuclear proteins and important transcription factors like KAP1 and PTBP1 that may affect viral fitness. Active dimerized HIV PR is delivered to the site of integration almost like a bodyguard to HIV IN. The potential for active HIV PR in resting CD4⁺ T cells is less clear. While the expression of integrated HIV provirus is under a positive feedback loop, low expression of viral RNA can persist.²⁶ Low expression of HIV PR during latency could enhance a reactivation event. This has previously been attributed to off target effects of HIV PR inhibitors in the Akt pathways.³ However, we have shown in J-Lat10.6 cells that stimulation and subsequent treatment with HIV PR inhibitors reduces the degradation of the C-terminus of KAP1. The C-terminal PHD and Bromo domains of KAP1 are required for recruiting HP1 and other host machinery to the HIV 5'LTR and suppressing reactivation.²⁷⁻²⁹

2.3 Results

2.3.1 Identifying possible interactions between host proteins and HIV PR

AP-MS experiments performed by the Krogan lab showed that pulldown experiments with viral protein and cell lines were not consistent. There is modest overlap between affinity purification pulldown with C-terminally Streptavidin tagged HIV PR in HEK293Ts and Jurkat E6.1 cell line (**Figure 2.2**). There was little to no overlap between the interactome identified by AP-MS and N-terminal degradomics, only 3 substrates were identified in all 3 experiments. These substrates included KAP1, EIF3B, PCBP2, and PYC. Several candidates from all three

experiments were then tested in HEK293Ts. These substrates were chosen based on their relevance to mammalian transcription and translation.

In collaboration with Cathal Mahon (Craik lab, UCSF), we seek to identify human substrates of the HIV PR (host - viral protein interactions). The Gevaert lab has attempted such studies in the past using COFRADIC and adding exogenous HIV PR into cell lysate,³⁰ but the data is not as robust as one could hope for, making target validation difficult. To better determine HIV PR substrates a doxycycline inducible Jurkat cell line was used to express the HIV PR. Utilizing a technique from the Wells lab employing SILAC (light/heavy) and subtiligase positive N-termini enrichment in order to quantify cleavage products over background. We grew 4L of Jurkat cells, 2x1L light and 2x1L heavy. Doxycycline (DOX) was added for 16h in one light (L+) and one heavy flask (H+), while Saquinavir (SQV) was added into the other light (L-) and the other heavy (H-) flasks. Saquinavir was added in the control samples to inhibit any background expression of HIV PR. Samples were combined for subtiligase labeling (**Figure 2.4, Figure 2.5**).

In total, we identified 260 and 245 N-terminal protein fragments in the DOX and SQV treated samples, respectively. By removing native protein N-termini and methionine removal, we identified 190 (DOX) and 178 (SQV) cleavage sites. We hypothesized that the HIV PR would generate new cleavage sites in human cells never seen in previously experiments. We compared our 190 cleavage sites observed in DOX-induced HIV PR samples to previously identified N-termini in human experiments³¹ and found that 35 sites were never observed before. We cherry picked KAP1 and PTBP1 for further investigation.

2.3.2 Evaluation of HIV PR Substrates in HEK293Ts

Host protein targets that were selected from HIV PR interaction screens and datasets were tagged C-terminally with a 3XFLAG tag. Cleavage of the FLAG tagged targets were assessed in cells by co-transfecting HEK293Ts with FLAG tagged host protein and streptavidin tagged HIV PR. Most host substrates identified in AP-MS did not show cleavage in HEK293Ts. Three host proteins showed cleavage with increasing amounts of HIV PR DNA transfected. EIF3D which was identified by AP-MS showed substantial cleavage after 48 hours. Similarly, host substrates PTBP1 and KAP1 showed increased cleavage proportional to the amount of HIV PR DNA transfected. FLAG AP-MS of tagged host protein was used to isolate EIF3D, PTBP1, and KAP1 from lysate. The cleavage site of KAP1 and PTBP1 were reconstructed from FLAG tagged fragments from cleavage gels for identification with mass spectroscopy. Flag tagged KAP1 appeared to undergo two proteolysis events creating fragments ~50 kDa and ~45 kDa in size. Cleavage sites were then pinpointed by using approximate molecular weight, predicted HIV proteolytic sites, and mutation of predicted P1 sites. Mutations were made in the predicted site of cleavage of each host protein. Mutated host proteins with a FLAG tag were then co-transfected with HIV PR and disruption of cleavage of FLAG tagged fragments were assessed by SDS page gel.

2.3.3 HIV proteolytic activity in CD4⁺ T cells

The validation of host substrates for HIV PR in HEK293Ts showed that only a few proteins identified by convergent mass spectroscopy screens were able to be cleaved in cells. The cleavage of the co-transfected host substrates proved that HIV PR would be able to cleave the host protein but not whether it had relevance during an infection. To discover the potential role

of non-canonical HIV Proteolytic activity during an infection CD4⁺ T cells were isolated from donor LRCS or purchased frozen. The CD4⁺ T cells were then stimulated with IL-2 and CD2/CD3/CD28 beads. The stimulation of these CD4⁺ T cells was confirmed by flow cytometry for CD4 and CD25 expression. Cells were then infected and substrates of interest were analyzed for cleavage by western blot (**Figure 2.6**). Infection with HIV-1 NL4-3 ΔNef GFP of three donor CD4⁺ T cells show between 4-20% infection following spinfection (**Figure 2.6**). Donor samples treated with HIV PI darunavir and saquinavir show modest reduction (1-2%) in GFP fluorescence. The cellular translation initiator EIF3D was not cleaved during viral infection. PTBP1 is degraded in CD4⁺ T cells infected with HIV-1 NL4-3 Dnef GFP compared to uninfected T cells. The treatment of HIV PI darunavir and saquinavir 24 hpi show a restoration of near cellular levels of PTBP1 (**Figure 2.7**). KAP1 shows no degradation when blotted for using an antibody specific for the N-terminus of KAP1 (amino acid residue 60-383). The C-terminus of KAP1 is cleaved when CD4⁺ T cells are infected. Treatment with Darunavir and Saquinavir modestly inhibits the degradation of the C-terminus of KAP1 in Donor B and C (**Figure 2.7**). Cleavage of the host substrates PTBP1 and KAP1 were not inhibited by the addition of protease inhibitors in Donor A.

2.3.4 HIV Proteolytic Activity During Latency in J-Lat10.6 cells

Confirmation of PTBP1 and KAP1 cleavage during HIV infection of CD4⁺ T cells prompts evaluation of downstream consequences of host factor cleavage. To evaluate the potential effect of KAP1 cleavage by HIV PR during latency J-Lat10.6 cells were stimulated with 100 nM phorbol 12-myristate 13-acetate (PMA) to reactivate integrated provirus. J-Lat10.6 cells were treated with HIV PR inhibitors 10 mM darunavir and 10 mM saquinavir in addition to

PMA (**Figure 2.8**). The C-terminus of KAP1 is partially degraded in J-Lat10.6 cells treated with 100 nM PMA compared with unstimulated J-Lat10.6 cells. J-Lat10.6 cells treated with protease inhibitors restore cellular levels of C-terminal KAP1 (**Figure 2.8**).

2.3.5 Reduced Co-localization of KAP1 with HP1 γ

KAP1 and HP1 γ colocalize in the nucleus during normal cell proliferation. KAP1 is predominantly localized in the nucleus and forms a soft halo around HP1 γ puncta. In J-Lat10.6 cells treated with 100 nM PMA activating the expression of viral proteins and GFP KAP1 forms the distinctive puncta in association with HP1 γ . Protease inhibitor treatment in conjunction with PMA reactivation reduce the amount of puncta colocalized with HP1 γ (**Figure 2.9**).

2.4 Discussion

Any viral infection is likely to alter the translational landscape of the host cell infected. Many of the mechanisms of how HIV elicits these changes are not perfectly understood. The initial experiments performed by the Krogan Lab showed 53 potential substrates of HIV PR.⁶ N-terminomics with an HIV PR Jurkat cell line picked up a different set of host cleavages. These experiments showcase the importance of experimental design to understand interactions between virus and host. Jager et al 2012, utilized transfection of viral proteins into the cytoplasm of HEK293T cells and Jurkat cell lines. Recent studies show that the viral capsid of HIV maintains integrity up until the point of integration. Jacques et al 2016, showed that the pore of the capsid regulates entry of nucleotides into the viral capsid so viral reverse transcription physically occurs in the capsid. The model of EIF3D interaction with viral RNA proposed would not be possible based on cellular and viral localization. Upon completion of reverse transcription and appropriate

localization of the capsid in the nucleus the capsid degrades (~10-15 hpi). Similarly, the HIV PR interactions with cytoplasmic proteins while not impossible is less possible. While HIV PR likely cleaves several host proteins non-specifically we have shown that it can and does cleave KAP1 during infection. The cleavage of KAP1 by HIV PR has the potential to abrogate the innate antiviral effects of KAP1 and increase integration into the host genome.

Potential effects of disrupted KAP1 function have been identified in a cohort of HIV infected patients. Patients were treated with either an Antiretroviral therapy (ART) cocktail that included a HIV PR inhibitor or only contained 2 non-nucleoside reverse transcriptase inhibitors (NNRTIs).³² Resting CD4⁺ T cells were isolated from HIV infected patients and assayed for the amount of viral RNA present in the supernatant and the amount of HIV DNA integrated into the patient's genomes. Patients on an ART cocktail that included a PI had significantly reduced HIV transcription and significantly fewer integrated proviruses in their CD4⁺ T cell DNA.³² This study focused on the effect of PIs in latency and coupled with the effects of KAP1 on reducing reactivation during latency²⁰ give credibility to the possibility that HIV PR inhibitors are reducing the degradation of KAP1 during early infection and latency to reduce integration and reduce reactivation. While long term treatment with HIV PIs has high morbidity, these results could present a window of opportunity in treating newly infected patients to reduce the amount of integration and decrease the pool of latently infected T cells. Patient RNAseq data has also identified KAP1 mRNA levels as a predictor of patient disease progression. KAP1 expression in different PBMCs is variable and KAP1 expression in T cells is low compared to dendritic cells. Infection of dendritic cells is unusual in part to the levels of KAP1. It is interesting that although the cleavage of KAP1 is confirmed to be in the HP1 binding site, the localization of HP1g is largely unaffected in J-Lat10.6 cells.

Future studies to assess the effect of PI treatment on integration and viral production during infection would be of interest. This data suggests that HIV PR cleavage of KAP1 in this context could reduce the amount of integration in infected cells. Thereby reducing the pool of latently infected T cells in patients. A much larger clinical study would need to be done to evaluate this effect to inform patient treatment. It is also likely that the adjustment of treatment for patients who are not diagnosed soon after exposure would only modestly benefit from PI treatment. However, as the field of HIV shifts to controlling viral replication and reducing the number of new infections consideration of reducing latency is worthwhile.

2.5 Materials and Methods

Reagents, Plasmids, and Cell lines.

PMA (phorbol 12-myristate 13-acetate) was purchased from Sigma-Aldrich. Dynabeads Protein G, Dynabeads and Human T-Activator CD3/CD28 (CD3/28-Dynabeads) were purchased from Thermo Fisher Scientific. anti-KAP1 (ab22553), anti-H3K9 trimethylation (ab8898), and anti-HP1gamma (CS203221) antibodies were purchased from Millipore. Anti-GAPDH (GTX627408-01), HRP-conjugated anti-rabbit (7074), and HRP-conjugated anti-mouse (7076) antibodies were from Cell Signaling Technology. Hek293Ts and Jurkat E6-1 were purchased from the American Type Culture Collection (ATCC). Viral clones, anti-p24, darunavir, saquinavir and J-Lat10.6 cells were provided by the AIDS Research and Reference Reagent Program, Division of AIDS, NIAID, NIH. J-Lat10.6 KAP1 KO cells were generously provided by Akiko Iwasaki at Yale University, New Haven. Patient derived Primary CD4⁺ T cells were purchased from Stemcell technologies.

N-terminal labeling

The two replicate samples (L+,H- and H+L-) were lysed in 1% Triton, 100mM Bicine (pH 7.4) and the presence of protease inhibitors (5mM EDTA, 1mM AEBSF, 1mM PMSF, 4mM IAM, 10uM z-vad-fmk, 100uM E-64). We used 20 mM DTT to react with excess IAM before performing N-terminal labeling using 1 uM subtiligase and 1 mM biotin ester peptide (TEVEST4B) for 1 hour. Proteins were precipitated using acetonitrile, then denatured (8 M Gdn-HCl), diluted, and reduced (2 mM TECP), and thiols were alkylated (4 mM IAM), before ethanol precipitation. Biotinylated N-terminal protein fragments were then captured with NeutrAvidin agarose beads for 48 h. The beads were washed using 4 M Gdn-HCl, trypsinized, and released from the beads using TEV protease. The tryptic peptides fractionated into 11 fractions/sample, using high pH reverse phase C18 chromatography, and were then desalted with a C18 Ziptip (Millipore).

Mass Spectrometry

LC-MS/MS was performed on a QExactive Plus (Thermo Fisher Scientific) featuring a nanoflow HPLC (Dionex UltiMate 3000, Thermo Fisher Scientific) equipped with an analytical column (Acclaim Pep-Map RSLC, 75 μ m x 150 mm, Thermo Fisher Scientific). Peptides were eluted over a linear gradient from 2% to 30% acetonitrile in 0.1% formic acid. For data analysis, peptide sequences were assigned using ProteinProspector (v5.13.2) database search engine against the Swiss-Prot human protein database (2013.6.27). Search parameters included a precursor mass tolerance of 20 ppm, fragment ion mass tolerance of 6 ppm, up to three missed trypsin cleavages, constant carbamidomethylation of cysteine and N-terminal addition of aminobutyric acid (Abu), as well as variable oxidation of methionine. Heavy peptides were identified by using constant Lys and Arg (+8 and +10). The identified peptides were searched

against a random decoy protein database for evaluating the false positive rates (set to <1%). Raw data has been deposited in the MassIVE repository.

Cleavage of host factors in HEK293Ts

Mammalian cells were maintained in a humidified incubator at 37°C and 5% CO₂. 293T cells were obtained from the American Type Culture Collection and grown in DMEM (Hyclone, Gibco) supplemented with 10% Fetal Bovine Serum (Hyclone, Gibco). In brief, lysates from 1x10⁶ cells of Jurkat T cells expressing HIV PR (+/- 5uM Saquinavir) were separated by SDS PAGE and each lane was excised into 10 slices. Each slice was subjected to LC-MS/MS following in gel digestion with trypsin. To eliminate SILAC errors “flipped” experiments were carried out in both heavy and light media. Resulting peptides were analyzed using MaxQuant and statistically filtered to rank host proteins reduced in abundance in the absence of saquinavir and proteins that appeared in both expected and faster migrating gel slices. Western blotting was performed using mouse anti-Flag antibody (Sigma) at 1/10,000.

CD4⁺ T cell isolation

Trima Leukoreduction Chambers (LRCs) were purchased from Blood Centers of the Pacific. CD4⁺ T cells were isolated from LRCs using a Fabian CD4⁺ T cell kit and Fabian robot as previously described.³³ Purity of CD4⁺ T cells was assessed by staining with anti-CD4 APC and anti-CD25 antibodies on an Attune NxT Flow cytometer.

HIV NL4-3 virus production

HIV virus was produced by transfecting HEK293T cells with vector provided by the NIH AIDS reagents program. Low passage HEK293Ts were plates at 2.7e5 cells/mL in T250 flasks for transfection with PolyJet transfection reagent the next day. A ratio of 12 ug to 100 uL of pHIV NL4-3 DNA to Polyjet was used. Virus was harvested from the HEK293T supernatant 48 hours

post transfection and precipitated using a 50% PEG-6000 and 4M NaCl solution. Virus was allowed to precipitate at 4°C for 4 hours and then isolated by centrifugation before resuspension in RPMI-1640 and freezing for storage at -80°C.

Infection of Donor CD4⁺ T cells with HIV by centrifugation

Donor samples were purchased from Stanford blood bank. Fresh leukocyte reduction chambers were processed with CD4⁺ antibodies for the isolation of the CD4⁺ population using the Fabian kit as previously described. CD4⁺ T cells were also purchased frozen from stem cell technologies. Fresh or frozen CD4⁺ T cells were stimulated with CD2/CD3/CD28 tetramers and 80 IU/mL of IL-2 (Miltenyi). Cells were stimulated for 10 days prior to infection with HIV-1 NL4-3 GFPΔnef (ASI). Cells were infected with a multiplicity of infection of 1:25 by spininfection. CD4⁺ T cells were centrifuged with virus at 1,200 x g for 40 mins at 4°C. 24hr post infection cells were treated with DMSO, Saquinavir, or Darunavir and allowed to grow for an additional 24 hours. After 48 hours cells were sorted with a BD FACS Calibur on GFP fluorescence and viability (7-AAD stain). Infected cells and uninfected cells were prepared for sequencing by the addition of TRIzol before freezing at -80°C. Frozen aliquots of 50K cells were saved for western blot.

Western blot analysis

An aliquot of 50,000 cells were sorted during FACS and frozen at -80° C. CD4⁺ T cells were lysed in RIPA buffer supplemented with SDS and cOmplete, EDTA-free Protease Inhibitor Cocktail (ROCHE) on ice.

J-Lat10.6 cells ChIP

J-Lat10.6 cells were fixed for 6 mins with 1% formaldehyde according to the ChIP IT express protocol for suspension cells.³⁴ Fixed samples were sonicated with a fisher scientific model 705

sonic dismembrator for five and a half minutes with a 10 second on 10 second off pulse cycle. Sheared chromatin was incubated with 2 mg of KAP1 [201C] antibody and 5 mg H3K9me3 antibody overnight. ChIP was performed following ChIP-Enzymatic Express protocol.³⁵ DNA was cleaned up using NucleoSpinä gel and PCR cleanup columns for SDS samples.³⁶

Microscopy

J-Lat10.6 cells were treated as described in ChIP experiments and fixed for microscopy following Tsang et al. protocol for microscopy of suspension cells.³⁷ In brief cells were centrifuged and resuspended in PBS on Poly-L-lysine coated microscopy slides. Cells were allowed to adhere for 30 minutes at 25°C before fixing with 10% formalin in PBS (Sigma-Aldrich, St. Louis, MO, USA) for 10 minutes. Cells were washed with PBS and permeabilized with 0.5% Triton X-100 (Thermo Fisher, Waltham, MA, USA) for 10 minutes. Cells were washed again twice with PBS and blocked for 30 minutes with 1% BSA. 1° antibody was added 2µg/mL in 1% BSA and incubated overnight at 4°C. Cells were washed twice with PBS and then incubated for 1 hour at 25°C with 2° antibody. Cells were washed and incubated with DAPI for 10 minutes. Slides were mounted using Immogold antifade with DAPI. Microscopy was performed with the UCSF Nikon Imaging center on a Confocal Spinning Disk Microscope (Zeiss 510m; Zeiss, Oberkochen, Germany).

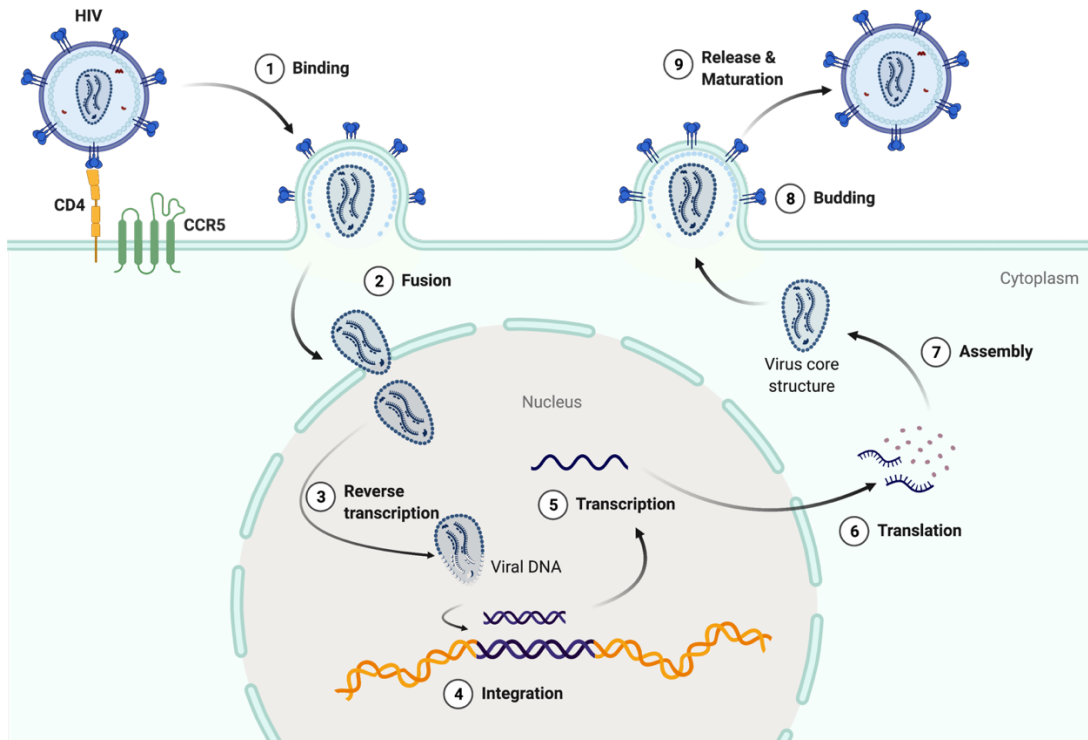


Figure 2.1 | The viral lifecycle of HIV-1.

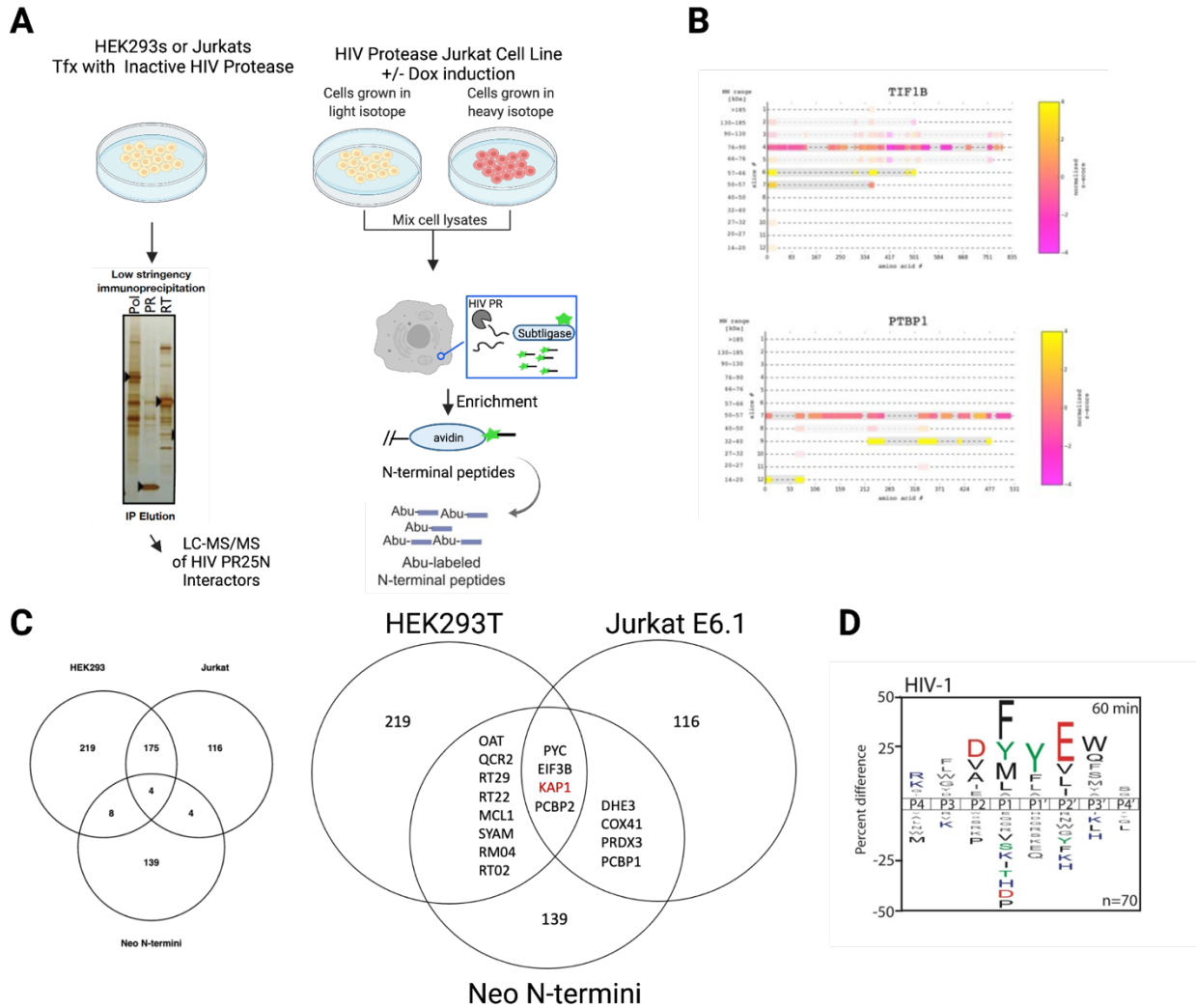


Figure 2.2 | Identification of HIV protease interactions with host proteins.

A) Experimental design of SILAC MS for AP-MS with catalytically inactive HIV PR and N-terminomics with subtiligase in HIV PR Jurkat cell line. B) Peptide coverage by IPMS, predicted sites. C) Convergence of AP-MS and N-terminomics data sets. D) HIV-1 Protease substrate specificity.

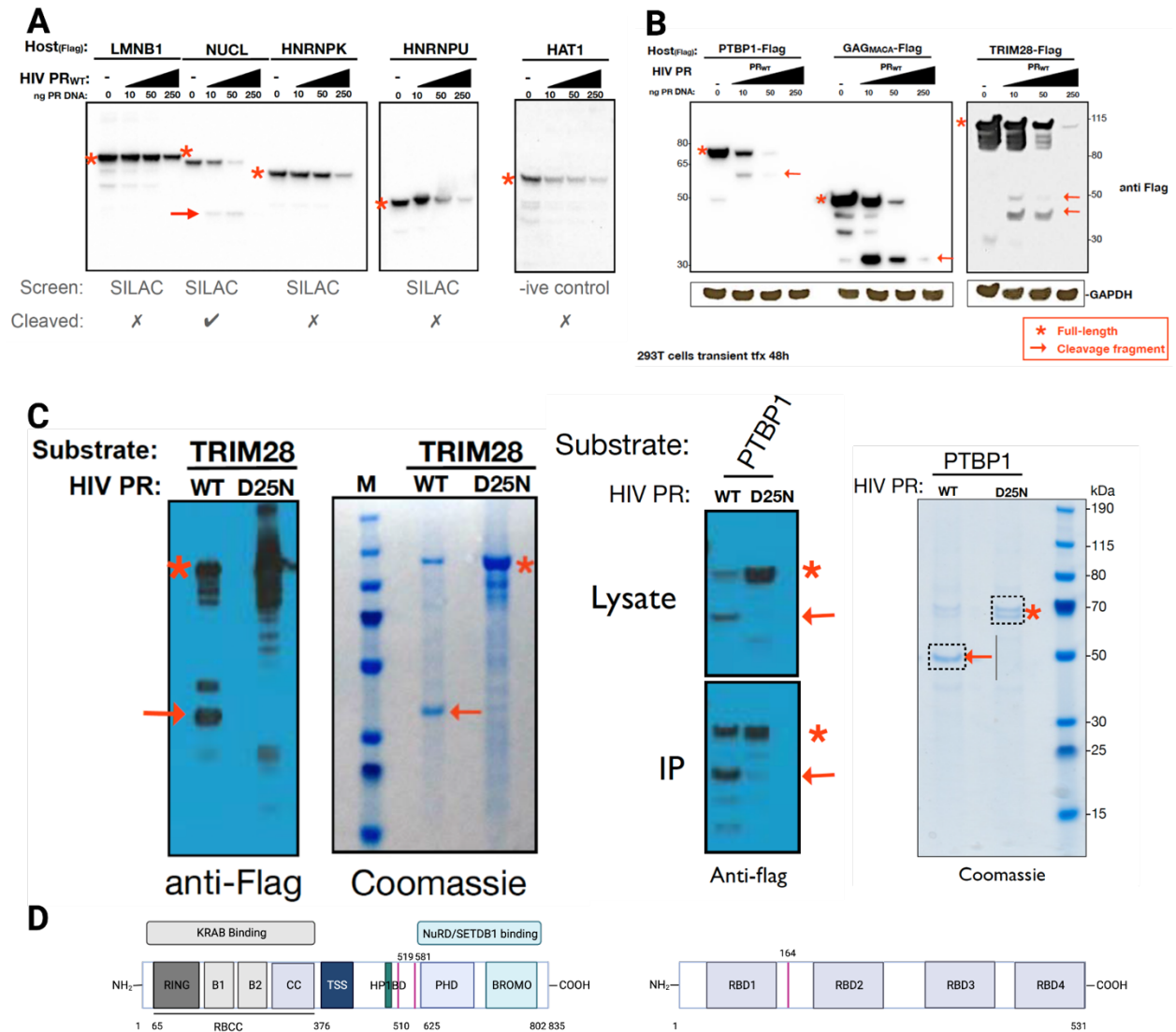


Figure 2.3 | Host substrate cleavage by HIV PR in HEK293Ts.

A) Substrates that were not cleaved in cells from Jager et al. B) Cleavage of PTBP1, KAP1 and EIF3d in cells C) Cleavage of KAP1 and PTBP1 with recombinant HIV PR D) Domain architecture and cleavage site of KAP1 and PTBP1.

Experimental setup

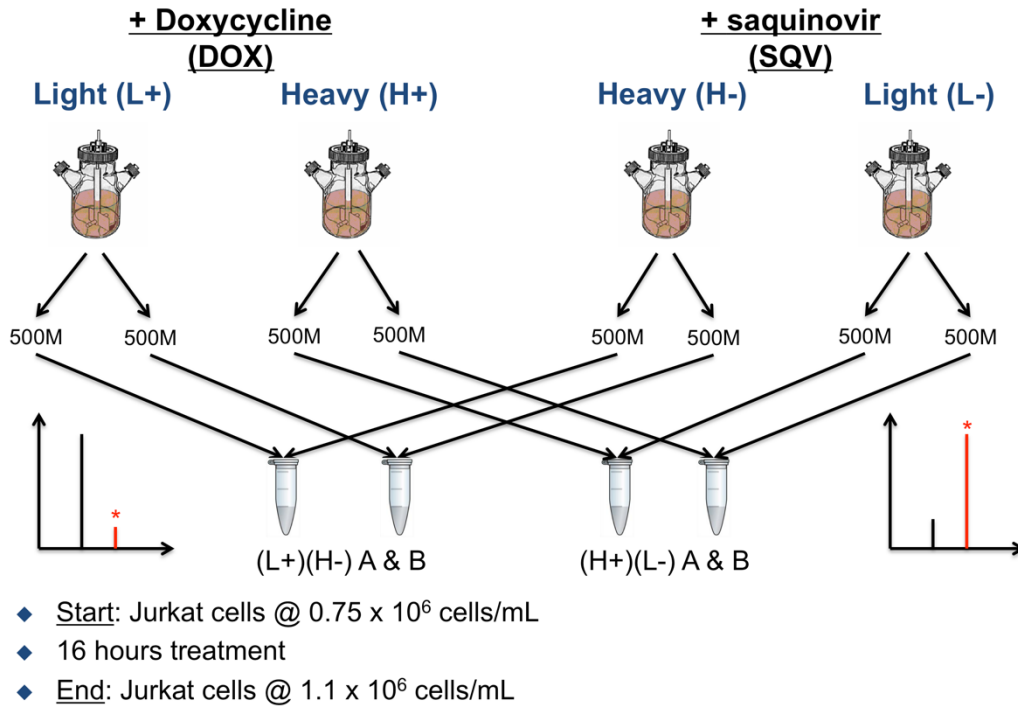


Figure 2.4 | Experimental setup for inducing HIV protease in Jurkat cells.

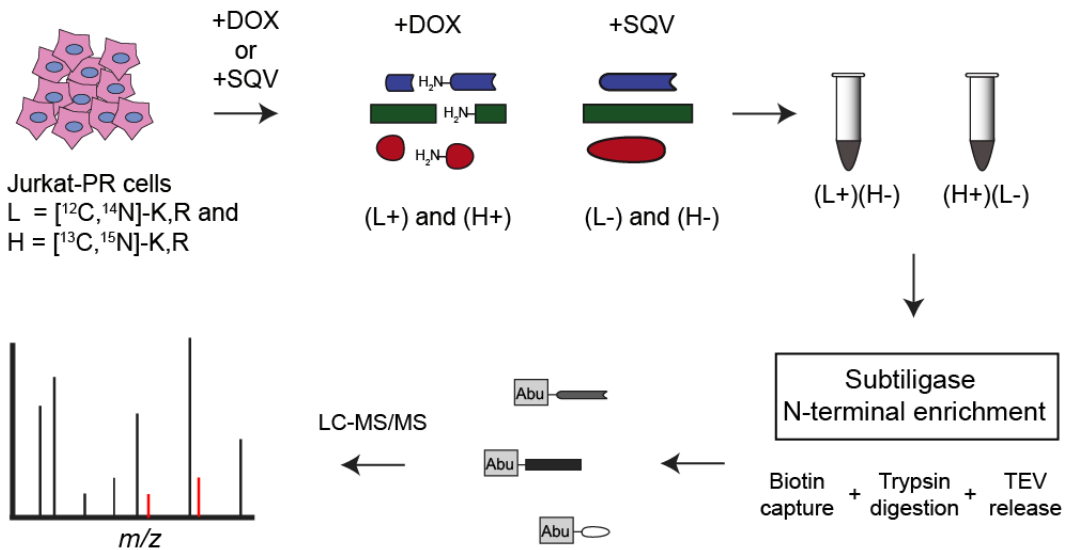


Figure 2.5 | Subtiligase N-terminomics of HIV protease substrates.

Jurkat cells were grown in both light and heavy media in replicates each. DOX was added in one light (L+) and one heavy (H+) cell lines. Saquinovir was added to the controls (L- and H-). DOX and SQV light and heavy samples were combined.

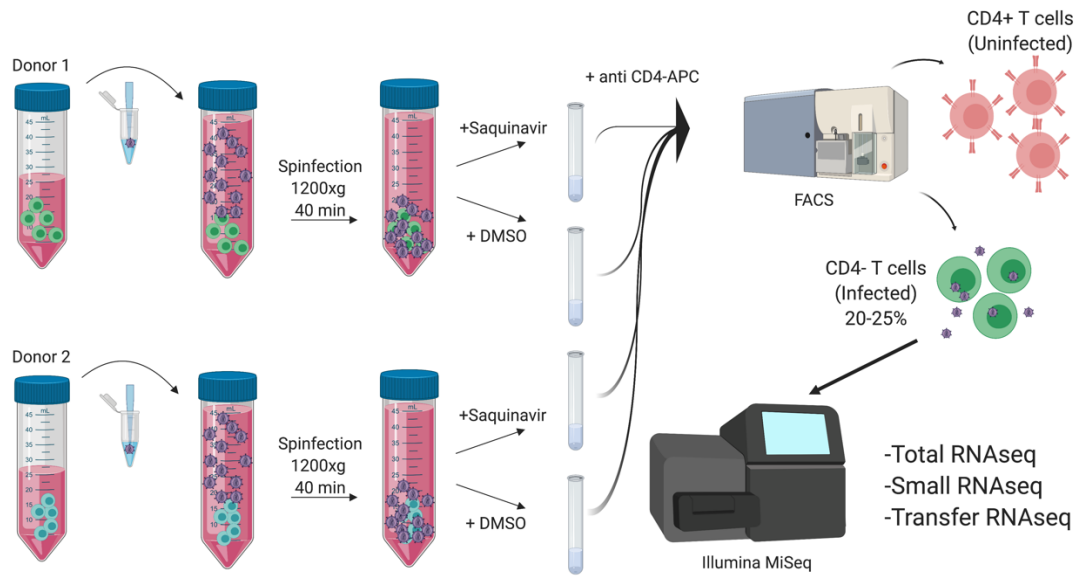


Figure 2.6 | Experimental design of CD4⁺ T cell Infection and Sorting.

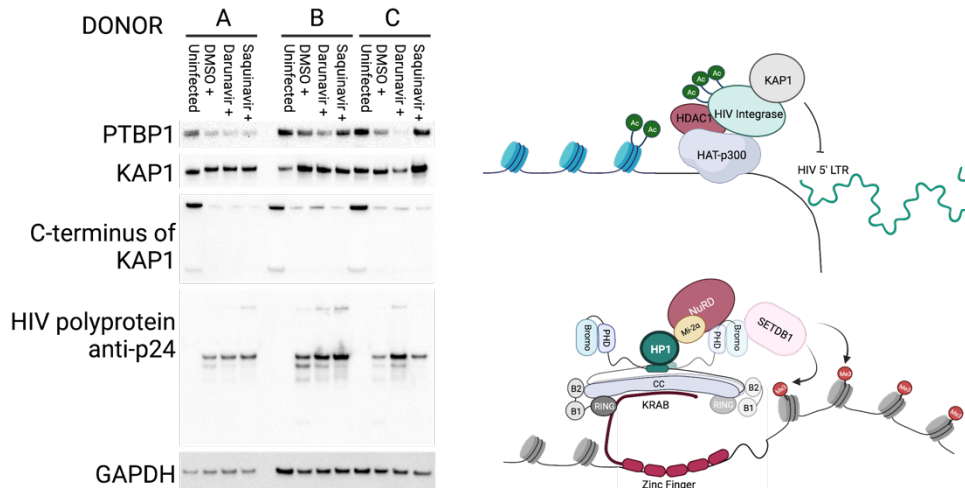
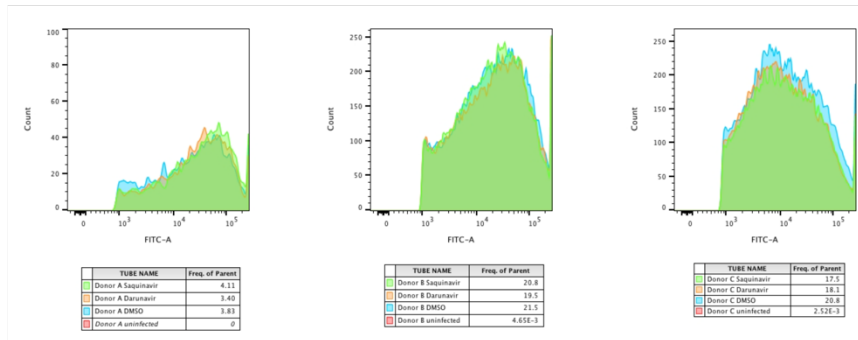


Figure 2.7 | Evaluation of host substrate degradation in CD4⁺ T cells.

A) The GFP⁺ populations of Infected CD4⁺ T cells under different inhibitor treatment. B) Western blot of infected CD4⁺ T cells for three donors. C) Model of KAP1 interaction with HIV Integrase. D) Model of KAP1 interaction with 5' LTR of integrated HIV provirus.

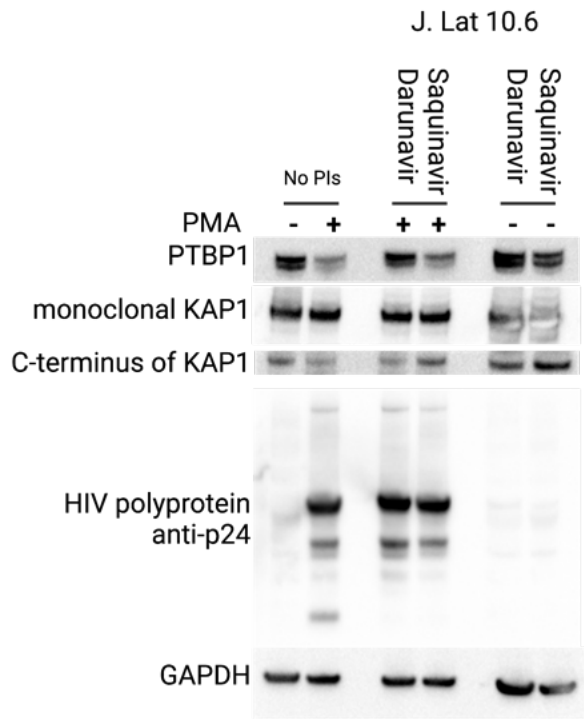


Figure 2.8 | Evaluation of endogenous host substrate degradation in J-Lat10.6.

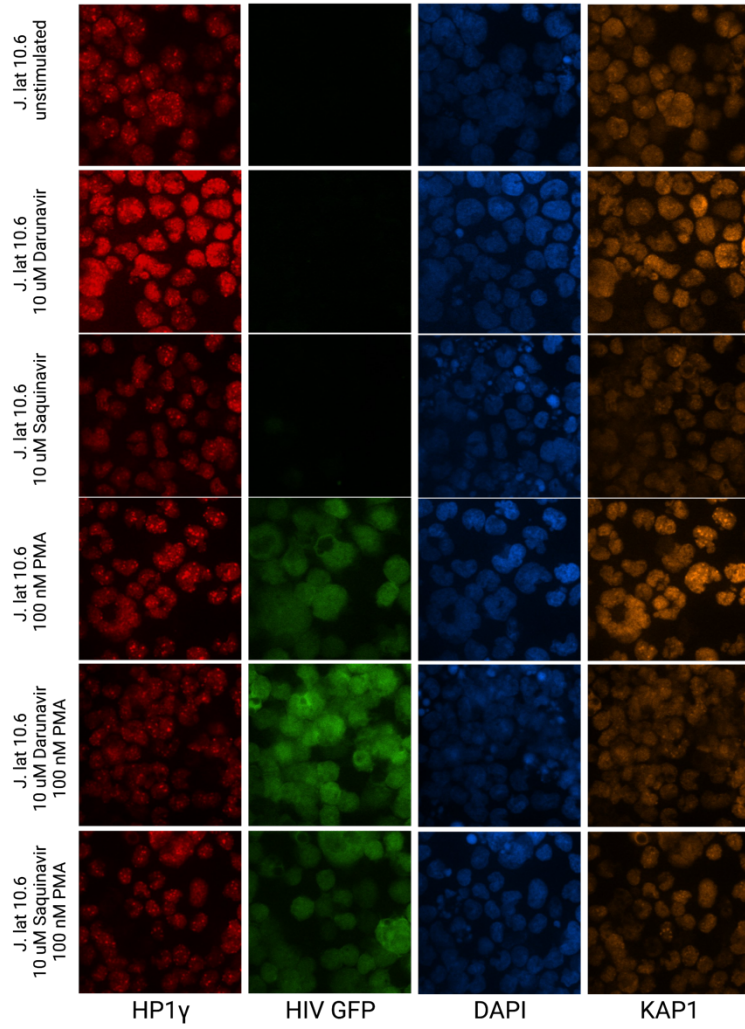


Figure 2.9 | Colocalization of KAP1 and HP1g during reactivation of HIV in J-Lat10.6.

2.6 References

1. Cheng, C.-T., Kuo, C.-Y. & Ann, D. K. KAPtain in charge of multiple missions: Emerging roles of KAP1. *World J. Biol. Chem.* **5**, 308–320 (2014).
2. Anjana Sharma, S. P. G. Fundamentals of Viruses and Their Proteases. *Viral Proteases and Their Inhibitors 1* (2017).
3. Pasquereau, S., Kumar, A., Abbas, W. & Herbein, G. Counteracting Akt Activation by HIV Protease Inhibitors in Monocytes/Macrophages. *Viruses* **10**, (2018).
4. Wang, Q. *et al.* CARD8 is an inflammasome sensor for HIV-1 protease activity. *Science* **371**, (2021).
5. Pablos, I. *et al.* Mechanistic insights into COVID-19 by global analysis of the SARS-CoV-2 3CLpro substrate degradome. *Cell Rep.* **37**, 109892 (2021).
6. Jäger, S. *et al.* Global landscape of HIV–human protein complexes. *Nature* **481**, 365–370 (2012).
7. Zhang, G., Fenyö, D. & Neubert, T. A. Evaluation of the variation in sample preparation for comparative proteomics using stable isotope labeling by amino acids in cell culture. *J. Proteome Res.* **8**, 1285–1292 (2009).
8. Miyamoto, A. *et al.* Subcellular localization of the RNA-binding protein PTBP1 is regulated by post-translational modifications in the RRM2 domain. *FASEB J.* **34**, 1–1 (2020).
9. Han, A. *et al.* De novo prediction of PTBP1 binding and splicing targets reveals unexpected features of its RNA recognition and function. *PLoS Comput. Biol.* **10**, e1003442 (2014).

10. Kosinski, P. A., Laughlin, J., Singh, K. & Covey, L. R. A complex containing polypyrimidine tract-binding protein is involved in regulating the stability of CD40 ligand (CD154) mRNA. *J. Immunol.* **170**, 979–988 (2003).
11. Vavassori, S., Shi, Y., Chen, C.-C., Ron, Y. & Covey, L. R. In vivo post-transcriptional regulation of CD154 in mouse CD4⁺ T cells. *Eur. J. Immunol.* **39**, 2224–2232 (2009).
12. Geng, G. *et al.* PTBP1 is necessary for dendritic cells to regulate T-cell homeostasis and antitumour immunity. *Immunology* **163**, 74–85 (2021).
13. Monzón-Casanova, E. *et al.* The RNA-binding protein PTBP1 is necessary for B cell selection in germinal centers. *Nat. Immunol.* **19**, 267–278 (2018).
14. Florez, P. M., Sessions, O. M., Wagner, E. J., Gromeier, M. & Garcia-Blanco, M. A. The polypyrimidine tract binding protein is required for efficient picornavirus gene expression and propagation. *J. Virol.* **79**, 6172–6179 (2005).
15. Allouch, A. *et al.* The TRIM family protein KAP1 inhibits HIV-1 integration. *Cell Host Microbe* **9**, 484–495 (2011).
16. Van den Bergh, R. *et al.* Transcriptome analysis of monocyte-HIV interactions. *Retrovirology* **7**, 53 (2010).
17. Ait-Ammar, A. *et al.* Inhibition of HIV-1 gene transcription by KAP1 in myeloid lineage. *Sci. Rep.* **11**, 2692 (2021).
18. Robbez-Masson, L. *et al.* The HUSH complex cooperates with TRIM28 to repress young retrotransposons and new genes. *Genome Res.* **28**, 836–845 (2018).
19. Chougui, G. & Margottin-Goguet, F. HUSH, a Link Between Intrinsic Immunity and HIV Latency. *Front. Microbiol.* **10**, 224 (2019).

20. Taura, M., Song, E., Ho, Y.-C. & Iwasaki, A. Apobec3A maintains HIV-1 latency through recruitment of epigenetic silencing machinery to the long terminal repeat. *Proc. Natl. Acad. Sci. U. S. A.* **116**, 2282–2289 (2019).
21. Price, A. J. *et al.* CPSF6 defines a conserved capsid interface that modulates HIV-1 replication. *PLoS Pathog.* **8**, e1002896 (2012).
22. Burdick, R. C. *et al.* HIV-1 uncoats in the nucleus near sites of integration. *Proc. Natl. Acad. Sci. U. S. A.* **117**, 5486–5493 (2020).
23. Selyutina, A., Persaud, M., Lee, K., KewalRamani, V. & Diaz-Griffero, F. Nuclear Import of the HIV-1 Core Precedes Reverse Transcription and Uncoating. *Cell Rep.* **32**, 108201 (2020).
24. Achuthan, V., Perreira, J. M., Ahn, J. J., Brass, A. L. & Engelman, A. N. Capsid-CPSF6 interaction: Master regulator of nuclear HIV-1 positioning and integration. *J. Life Sci.* **1**, 39–45 (2019).
25. Jacques, D. A. *et al.* HIV-1 uses dynamic capsid pores to import nucleotides and fuel encapsidated DNA synthesis. *Nature* **536**, 349–353 (2016).
26. Bonczkowski, P. *et al.* Protein expression from unintegrated HIV-1 DNA introduces bias in primary in vitro post-integration latency models. *Sci. Rep.* **6**, 38329 (2016).
27. Randolph, K., Hyder, U. & D’Orso, I. KAP1/TRIM28: Transcriptional Activator and/or Repressor of Viral and Cellular Programs? *Front. Cell. Infect. Microbiol.* **12**, (2022).
28. Bacon, C. W. *et al.* KAP1 Is a Chromatin Reader that Couples Steps of RNA Polymerase II Transcription to Sustain Oncogenic Programs. *Mol. Cell* **78**, 1133-1151.e14 (2020).

29. Hiragami-Hamada, K. *et al.* Dynamic and flexible H3K9me3 bridging via HP1 β dimerization establishes a plastic state of condensed chromatin. *Nat. Commun.* **7**, 11310 (2016).
30. Impens, F. *et al.* A catalogue of putative HIV-1 protease host cell substrates. *Biol. Chem.* **393**, 915–931 (2012).
31. Crawford, E. D. *et al.* The DegraBase: a database of proteolysis in healthy and apoptotic human cells. *Mol. Cell. Proteomics* **12**, 813–824 (2013).
32. Kumar, A. *et al.* Limited HIV-1 Reactivation in Resting CD4⁺ T cells from Aviremic Patients under Protease Inhibitors. *Sci. Rep.* **6**, 38313 (2016).
33. Hultquist, J. F. *et al.* A Cas9 Ribonucleoprotein Platform for Functional Genetic Studies of HIV-Host Interactions in Primary Human T Cells. *Cell Rep.* **17**, 1438–1452 (2016).
34. chip suspension protocol.pdf.
35. Kit, M. C. I. ChIP-IT Express Enzymatic.
36. NucleoSpin%20Gel%20and%20PCR%20Clean-up%20User%20Manual_Rev_04.pdf.
37. Tsang, M., Gantchev, J., Ghazawi, F. M. & Litvinov, I. V. Protocol for adhesion and immunostaining of lymphocytes and other non-adherent cells in culture. *Biotechniques* **63**, 230–233 (2017).

Chapter 3

Development of SARS-CoV-2 Major Protease Production and Replicon

3.1 Abstract

SARS-CoV-2 is the virus responsible for the worldwide pandemic of 2020. We produced recombinant SARS-CoV-2 Major protease (Mpro) to develop first line of defense protease inhibitors. Recombinant Mpro was used to design a FRET based assay for inhibitor screening with the Shoichet lab. Inhibitors were chosen by molecular docking screens against Mpro. A SARS-CoV-2 BSL-2 Replicon was designed to study virus host interactions and test inhibitors of Mpro *in vitro*.

3.2 Introduction

SARS-CoV-2 is a novel 29.9 kilobases (kb) RNA virus from the genera of *betacoronavirus*.³⁸ Corona viruses have a wide host range and can cause severe outbreaks in wildlife, livestock, and humans. The closest relative to SARS-CoV-2 has only 96% sequence identity and was isolated from bat populations screened in western China. It is thought to have been passaged in a different mammalian host than bats to have better adapted its virulence in humans. While the origin of SARS-CoV-2 may never be pinpointed, it has caused a significant burden on worldwide health and the economy. The development of small molecule inhibitors, biologic therapeutics, and scientific platforms/tools is an important focus of the scientific community.

In early March 2020 we aimed to produce recombinant viral proteins and a BSL-2 SARS-CoV-2 replicon to assay potential viral inhibitors and study viral protein interactions. Utilizing the published genome for the first SARS-CoV-2 alpha variant³⁸, we designed a series of plasmids for Mpro production. Similarly, we designed a SARS-CoV-2 replicon for assembly from 5 kbp fragments synthesized by Twist following the design of the SARS-1 replicon.³⁹ Following protocols from our own lab of SARS-1 Mpro⁴⁰ and others making corona virus

protease⁴¹⁻⁴⁴ we began trials of SARS-CoV-2 Mpro production. We tested the activity of the recombinant Mpro with 5 FRET-based peptide probes designed from the 11 Mpro proteolytic sites.^{38,45} The Shoichet lab has carried out a large-scale docking campaign to find new chemical entities that act as inhibitors for Mpro. Over 300,000,000 distinct chemical entities were computationally docked against a published high-resolution crystal structure of Mpro *in-silico*. Filtering and ranking these distinct chemical entities for their inhibitory potential, hundreds of non-covalent and covalent compounds were ordered for *in-vitro* inhibitory screening.

Our interest in developing a viral protease inhibitor extended beyond biochemical assays. We therefore needed to develop cellular assays. In the absence of available tools for a completely new pathogen we designed four replicon constructs for establishment of a SARS-CoV-2 replicon in mammalian cells.

Concurrently, a high-yield, robust expression system for recombinant major protease was optimized in the Craik lab, yielding reagent quantities of native, purified, and highly active Mpro. With reagent quantities of the major protease we optimized a specific and sensitive fluorescent-quencher peptide substrate (**Figure 3.1**). With reagent quantities of Mpro, an optimized fluorescent substrate, and hundreds of lead compounds, an inhibitor screen was carried out where active compounds were discovered and further characterized by their IC₅₀s. Currently, we have a handful of lead small-molecules with approximately 50µM IC₅₀s. We are currently analoguing these ‘parent’ molecules among others to do SAR and build more potent, novel inhibitors.

3.3 Results

3.3.1 Development and production of highly active recombinant Mpro

Maximal Mpro activity came from the Rolf Hilgenfeld construct (nsp5-RF). Expression with the four plasmids nsp5-GST (GT), nsp5-6xHis (BT), nsp5-MBP (MT), nsp5-SUMO (ST) from Ursula Schulze-Gahmen yielded variable expression and purity (**Figure 3.2**). The nsp5-GT construct expressed the most protein. The Mpro from GT was also the most stable during purification. The BT had the most minimal tag and expressed comparably to GT, however Mpro was much less stable during purification and would crash out. MT and ST did not express well. These constructs were abandoned. The SARS-CoV-2 Mpro purified from expression of GT or BT were 10-100x less active than reported Mpro.⁴¹ We determined the source of this reduced activity was the result of 2 amino acid residues at the N-terminus of the GT and BT sequences. The solvent accessibility of the serine at the N-terminus of Mpro was shown to be crucial to dimerization of Mpro.^{46,47} The dimer form of Mpro is significantly more active than the monomer and is the most accurate biochemical state for comparison with the viral activity during infection. The universal primer pairs from the LIC cloning protocol from UC Berkeley used to make the GT, BT, MT, and ST constructs all have a two amino acid extension and are therefore less active. The design of nsp5-BA (BA) was also insufficient for stable expression of Mpro and high proteolytic activity of the recombinant protein. BA lacked a large protein stabilizing tag like GST and relies on a TEV cleavage site at the N and C terminus of the purified protein. The nsp5-BA construct produced predominantly monomeric Mpro (**Figure 3.2**).

The Zhang, et al. construct pGEX-6p-1-Mpro contains a GST tag at the N terminus and a native self-cleavage site for Mpro as a linker between the GST tag and Mpro. At the C-terminus 3C protease cleavage site for removal the 6xHis tag. Following expression and purification with

the 6xHis tag this construct readily cleaves itself from the GST tag and can then be cleaved with 3C protease. The product is a tagless highly active dimeric Mpro.

3.3.2 SARS-CoV-2 Replicon Development

SARS-CoV-2 has been designated a BSL-3 pathogen because of its route of transmission and risk to the researcher. This greatly limits access of biochemists and medicinal chemists to testing efficacy of compounds. To eliminate risk to researchers in BSL-2 the viral structural proteins envelope (E), membrane (M), and spike (S) were removed to prevent the formation of virions. Our design includes open reading frame ORF 1a, ORF 1b, and nucleocapsid (N) protein (**Figure 3.3**). We created four SARS-CoV-2 replicon constructs in total. The first construct Nluc Short (NS) encodes a Nanoluc Luciferase and blasticidin (Nluc-BSD) fusion gene after orf 1b. The second construct Nluc Long (NL) also encodes Nuc-BSD fusion gene after orf1 b as well as ORF 6-8. The third construct GFP Short (GS) encodes a GFP-blasticidin (GFP-BSD) fusion gene after orf 1b. The fourth construct GFP Long (GL) encodes a GFP-BSD fusion gene after ORF 1b and ORF 6-8. The inclusion of N protein in the replicon is essential for continuous high expression as seen by Ge, F. et al.³⁹ The six 5 kbp synthetic gene fragments GB1, GB2, GB3, GB4, GB5, and GB6 were assembled using golden gate cloning into larger fragments GB12 and GB3456 before assembly of the full length transcription template (**Figure 3.3, Figure 3.4**).^{48,49}

Several in vitro transcription (IVT) kits were tested to find the highest and best quality full length RNA transcript (**Figure 3.4**). The mMessage MACHINE™ T7 transcription kit from Thermo Fisher did not produce any transcript. The HiScribe™ T7 ARCA mRNA Kit produced a significantly shorter product than the desired 25 kbp RNA transcript. The T7 RiboMAX™ Promega Kit produced a small quantity of appropriately sized RNA that could be used for

transfection and electroporation. Our IVT RNA product was comparable or better to previously reported IVT RNA transcripts used to create SARS-CoV replicons.^{39,50,51}

We tested transfection or electroporation of viral RNA constructs supplemented with N protein RNA into many mammalian cell types including Vero E6, BHK21, HEK293T, HeLa, A549, Huh 7, and Huh 7.5.1 (**Figure 3.4**). After 4 days following transfection or electroporation most cell lines were 5-10% fluorescent if GS or GL constructs were transfected/electroporated. However, no luciferase activity was ever detected from the NS or NL constructs. Cells were treated with blasticidin for ~20 passages to select for SARS-CoV-2 replicon establishment. Vero E6 cells tolerated electroporation best and GFP signal increased after blasticidin selection. Bulk RNA isolated from two GFP positive clones (C1 and C2) of the GS construct were evaluated with real-time quantitative PCR (RT-qPCR) for the presence of orf 1a orf 1b and BSD (**Figure 3.5**). Both GS clones GSC1 and GSC2 had RNA of orf 1a, orf 1b, and BSD present in the cytoplasm. The genomic DNA isolated from GSC1 and GSC2 did not have integrated viral N protein DNA or integrated blasticidin resistance gene DNA. RT-qPCR of GSC1 and GSC2 indicate the barest requirements of a replicon. Unfortunately, the population of cells expressing GFP was only between 5-20%.

3.4 Discussion

Production and purification of Mpro is essential to its study and the development of corona virus protease inhibitors. We found that similarly to SARS-CoV-1 Mpro the N-terminus is highly sensitive to modification. The best construct for recombinant protein production utilized a large n-terminal tag and an endogenous cleavage site to create a native neo N-termini following translation in *E. coli*. The effect of N-terminal modification has been noted by et al

when trying to crystallize SARS-CoV-1 Mpro with inhibitor compounds. The homology of SARS-CoV-1 to SARS-CoV-2 Mpro is only 60%. While there is significant sequence modification a similar proteolytic signature is seen between these two proteases.

The expression of Mpro was greatly improved by culturing at higher temperatures (37°C) and inducing expression over a shorter period of time (5 hours) compared with conventional recombinant proteins (~16 °C and 18 hours). This is consistent with the expression protocols of other viral proteases. It appears that the expression of viral proteases in *E. coli* over long time periods results in the degradation of the protein product.

Many other groups have had limited success with establishment of a SARS-CoV-2 replicon. Similar construct designs were attempted and published. These groups were able to get low GFP expression for 1-2 months or 20-30 passages but fluorescence and RT-qPCR shown decline like ours. Further attempts to make a SARS-CoV-2 replicon may need the aid of N-protein expressing cell lines and the trial of other reporters and antibiotic selection agents. In future we will try GFP and nLuc zeocin fusion genes.

A SARS-CoV-2 Replicon would not only aid in drug development but enhance the study of SARS-CoV-2 interactions with the host. A pipeline for creating a SARS-CoV-2 replicon would enhance the study of rapidly emerging variants by allowing many more scientists to study SARS-CoV-2 mutations in the entire virus not just spike. It is difficult to study new variants in cell model outside of BSL3 facilities. Currently as new variants arise it is difficult to predict whether they will significantly impact the clinic and to understand why those mutations are so advantageous to the virus. While some mutations alter viral fitness by increasing the speed of replication other mutations likely engage the host innate immune system differently to better incapacitate cells.

3.5 Materials and Methods

E. coli strains and bacterial expression plasmids

All bacterial expression plasmids were transformed into One Shot™ BL21(DE3)pLysS Chemically Competent *E. coli* (Thermo). We received four plasmids from Ursula Schulze-Gahmen at the Gladstone Institute encoding non-structural protein 5 (nsp5). Nsp5 codon optimized for *E. coli* was synthesized (Genscript). Nsp5 was cloned into pET His6 GST TEV LIC cloning vector (2G-T) (Addgene 29707), pET His6 TEV LIC cloning vector (2B-T) (Addgene 29666), pET His6 MBP TEV LIC cloning vector (2M-T) (Addgene 29708), pET His6 Sumo TEV LIC cloning vector (2S-T) (Addgene 29711). We received nsp5 cloned into pGEX-6p-1 with a N-terminal GST tag and Mpro cleavage-site SAVLQ↓SGFRK from Rolf Hilgenfeld.⁴¹ Nsp5-BA is Mpro cloned into pET28a(+) with a C-terminal TEV cleavage site and kanamycin resistance (TWIST).

Expression and purification of Mpro

The expression for Mpro in *E. coli* was previously described.⁴¹ In brief a transformed clone of BL21(DE3)pLysS *E. coli* was added to a 50 mL culture of 2xYT media supplemented with 2% glucose and ampicillin grown overnight at 37°C. 30 mL of overnight cultures were used to inoculate 1 L of 2xYT media ampicillin or appropriate antibiotic. A large 1 L culture was shaken at 225 rpm at 37°C. The 1 L culture was induced when culture OD₆₀₀ reached 0.8 (after ~3 hours) by adding 1 mL of 1 M IPTG. After 5 hours of expression at 37°C the culture was centrifuged at 9,000 rpm for 15 min. Supernatant was discarded and cell pellet stored at -80°C. The frozen cell pellet was thawed on ice in 30 mL of 20 mM TRIS 150 mM NaCl pH 7.4 buffer. The resuspended sample was sonicated for 5 mins or until lysis was complete. Sonicated cell lysate was centrifuged at 15000 rpm for 30 mins. 3 mL of Ni-NTA beads were incubated with

the supernatant for 1 hour at 4°C. Beads were centrifuged at 200 rpm for 2 mins. Supernatant was stored at 4°C. Ni-NTA beads were washed with ~3 column volumes of wash buffer (20 mM TRIS 150 mM NaCl 20 mM imidazole). 6xHis tagged protein was eluted with 1 mL fractions of elution buffer (20 mM TRIS 150 mM NaCl 350 mM Imidazole). Sample was immediately buffer exchanged into 20% Glycerol 20 mM TRIS 150 mM NaCl pH 7.4 using Amicon concentrators. 3C protease was added in a 5:1 ratio of Mpro to 3C protease and incubated overnight at 4°C. A 2 L of culture yielded 2.28 mg of Mpro following 3C cleavage. 3C protease and 6xHis-tag were removed by incubation with Ni-NTA beads. Monomer was isolated with a MonoQ column. Buffer A: 20 mM Tris 1 mM DTT (fresh) pH 8. Buffer B: 1 M NaCl 20 mM Tris 1 mM DTT (fresh) pH 8. MonoQ column equilibrated with buffer A and eluted with a linear gradient of Buffer B 0 mM to 500 mM NaCl over 20 column volumes.

SARS-CoV-2 replicon materials

All gene fragments were synthesized and purchased from Twist Bioscience, San Francisco.

Electroporation of mammalian cells

Electroporation of mammalian cells was done using a Lonza Amaxa 4D Nucleofector and following suggested protocols for the cell type.

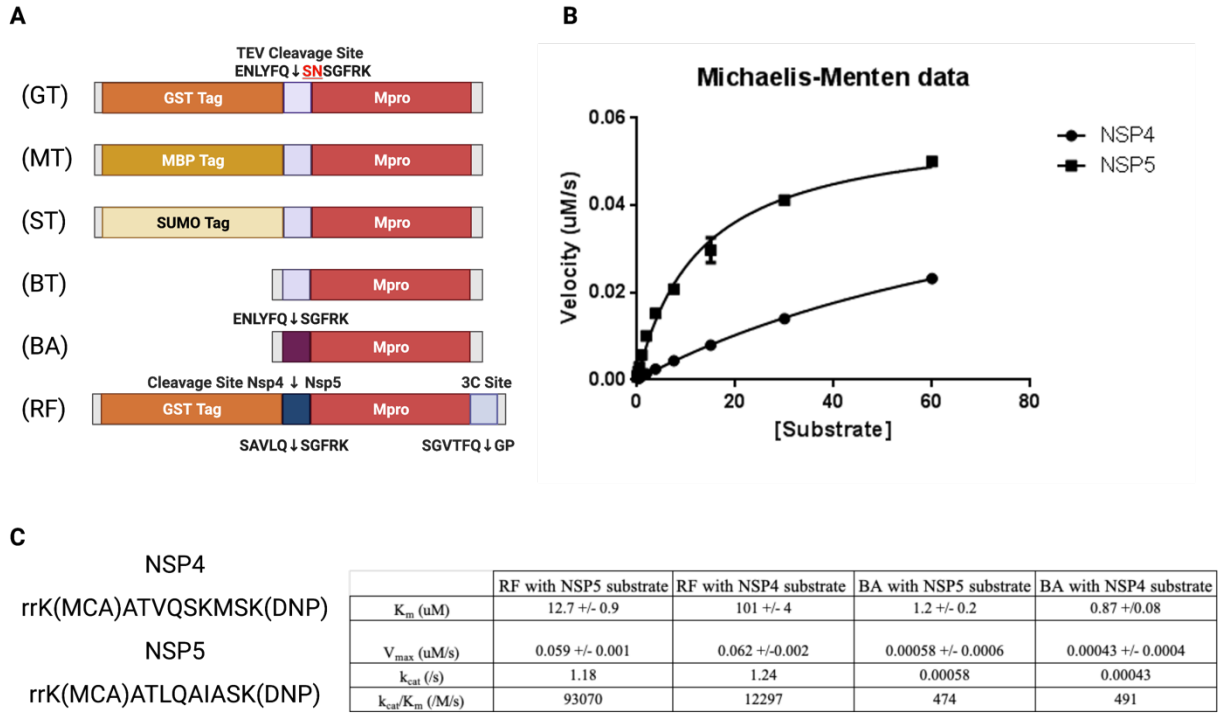


Figure 3.1 | Mpro expression constructs and activity

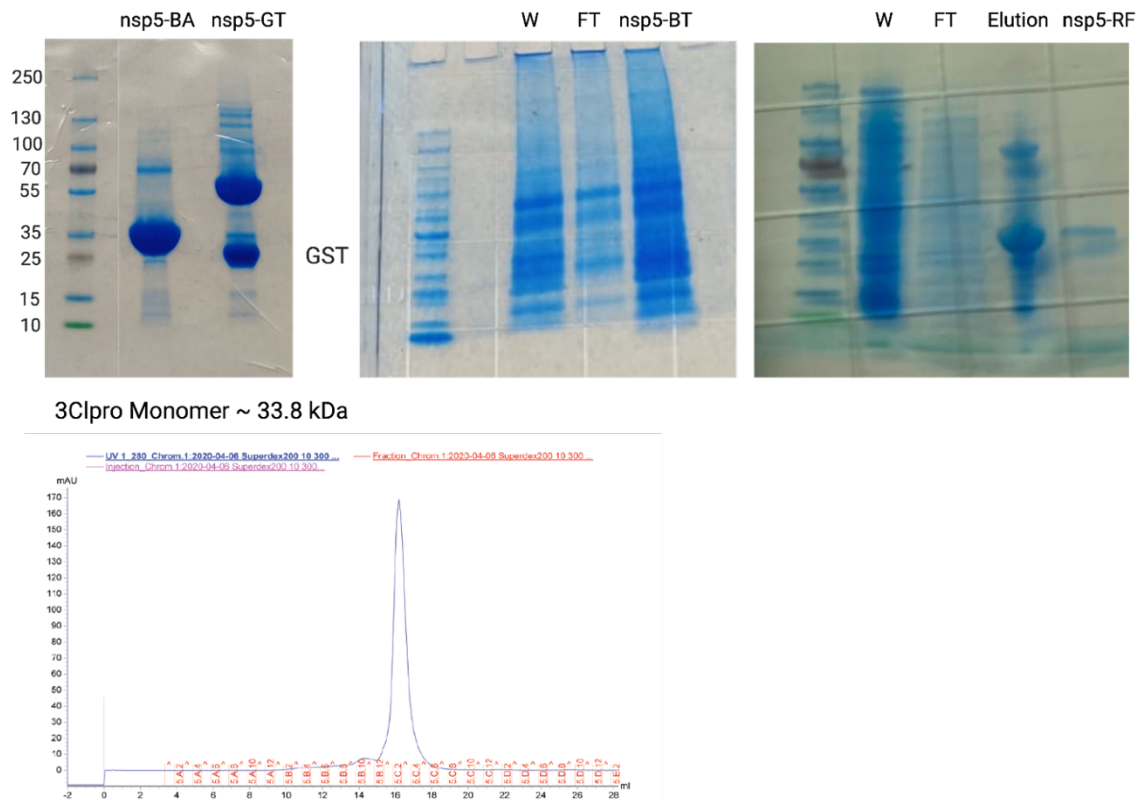


Figure 3.2 | Expression and purification of different Mpro constructs.

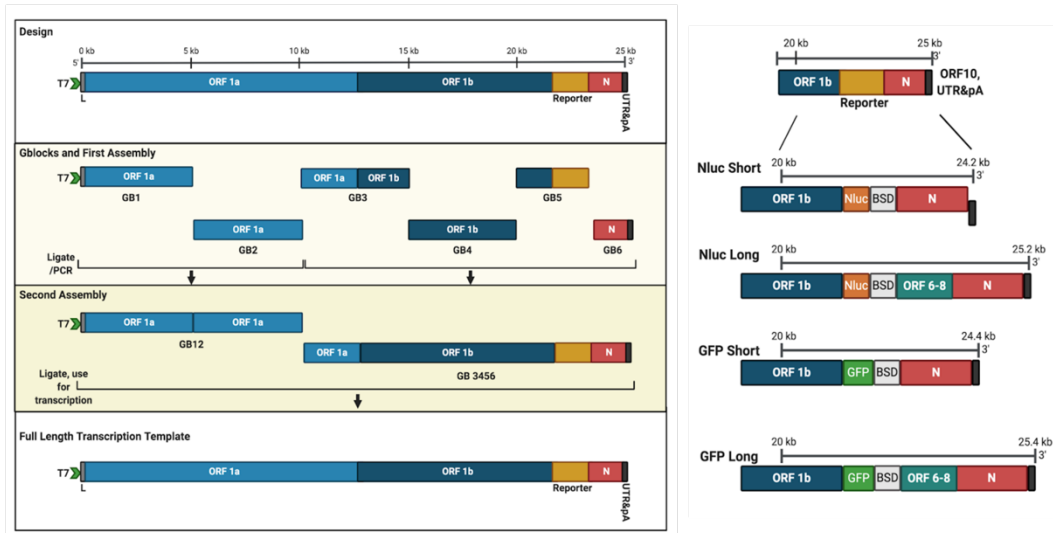


Figure 3.3 | Design of four SARS-CoV-2 replicon RNA constructs.

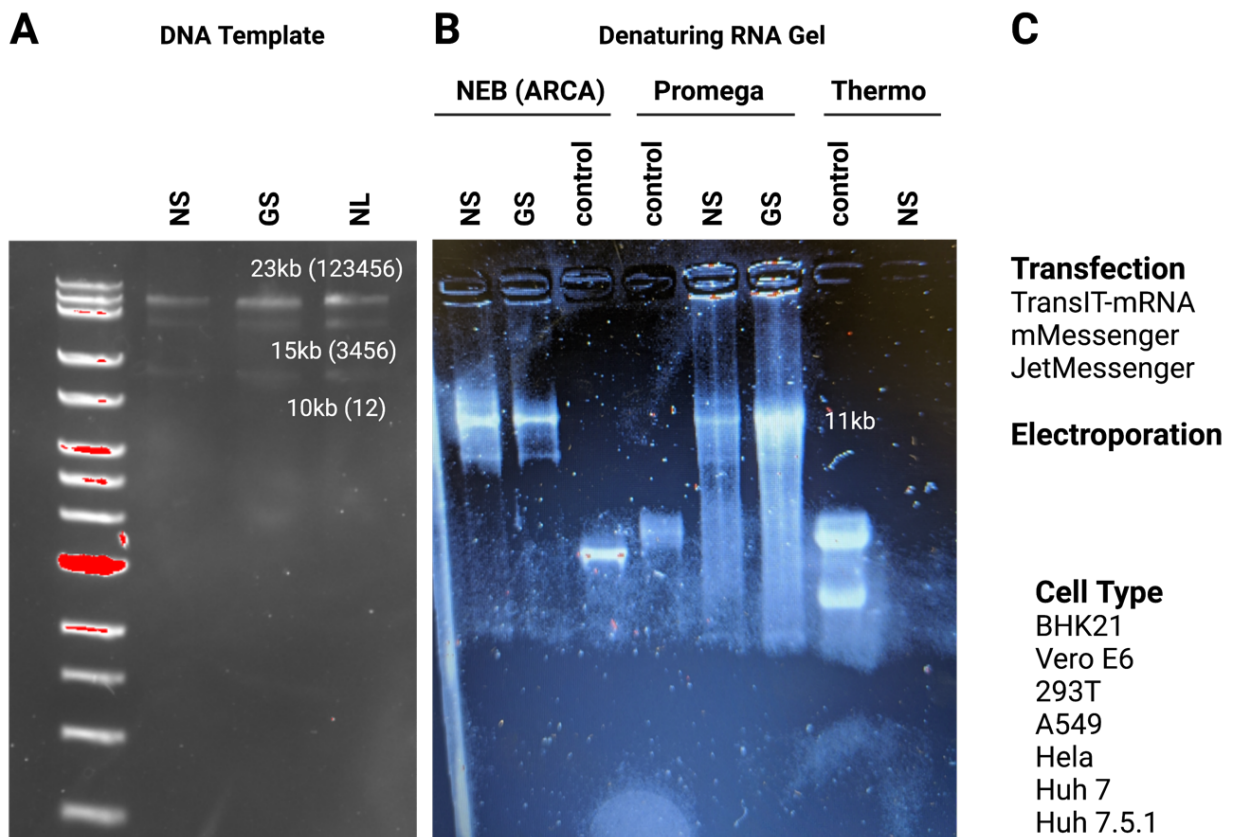


Figure 3.4 | SARS-CoV-2 DNA transcript assembly and IVT trials.

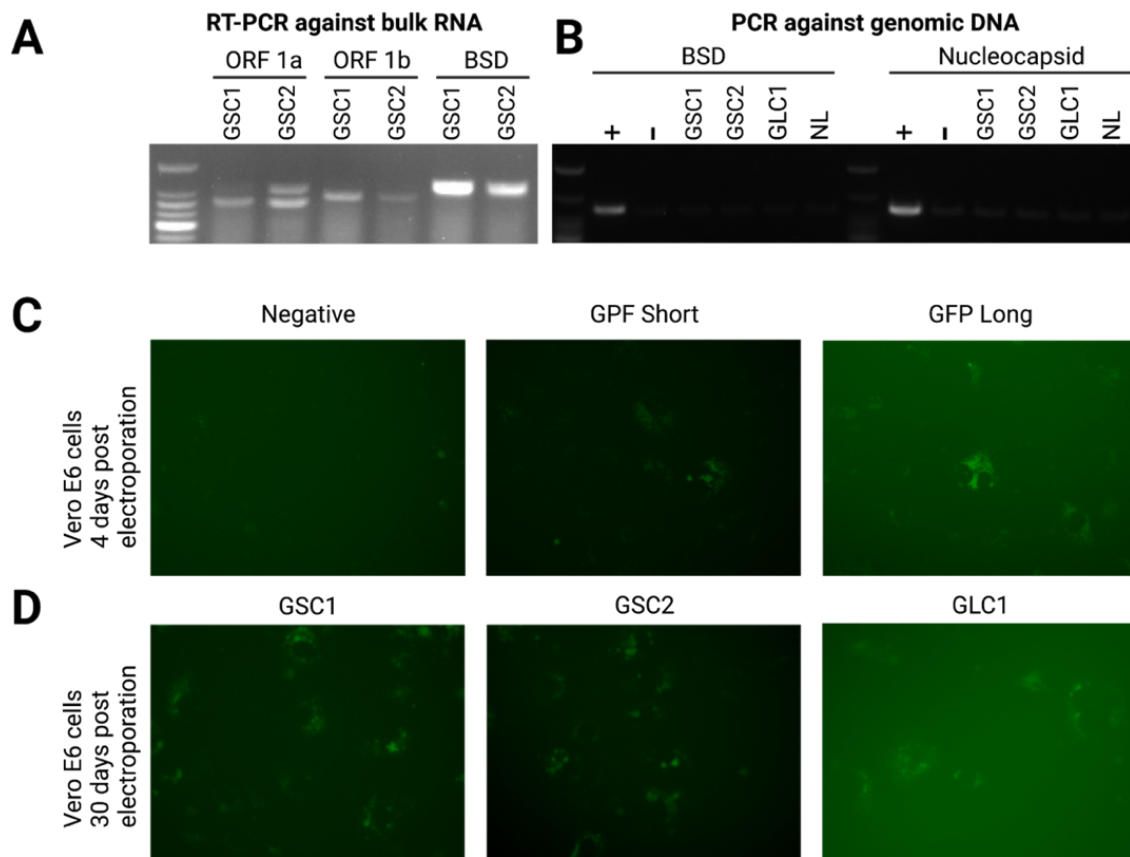


Figure 3.5 | GFP positive Vero E6 cells and RT-qPCR of bulk RNA and Genomic DNA.

3.6 References

1. Chan, J. F.-W. *et al.* Genomic characterization of the 2019 novel human-pathogenic coronavirus isolated from a patient with atypical pneumonia after visiting Wuhan. *Emerg. Microbes Infect.* **9**, 221–236 (2020).
2. Ge, F., Luo, Y., Liew, P. X. & Hung, E. Derivation of a novel SARS-coronavirus replicon cell line and its application for anti-SARS drug screening. *Virology* **360**, 150–158 (2007).
3. Goetz, D. H. *et al.* Substrate specificity profiling and identification of a new class of inhibitor for the major protease of the SARS coronavirus. *Biochemistry* **46**, 8744–8752 (2007).
4. Zhang, L. *et al.* Crystal structure of SARS-CoV-2 main protease provides a basis for design of improved α -ketoamide inhibitors. *Science* **368**, 409–412 (2020).
5. Ye, G. *et al.* Structural basis for the dimerization and substrate recognition specificity of porcine epidemic diarrhea virus 3C-like protease. *Virology* **494**, 225–235 (2016).
6. Ye, G. *et al.* Structural Basis for Inhibiting Porcine Epidemic Diarrhea Virus Replication with the 3C-Like Protease Inhibitor GC376. *Viruses* **12**, (2020).
7. Wang, F. *et al.* Michael Acceptor-Based Peptidomimetic Inhibitor of Main Protease from Porcine Epidemic Diarrhea Virus. *J. Med. Chem.* **60**, 3212–3216 (2017).
8. Gordon, D. E. *et al.* A SARS-CoV-2 protein interaction map reveals targets for drug repurposing. *Nature* **583**, 459–468 (2020).
9. Goyal, B. & Goyal, D. Targeting the Dimerization of the Main Protease of Coronaviruses: A Potential Broad-Spectrum Therapeutic Strategy. *ACS Comb. Sci.* **22**, 297–305 (2020).

10. Cheng, S.-C., Chang, G.-G. & Chou, C.-Y. Mutation of Glu-166 blocks the substrate-induced dimerization of SARS coronavirus main protease. *Biophys. J.* **98**, 1327–1336 (2010).
11. Cermak, T. *et al.* Efficient design and assembly of custom TALEN and other TAL effector-based constructs for DNA targeting. *Nucleic Acids Res.* **39**, e82 (2011).
12. Engler, C., Kandzia, R. & Marillonnet, S. A one pot, one step, precision cloning method with high throughput capability. *PLoS One* **3**, e3647 (2008).
13. Xie, X. *et al.* An Infectious cDNA Clone of SARS-CoV-2. *Cell Host Microbe* **27**, 841-848.e3 (2020).
14. Hertzog, T. *et al.* Rapid identification of coronavirus replicase inhibitors using a selectable replicon RNA. *J. Gen. Virol.* **85**, 1717–1725 (2004).

Chapter 4

Platform to Discover Protease-Activated Antibiotics and Application to Siderophore–Antibiotic Conjugates

4.1 Abstract

Here we present a platform for discovery of protease-activated prodrugs and apply it to antibiotics that target Gram-negative bacteria. Because cleavable linkers for prodrugs had not been developed for bacterial proteases, we used substrate phage to discover substrates for proteases found in the bacterial periplasm. Rather than focusing on a single protease, we used a periplasmic extract of *E. coli* to find sequences with the greatest susceptibility to the endogenous mixture of periplasmic proteases. Using a fluorescence assay, candidate sequences were evaluated to identify substrates that release native amine-containing payloads. We next designed conjugates consisting of¹ an N-terminal siderophore to facilitate uptake,² a protease-cleavable linker, and³ an amine-containing antibiotic. Using this strategy, we converted daptomycin—which by itself is active only against Gram-positive bacteria—into an antibiotic capable of targeting Gram-negative *Acinetobacter* species. We similarly demonstrated siderophore-facilitated delivery of oxazolidinone and macrolide antibiotics into a number of Gram-negative species. These results illustrate this platform’s utility for development of protease-activated prodrugs, including Trojan horse antibiotics.

4.2 Introduction

The well-recognized term, “ESKAPEE” (previously ESKAPE),¹ encompasses the names of seven species of clinically relevant pathogens (*Enterococcus faecium*, *Staphylococcus aureus*, *Klebsiella pneumoniae*, *Acinetobacter baumannii*, *Pseudomonas aeruginosa*, *Enterobacter spp.*, and *Escherichia coli*) that are associated with resistance to commonly prescribed antibiotics and are largely responsible for the world’s nosocomial infections.² Five of these pathogens are Gram-negative species, whose outer membrane and associated resistance–nodulation–cell division (RND) efflux pumps render them resistant to many classes of antibiotics.^{3,4} Indeed, the outer

membrane shields the bacteria from molecules that are unable to pass through porins,^{5,6} providing an effective barrier to many molecules that would otherwise be effective antibiotics against these pathogens.⁷⁻⁹ Gram-negative therapies can be delivered by siderophore-mediated antibiotic delivery using Nature's Trojan-horse approach.¹⁰⁻²⁴ Siderophores are small-molecule chelators that are produced by bacteria to sequester Fe(III),²⁵⁻²⁷ which is an essential nutrient required for bacterial growth and virulence.²⁸⁻³⁰ In the case of Gram-negative pathogens, outer membrane proteins (e.g., TonB-dependent transporters)³¹ bind ferric siderophores and provide opportunities for their active transport into the periplasm,³² where they may undergo further translocation into the cytoplasm by alternate transport mechanisms depending on the siderophore and the species of bacteria.³³⁻³⁸ Owing to the promiscuity of their transport systems, bacteria also use siderophores in warfare against other microbes.^{32,39-41} For example, streptomycetes produce albomycins, which are natural siderophore-antibiotic conjugates (SACs) and highly effective antibiotics against Gram-negative Enterobacteriaceae.⁴² Albomycins are recognized by siderophore uptake machinery, transported into the cytoplasm, and activated by peptidase N, which cleaves the N-terminal serine-amide bond and releases the serine-bound t-RNA synthetase inhibitor to bind to its target.⁴³⁻⁵⁵ Inspired by Nature's strategy, we develop an unbiased platform for the discovery of linkers that are cleaved by periplasmic proteases,⁵⁶ which demonstrates that this platform can produce SACs with both broad and narrow spectra of activity. We target proteases in the periplasm, a compartment that contains >20 known proteases, because all SACs pass through the periplasm.

There are two categories of SACs, depending on the type of linker they possess: non-cleavable and cleavable. There has been significant progress in the development of non-cleavable SACs,⁵⁷⁻⁵⁹ with the first siderophore- β -lactam conjugate Fetroja (cefiderocol) recently

approved by the FDA.⁶⁰ However, their use is often limited to periplasmic-targeting antibiotics (e.g., daptomycin, vancomycin, and β -lactams). The few examples of cytoplasmic-targeting, non-cleavable SACs may be less effective than the parent antibiotic for two reasons^{61–74}: (1) the conjugate may not pass through the inner membrane to reach the cytoplasm, or (2) the bulky siderophore component may interfere with binding to the target.^{15,32,62} Therefore, cleavable linkers are traditionally thought to be required for SAC compatibility with cytoplasmic-targeting antibiotics.⁵⁷ The majority of Gram positive antibiotics are cytoplasmic-targeting and may require a cleavable linker to be converted into SACs for Gram-negative pathogens.^{32,57,75} We show that protease-cleavable linkers improve the activity of SACs containing periplasmic- and cytoplasmic-targeting antibiotics.

Over the past 30 years, only a few cleavable linker strategies have been developed for SACs and a number of challenges remain.^{57,58,61–67,76–83} Despite optimization for hydrolytic stability,⁸⁰ ester linkers for SACs (**Figure 4.1**) are susceptible to premature cleavage prior to bacterial-cell entry.^{61–63,65–67,80,83} SACs with disulfide (**Figure 4.1**) and trimethyl-lock linkers based on reduction- (**Figure 4.1**), phosphatase (**Figure 4.1**), and esterase-triggered cleavage mechanisms were less active than the parent antibiotic.^{64–66,81,84,85} Recent work by Nolan demonstrated that cytoplasmic siderophore degradation by the siderophore-hydrolase IroD confers high activity to a conjugate with a non-cleavable linker.⁸² Miller and co-workers developed a dual drug conjugate with the cleavable β -lactam linker E.⁷⁶ However, more alternatives are needed as the physiological instability of β -lactams can lead to hypersensitivity and allergic reactions in patients.⁸⁶ Protease cleavable linkers have the potential to overcome the limitations of cleavable SACs reported to date.

With few exceptions,^{67,76,83} cleavable SACs have incorporated a DNA-gyrase-inhibiting fluoroquinolone antibiotic, ciprofloxacin or norfloxacin,^{87,88} which are already active against Gram-negative pathogens. These SACs provide a method to study siderophore-mediated antibiotic delivery because release of the antibiotic from the conjugate is often required to observe significant growth inhibition.^{57,61–66,80,82,84,85} In line with this trend, we investigate a macrolide that is already active in Gram-negative bacteria as one strategy to interrogate SAC cleavage.

Protease-cleavable SACs are classified as prodrugs.^{89–91} Protease-activated prodrugs that are cleaved by mammalian proteases include antibody–drug conjugates,^{92–98} antibody–antibiotic conjugates,^{99,100} peptide–drug conjugates,¹⁰¹ macromolecular prodrugs,^{89,102} and protease-activatable photosensitizers,^{103,104} with the cathepsin B-sensitive valyl-citrulline (ValCit) linker being the most successful and widely known.^{95,97} Although most protease-activated prodrugs target cancer, antibody–antibiotic conjugates are undergoing clinical trials for intracellular bacterial infections associated with difficult to treat persisters.^{99,100} However, antibody–antibiotic conjugates have been limited to the treatment of intracellular *S. aureus*, using a linker that was optimized for cleavage by mammalian proteases. Protease-activated prodrugs that are activated by bacterial proteases would clearly be of value for treatment of a variety of Gram-negative bacterial infections.

Several technologies have been developed to screen libraries of protease substrates,¹⁰⁵ including indexed arrays of fluorogenic substrates,^{106,107} positional scanning of synthetic combinatorial libraries,^{108,109} substrate phage,^{110,111} multiplex substrate profiling by mass spectrometry,^{105,112–114} and others.^{106,115–119} Given the large size of achievable libraries, substrate phage display¹¹⁰ provides an unbiased selection tool to discover cleavable linkers for SACs.

Conventional phage display has been used in vitro and in vivo to design targeted-peptide conjugates.^{120–126} For example, Wilfred van der Donk used phage display to select for ribosomally synthesized and post translationally modified peptides (RiPPs) that bind to lipid II.¹²⁶ However, “substrate phage display” has not been applied to prodrug development,¹¹¹ and its use for profiling complex biological mixtures is limited.^{127,128} Here, we extend substrate phage display to identify cleavable peptide linkers for SACs that are activated by periplasmic proteases.

In designing protease-activated prodrugs, there are advantages to targeting multiple proteases over an individual protease.^{129–131} For example, in vivo deletion mutants of cathepsin B retain the ability to release prodrugs from the combined activity of several proteases.^{132,133} Indeed, targeting multiple proteases might minimize resistance when designing antibiotic prodrugs. Thus, we screened broadly for peptides that are cleaved by the proteases present in an unfractionated periplasmic extract.

4.3 Results

4.3.1 Substrate Phage Display Leads to WSPKYM-RFG and WSWC-KWASG for Periplasmic Cleavage.

To discover efficient peptide substrates using the method of substrate phage,¹¹⁰ we built a random hexapeptide library genetically fused to the pIII gene of M13 bacteriophage. A phagemid vector allows monovalent display of the corresponding protein on the tip of the phage. A GGS spacer was incorporated at each end of the randomized peptide to enhance flexibility. An AviTag sequence was also incorporated at the N-terminus for biotinylation of the displayed peptides. The biotin is used to immobilize the phage library on a streptavidin-coated surface, and a protease

can then cleave at favorable peptide sequences. Proteolysis releases the phage, which are then amplified and sequenced to determine the favorable substrates for the protease of interest.

The process of “biopanning” entails the following steps: (1) enzymatic biotinylation of the AviTag sequence,^{134,135} (2) immobilization of the biotinylated library on streptavidin 96- well plates, (3) cleavage of the immobilized library by incubation with the periplasmic extract of *E. coli K12 MG1655* at 37 °C, (4) amplification of the eluted phage using *E. coli TG-1* cells, and (5) isolation and purification of phage for the next round of selection. The periplasmic extract used in panning was obtained by osmotic shock of *E. coli K12 MG1655*.¹³⁶ We carried out four rounds of selection, with the stringency being increased with each succeeding round by reducing extract concentration and decreasing the incubation time. The phagemids from the input library and final round of biopanning were isolated, barcoded, and submitted for next generation sequencing.¹³⁷ Sequences for further characterization were ranked based on the extent of enrichment relative to the original library (**Table 4.1**).

Six highly enriched sequences (SKNQLSGG, SGSDSSVG, SNHADVHG, SKSEMLSG, SWCKWASG, and SPKYMRFG) were synthesized with a Ser at the N-terminus and a Gly at the C-terminus to mimic the GGS spacers in the phage library. A tryptophan was added to the N-terminus to facilitate detection by HPLC. Each peptide was found to be cleaved to varying extents following treatment with periplasmic extract for 18 h at 37 °C. The cleavage sites and extent of proteolysis were evaluated by LC/MS, which revealed that the sequences WSWC-KWASG and WSPKYM-RFG may be optimal linkers for cleavable SACs. In addition to their promising cleavage profiles, the presence of these sequences in the original library contributed to their selection as potential linker candidates. In protease substrate nomenclature, the Cys and Met residues at the N-terminal side of the scissile bond for WSWC-KWASG and WSPKYM-

RFG are designated as the P1 positions, while the Lys and Arg residues at the C-terminal side are designated as the P1' positions. Although the residues on the P' side are sometimes important for efficient cleavage,¹³⁸ this is not always the case.¹³⁹

4.3.2 WSPKYM Conjugates Are Efficiently Cleaved without a P' Peptide.

With the candidate sequences WSWC-KWASG and WSPKYM-RFG in-hand, we asked whether the residues on the C-terminal P' sequence were required for proteolysis (**Figure 4.2**). To probe this question, we used a solid-phase method to synthesize fluorescent substrates. A 7-amino-4-carbamoylmethylcoumarin (acc)^{140,141} was coupled directly to the P1 Cys and Met residues as an antibiotic surrogate. We were indeed pleased to find that the treatment of peptide 1 (25 μ M) with periplasmic extract led to rapid release of the fluorescent amino coumarin. HPLC analysis also showed the substrate was fully consumed at the end of the reaction. As expected, the rate of cleavage was dependent on the substrate concentration, showing partial saturation at concentrations over 12.5 μ M. However, we did not attempt to fit a value of K_M , given the heterogeneous nature of the proteolytic composition of the extract. On the other hand, the amount of acc released from peptide 2 (WSWC-coumarin) was comparably insignificant under these conditions (**Figure 4.2**). Thus, WSPKYM was determined to be more suitable than WSWC for the development of cleavable SACs.

To determine the type of protease responsible for acc release in a periplasmic extract of *E. coli*, we evaluated a variety of protease inhibitors, which revealed that the enzymes of interest include a metalloprotease or a calcium dependent protease. We also used alanine positional scanning to evaluate the sequence dependence for efficient cleavage. The starting peptide Ac-WSPKYM-acc (1) was the most efficient substrate. Individual substitutions of Ala at Tyr (P2),

Trp (P6), and Lys (P3) resulted in large decreases in rate, while substitutions at other positions resulted in an approximately 2-fold decrease in rate. These findings indicate that substrate phage was effective in discovering an optimized substrate for cleavage.

We also examined the ability of human and mouse serum to cleave 1. We were pleased to find that under conditions where 1 is rapidly cleaved by periplasmic extract, human serum released acc with a half-life of approximately 3–4h. However, the compound is cleaved more rapidly by mouse serum, indicating that some optimization would be necessary for applications using mouse models.

4.3.3 Design and Synthesis of SACs That Incorporate Solithromycin, Daptomycin, and Eperezolid-NH₂.

To explore the versatility of SACs, we selected three structurally and mechanistically diverse antibiotics that act on targets in either the periplasm or the cytoplasm. Each antibiotic has an amine, which can be unmasked upon proteolysis of the WSPKYM linker. The lipopeptide daptomycin (**4**) interacts with the cytoplasmic membrane in Gram-positive bacteria, leading to increased membrane permeability and membrane depolarization.^{142–144} However, it is ineffective against Gram negative bacteria and challenging to functionalize without loss of potency.¹⁴⁵ Nevertheless, the Miller group has shown that daptomycin can gain activity in Gram-negative species if conjugated to a siderophore with a non-cleavable linker.^{58,59} Here, we examine the use of a protease-cleavable linker for this system.

We also chose two ribosomal protein synthesis inhibitors, amino-oxazolidinone **5** and solithromycin **6**, as examples of antibiotics that must gain access to the cytoplasm to be active.⁷⁶ Since both oxazolidinones and macrolides bind deep within the large ribosomal subunit in fairly

occluded binding sites, siderophore conjugates without cleavable linkers have been met with limited success, potentially due to interference of the linkers with binding.^{32,57,75,146,147} Our strategy would avoid this complication by enabling release of the parent antibiotics.

For attachment to the N-terminal side of the linker, we sought a siderophore that was synthetically accessible and compatible with a variety of bacterial siderophore uptake systems. The bis-catecholate, azotochelin-like¹⁴⁸ siderophore (Heinisch–Möllmann–Miller (HMM) siderophore, **Table 4.2**)^{58,76–79,149,150} was selected due to its ease of synthesis and its ability to carry large cargo (e.g., daptomycin) into *A. baumannii*, *E. coli*, and *P. aeruginosa*.^{58,59,76–79} Furthermore, β -lactam conjugates with non-cleavable linkers that used tetraacetate derivatives of siderophore **10a** were active against MDR strains capable of efflux.¹⁵¹ We used a modified version of Miller's protocol to access siderophore **10**, which has acid labile ketal protecting groups that can be removed concomitantly with tert-butyl and tert- butoxycarbonyl (Boc) protecting groups on the amino acid side chains.

We developed a modular synthetic route that enables the facile incorporation of a variety of linkers, antibiotics, and siderophores (**Table 4.2**). Gram-scale linker assembly and subsequent siderophore attachment were accomplished on solid-phase to provide the partially protected intermediate **3** in 50% overall yield, and the antibiotic was then coupled to the C-terminus in solution. Following acidolytic deprotection, the final SACs (**7–9**) were obtained in 12–53% yield over two to four steps.

Several aspects of our route merit further discussion. The majority of the synthesis proceeds on solid phase, simplifying purification and facilitating parallel synthesis of analogues. Antibiotics are directly attached in the penultimate step, enabling rapid access to the final antibiotic conjugates from intermediate **3**. The synthesis requires only one HPLC purification,

and the final products are purified by trituration. Daptomycin and solithromycin are commercially available and the oxazolidinones were synthesized following the protocols of Miller⁷⁶ and Rafai Far.¹⁵²

We also synthesized several controls to probe the mechanism of action of **7**, **8**, and **9** using modifications of our existing protocol (**11–18**, **Table 4.2**). These included conjugates with D-amino acid linkers (e.g., **13**, **14**, and **16**), which are not readily cleaved by proteases, enabling us to determine if proteolytic linker cleavage is responsible for the observed activity.¹⁵³ To confirm on-target activity of the antibiotic, we evaluated conjugates that lack an antibiotic or contain an inactive enantiomer of the antibiotic (e.g., **11**, **12**, and **15**). To compare the effectiveness of conjugates containing a peptide linker that did not release acc in periplasmic extract (**Figure 4.2**), we synthesized WSWC conjugate **17**. We also synthesized a siderophore-free conjugate (**18**) to determine the dependence of activity on the siderophore.

4.3.4 Determination of the Antibacterial Activity of SACs 7–9 and Iron-Dependent Activity.

The minimum inhibitory concentrations (MICs) of conjugates **7–9** were evaluated according to the standard CLSI antimicrobial susceptibility testing guidelines in Mueller–Hinton-II (MHII) broth with dipyriddy to sequester iron from the media and promote siderophore-mediated transport (**Table 4.1** and **Table 4.2**).¹⁵⁴ Controls that lacked a siderophore did not show activity dependence on dipyriddy concentration, while the siderophore conjugate became increasingly active at higher concentrations of dipyriddy. This phenomenon can be explained by the enhanced expression of outer membrane transport proteins for siderophore uptake in iron deficient media.¹⁵⁵ The absence of dipyriddy from the growth medium dramatically

attenuated siderophore–conjugate activities without influencing the MIC of the free antibiotic. These results correlate well with expected growth-inhibitory activity of SACs.

We included 15 bacterial strains in our assay (14 Gram negative and one Gram-positive)^{156–161} and have highlighted selected activities below. Two genetically modified strains of *E. coli* were included: a Δ surA strain that is deficient in outer membrane proteins and has increased permeability,¹⁵⁷ and a Δ bamB Δ tolC mutant, which has a deficient BamACDE outer membrane-assembly complex and lacks the TolC-transport protein.^{157,161} This strain is widely used because it is defective in small-molecule efflux.

Solithromycin is active in many Gram-negative and Gram positive species, and the strategy of using a Gram-negative antibiotic is frequently used to evaluate the efficiency of linker cleavage for cleavable SACs.^{57,61–66,80–82,84} The L-linker solithromycin conjugate **9** was comparably active to solithromycin in several pathogenic Gram-negative strains, and the D-linker conjugate **16** was inactive. In *E. coli*, however, conjugates **9** and **16** had similar activity, suggesting that the D-linker conjugate should not be used to evaluate linker cleavage in this species. We found that this may be due to the ability of the entire conjugate to inhibit the 70S *E. coli* ribosome. However, the differences in activity between the D- and the L-solithromycin conjugates in pathogenic strains suggested that the linker may enable the release of Gram-positive antibiotics. With this promising result in-hand, we then proceeded to investigate Gram-positive-only antibiotics (vide infra).

4.3.5 Oxazolidinone Conjugate 8 Was Active against *E. coli* Δ bamB Δ tolC (Table 4.3).

The oxazolidinone class of antibiotics are active against Gram-positive bacteria, but members of this class lack activity against Gram-negative bacteria, due to the presence of

endogenous efflux pumps. Nevertheless, mutants of *E. coli* such as *ΔbamBΔtolC* are susceptible to oxazolidinones because these bacterial strains have disruptions in their efflux systems. This strain is susceptible to eperezolid, but the corresponding amine variant, eperezolid-NH₂ (**5**), was inactive (MIC > 171 μM). This is likely a result of the inability of **5** to diffuse through the outer and inner membranes as indicated by the data in **Table 4.3** (*vide infra*). We therefore asked whether conjugate **8** could deliver **5** into a *ΔbamBΔtolC* mutant of *E. coli*. We were pleased to discover an MIC of 1 μM for **8** in this mutant; the corresponding derivative **14** with an all-D linker showed strongly decreased activity with an MIC of 19 μM, which is consistent with low activities of previously reported oxazolidinone conjugates with non-cleavable linkers.⁸³ In contrast to eperezolid-NH₂ (**5**), eperezolid conjugate **8** displayed only 10% inhibition in a cell-free translation assay at a concentration of 38 μM (**Figure 4.3**), indicating that the intact conjugate does not inhibit the ribosome. These findings suggest that potent inhibition of bacterial growth requires enzymatic cleavage of the linker. Supporting this suggestion, 34% cleavage of **8** to the parent antibiotic eperezolid-NH₂ occurred after 11 h of incubation with bacterial periplasmic extract (**Table 4.3**). Finally, as expected, conjugate **8** was not active in wild-type strains with functional endogenous efflux pumps.

Eperezolid-NH₂ (**5**) has only minimal activity (MIC = 43 μM) against both *E. coli ΔsurA* and *S. aureus Newman*, which lack outer membrane proteins, indicating that the cytoplasmic membrane of both Gram-positive and Gram-negative bacteria provide a barrier for the diffusion of **5** into the cytoplasm. There are two possible explanations for the potent activity of **8** given the lack of activity of **5** in *E. coli ΔbamBΔtolC*: (1) conjugate **8** may be actively transported to the cytoplasm and activated by a cytoplasmic protease^{162,163} or (2) cleavage in the periplasm may

lead to large differences in the concentrations of molecules in the periplasm versus the cytoplasm, enhancing the effective concentration of **5** in the cytoplasm and hence potency.

We also synthesized a number of additional control molecules to probe the antibacterial mechanism of **8**, including conjugate **17** with the WSWC linker (**Table 4.3**); this linker did not release an acc fluorophore from peptide 2 (**Figure 4.2**). Not surprisingly, this analogue had only weak (MIC = 37 μ M) activity, as did compounds **11**, **12**, and **15** that lacked an active antibiotic payload. Similarly, the conjugate **18** without a siderophore was inactive. However, methyl ester **15** retained a modicum of activity (9 μ M), possibly by a mechanism similar to many non-helical proline-containing cationic antimicrobial peptides.¹⁶⁴⁻¹⁶⁶

Miller and co-workers published a highly similar eperezolid conjugate using the same siderophore and eperezolid-NH₂ derivative with a cleavable β -lactam linker.⁷⁶ This conjugate exhibited activity against a number of strains of Gram-negative bacteria, including some with high-level β -lactam resistance. Against strains with high β -lactamase content for which the β -lactam linker did not measurably contribute to activity (up to 50 μ M), the MIC of the conjugates was 6 μ M. We did not observe activity of conjugate **8** in the same *A. baumannii* strain (ATCC BAA-1797), which could be due to inherent differences in the two linkers.

4.3.6 Daptomycin Conjugate 7 Exhibits High Activity against Acinetobacter Species (Table 4.4).

Daptomycin is used to treat Gram-positive infections, but it lacks activity against Gram-negative species. Therefore, we were gratified to find that the cleavable L-linker daptomycin conjugate **7** showed species-specific activity against *A. nosocomialis*, *A. baumannii*, and *E. coli*, with MIC values in the 1 to 10 μ M range, while daptomycin itself was inactive against these

species (MIC > 39 μ M). The highest activities were observed in Acinetobacter species (MIC = 1–5 μ M). Similarly, Miller and co-workers revealed that non-cleavable daptomycin conjugates displayed selective activity against *A. baumannii*.^{58,59} These findings indicate that this approach has the potential to produce precision antibiotics with relatively narrow-spectrum activity. Moreover, as expected, **7** was inactive against *S. aureus* as it was not proteolytically activated due to the absence of a periplasm and periplasmic proteases. The activities of ornithine-functionalized daptomycin analogs in *S. aureus* are highly dependent on the side chain, and the WSPKYM linker reduces the activity of daptomycin in this species.¹⁴⁴ The activity of **7** cannot be compared to previously reported non-cleavable linkers because the specific linker contributes to the activity of non-cleavable daptomycin conjugates.^{58,59} Therefore, we limit our comparisons of the cleavable conjugate **7** to its closely related non-cleavable diastereomer **13**.

The D-linker conjugate **13** was 2- to 11-fold less active than **7** against *E. coli*, *A. baumannii*, and *A. nosocomialis* and did not entirely lose activity as would be expected because daptomycin can still engage its target in the periplasm with a noncleavable linker.^{58,59,76–79} Nevertheless, the L-linker conjugate **7** improved the activity up to 11-fold, suggesting that cleavable linkers may benefit SACs containing periplasmic-targeting antibiotics. Finally, derivatives of **7** lacking the daptomycin payload (**11** and **12**) were essentially inactive. Taken together, the data in **Table 4.4** indicates that we have successfully repurposed daptomycin for Gram-negative bacteria, and the enhanced activity of **7** relative to **13** is consistent with our guiding hypothesis of stereospecific proteolytic activation. It is also clear that proteolytic activation likely occurred in the periplasm, rather than by an extracellular protease in the medium given that daptomycin lacks activity against Gram negative species.

To understand the lower activity observed for *E. coli* (MIC = 11 μ M) relative to *Acinetobacter* species (MIC = 1–5 μ M), we note that the release of daptomycin from conjugate **7** in periplasmic extract of *E. coli* was not observed by HPLC analysis, which may be due to unfavorable steric interactions between the approaching protease(s)¹⁶⁷ and the large daptomycin molecule. Following incubation of **7** in periplasmic extracts of *A. baumannii* and *A. nosocomialis*, however, the HPLC trace revealed cleavage products with retention times that overlapped with daptomycin.

These results are also of interest with respect to the mechanism of action of daptomycin. It has been previously reported that the target for daptomycin (**4**) may be absent in Gram-negative species due to the differing membrane compositions between Gram-positive and Gram-negative bacteria.¹⁶⁸ Given that **7** is active against *E. coli*, it would appear that daptomycin is able to act on the cytoplasmic membranes of these Gram-negative species once they gain access. Also, our finding that daptomycin itself is equipotent against *S. aureus Newman* and in the outer membrane compromised *E. coli Δ surA* (MIC = 0.6 μ M) is consistent with this conclusion.

4.4 Discussion

The strategy developed here should be broadly applicable for discovery of protease-activated peptide prodrugs for a variety of applications. Here, we focused on delivering antibiotics by designing protease-cleavable siderophore conjugates. By targeting *E. coli* periplasmic proteases, we were able to design conjugates that act against a broad (or narrow) spectrum of Gram-negative bacteria, illustrating the potential of this approach. Our results provide strong support for the overall mechanism of proteolytic release of the antibiotic from conjugates **7–9**. Although we have not yet identified the proteases responsible for activity against

our substrates, we purposefully avoided targeting a single protease to decrease the chances of resistance arising from mutants of a single protein. Moreover, the use of chemically stable amide linkers provides an advantage to targeting proteases over esterases and β -lactamases by avoiding the need for esters and β -lactams, which are chemically more labile. Importantly, the modular design and facile synthetic route provides opportunity for rapid synthesis of SACs with different siderophores, linkers, and antibiotics. This has led to the discovery of cleavable conjugates with activity against several clinically relevant Gram-negative pathogens.

Throughout the course of this work, we made a number of unexpected discoveries with impacts that extend beyond the scope of protease-cleavable prodrugs. The L-linker daptomycin conjugate **7** completely lacks the Gram-positive activity of daptomycin and has gained Gram-negative activity, effectively “flipping” the spectrum of activity of this potent antibiotic. We found that conjugates with D-linkers, which are unlikely to be cleaved proteolytically, have moderate activity against several strains of Gram-negative bacteria. Perhaps the most unexpected results are the activities of the solithromycin conjugates **9** and **16** in a cell-free translation assay, which indicate that these large (MW > 2000) conjugates may directly inhibit the ribosome in *E. coli*. These results are extremely surprising in the context of solithromycin–ribosome structural data¹⁶⁹ and may provide the basis for new macrolide–peptide hybrid antibiotics.

Additional studies will be required to optimize the current linkers for use as practical drugs. The current linker has reasonable stability in human serum, which could doubtlessly be enhanced by limited structure–activity relationships. The peptide WSPKYM also contains more than one cleavage site, which may complicate the drug activation mechanism. Our conjugates do not show significant activity against *P. aeruginosa*, a pathogen prone to resistance, which could be due to the following: (1) insufficient linker cleavage may not lead to growth inhibition

because the linker was optimized for *E. coli*, (2) the target for daptomycin may be present in minimal amounts, depending on the strain or species of Gram-negative bacteria,¹⁶⁸ or (3) solithromycin and eperzolid might be efflux substrates in this organism.

In summary, this work provides a robust methodology for selection and screening of Trojan-horse prodrugs applied to the persistent and growing problem of antibacterial resistance. The resulting conjugates from this platform improve upon existing cleavable linkers for SACs. Using phage display, one can rapidly screen vast peptide libraries, and by varying the selection strategy one can screen for linkers with desired characteristics. For example, by using periplasmic extracts from different species of bacteria in succeeding selections, one can ensure broad activity over the desired range of bacteria. Alternatively, negative selection could be incorporated to select against cleavage of serum proteases or beneficial members of the microbiome. Thus, the potential for fine-tuning the protocol for future practical applications is substantial.

4.5 Materials and Methods

MIC, PERIPLASMIC CLEAVAGE ASSAYS, AND CELL-FREE TRANSLATION

Antibiotic Susceptibility Testing by the Broth Microdilution Method.

Strains: *E. coli* DCO was purchased from the Coli Genetic Stock Center (CGSC), and *A. baumannii* ATCC 1797 was purchased from ATCC. The remaining strains were obtained as gifts.

Broth and Agar Preparation

Mueller-Hinton II (MH-II, cation-adjusted) broth was prepared from solid MH-II (22 g) and MilliQ H₂O (1 L), which was autoclaved in a presterilized 1-L glass bottle. MH-II agar plates were prepared from autoclaved MH-II (22 g), Bacto agar (17 g), and MilliQ water (1 L). The

bacterial strains were obtained from glycerol stocks by streaking onto the MH-II agar plates (no antibiotics were introduced into the MH-II agar).

Preparation of sterilized CaCl₂*2H₂O Stock Solutions (only for daptomycin-conjugates)

In the case of daptomycin-containing conjugates, a stock solution of CaCl₂ (50mg/mL) was prepared from CaCl₂*2H₂O (20 mL, 66.2 mg/mL). The solution was filter-sterilized utilizing a Steriflip Vacuum Filtration System with a Millipore Express PLUS Membrane (0.22 μm). In the case of daptomycin conjugates, the CaCl₂*2H₂O solution (100 μL) was added to 48.3-mL aliquots of autoclaved MH-II broth to reach a final concentration of 100 μg/mL CaCl₂ in MH-II. Daptomycin is a calcium-dependent lipopeptide, which requires calcium to permeabilize the cell membrane.

Preparation of sterilized 2,2'-dipyridyl (DP) and PBS stocks

A sterile stock solution of 2,2'- bipyridyl solution (40 mL, 1 mg/mL) was prepared in a 50-mL Falcon tube and then was filter sterilized utilizing a Steriflip Vacuum Filtration System with a Millipore Express PLUS Membrane (0.22 μm). A sterile 1X PBS stock solution [10X PBS (10mL), and MilliQ WATER (90 mL)] was prepared and filter sterilized with an Olympus Plastics 250-mL vacuum-driven filter system with a PES membrane (0.22 μm). A 200 μM DP solution in autoclaved MH-II media was prepared from 1 mg/mL DP (1.56 mL) in MH-II (48.4 mL). A 600 μM DP solution in autoclaved MH-II media was prepared from 1 mg/mL DP (4.68 mL) in MH-II (45.3 mL) were prepared 24 h before use. [Note: Avoided the use of bovine serum albumin (BSA) in the PBS stock solution for siderophore conjugates, which may inhibit catechol-type siderophore mediated iron-transport].

Bacterial Culture Preparation

All autoclaved and sterilized solutions were transferred using sterilized Sarstedt Serological Pipettes (10-mL, 25-mL, and 50-mL), which are attached to an Eppendorf Easypet3. The autoclaved MH-II media contained DP (600 μ M, 200 μ M, 160 μ M, 129 μ M, or without DP). The culture tubes were then placed bottom-side-up in an incubator set at 37°C without shaking for 18-20 h. A sterilized pipet tip was gently touched on the surface of a single colony and added to autoclaved MH-II broth (5 mL) in a sterilized 12-mL culture tube. The cultures were incubated for 18 h at 37 ° C with shaking at 250 rpm. The cultures were diluted 200- fold into autoclaved MH-II broth (4-mL) with 2,2'-dipyridyl (DP) and incubated at 37 o C with shaking at 250 rpm for 3-5 h, or until an optical density at 600 nm (OD600) between 0.2 and 0.6 was achieved. An aliquot of the culture (1 mL) was transferred to a sterilized culture tube and diluted with PBS until an OD600 of 0.13. The cultures (11.5 μ L) were then diluted into MH-II media (15-mL) to a concentration of 1×10^5 cells/mL. The diluted cultures (90 μ L/well) were then added to substrate (10 μ L at the following concentrations: 640 μ g/mL, 320 μ g/mL, 160 μ g/mL, 80 μ g/mL, 40 μ g/mL, 20 μ g/mL, and 10 μ g/mL) in sterilized 96-well plates to achieve a final substrate concentration of 64 μ g/mL, 32 μ g/mL, 16 μ g/mL, 8 μ g/mL, 4 μ g/mL, 2 μ g/mL, and 1 μ g/mL. [note: Polymyxin B was tested at the following final concentrations (μ g/mL): 8, 4, 2, 1, 0.5, 0.25, 0.125.] The 96-well plates were then sealed with sterilized gas-permeable covers. The plates were incubated at 37 ° C with shaking at 225 rpm for 16-20 h. Each well condition was prepared in triplicate. The turbidity of each well was examined and the MIC was counted as the lowest concentration that lacked turbidity. The OD600 was also measured.

Procedure for Isolating Periplasmic Extract

Stock Preparations [20% sucrose/30mM Tris, 50 mM Tris, 50 mM Tris with 0.01% Tween]:

A filter-sterilized, 1-L aqueous solution of 20% sucrose/30mM Tris base was prepared with sucrose (200 g) and Tris base (3.63 g). [Note: EDTA was not used in this procedure to avoid the elimination of metalloproteases from the resulting extract]. A 50-mL aqueous solution of 50 mM Tris base was prepared from solid Tris base (340 mg), along with a separate 50 mM Tris solution containing 0.01% Tween 20 (note: Tween prevents coagulation of proteins).

Osmotic Shock Procedure (without EDTA)

An overnight culture on a MH-II plate (prepared as described above) at 37 ° C for 18 h. Added a single colony to 100 mL of MH-II media and a S75 single colony to 100 mL of LB media in a sterile 2.5-L Erlenmeyer flask. The flask was incubated with shaking until an OD600 of 0.5 was reached (~5-6 hours). Centrifuged the cultures at 4150 rpm for 40 min at 4 ° C or at 15,000 rpm for 10 min at 4 ° C. Poured-off the supernatant into bleach, so as not to disturb the pelleted cells. The filter-sterilized 20% sucrose/30mM Tris base (50 mL) was added to the cell pellets after removal of supernatant using a sterile 50-mL GeneMate serological pipet. The pellets were suspended with the pipet tip and subsequently vortexed to achieve a relatively homogenous suspension and mixed for 10 min at 4 ° C. The suspension was then centrifuged at 4150 rpm for 30 min at 4 ° C or at 15,000 rpm for 10 min at 4 ° C. The supernatant was decanted-off so as not to disturb the pellets. Filter-sterilized cold water (50 mL) was added and vortexed to provide a homogeneous suspension, which was allowed to shake for 10 minutes at 4 ° C. The suspension was then centrifuged at 4150 rpm for 30 min at 4 ° C or at 15,000 rpm for 10 min at 4 ° C. The supernatant (periplasmic extract) was filtered through a 500-mL vacuum filter (PES: 0.22 µm), ensuring that the filtrate remained at 4 ° C by keeping the plastic filtration container on ice. The filtrate was then concentrated in an Amicon Ultra-15 Centrifugal Filter Ultracel -10K (15-mL) by centrifuging at 3600 rpm for 15 min at 4 ° C. The process was repeated until the periplasmic

extract reached a volume of 0.5-2 mL and a total protein concentration <2.5 mg/mL. A nanodrop was used to determine the protein concentrations. Depending on the concentration, the periplasmic extract may be diluted with aqueous Tris solution (pH=8). The periplasmic extract were then aliquoted (200 µL/Eppendorf tube) into 1.5-mL Eppendorf tubes and flash-frozen with liquid nitrogen. [Note: To avoid reduction in protease activity, glycerol was not added to the periplasmic extract prior to freezing. All experiments were conducted with a fresh 200 µL aliquot of periplasmic extract to avoid inconsistencies after multiple freeze-thaw cycles. Before use, the periplasmic extract was thawed slowly at 4°C.]

Total Protein/Periplasmic Extract (Evaluated concentration at OD 280 nm using Nanodrop™)

E. coli K12 MG1655 (from LB media): 1.557 mg/mL; subsequent preparation: 745 µg/mL

E. coli K12 MG1655 (from MH-II media): 1.979 mg/mL

A. nosocomialis M2 (from LB media): 548 µg/mL

A. nosocomialis M2 (from MH-II media): 545 µg/mL

A. baumannii ATCC BAA-1797 (from LB media): 1.006 mg/mL

A. baumannii ATCC BAA-1797 (from MH-II media): 565 µg/mL

S76 E. coli DCO (from LB media): 1.581 mg/mL

E. coli DCO (from MH-II media): 1.906 mg/mL

E. coli BW25113 ΔbamBΔtolC (from LB media): 924 µg/mL (batch 1); 1.962 µg/mL (batch 2)

E. coli BW25113 ΔbamBΔtolC (from MH-II media): 919 µg/mL

P. aeruginosa PA01 (from LB media): 2.401 mg/mL

P. aeruginosa PA01 (from MH-II media): 1.769 mg/mL

P. aeruginosa ATCC10145 (from LB media): 2.002 mg/mL

P. aeruginosa ATCC10145 (from MH-II media): 1.447 mg/mL

S. enterica 14028s (from LB media): 939 µg/mL

S. enterica 14028s (from MH-II media): 1.257 µg/mL

E. cloacae ATCC 13047 (from LB media): 917 µg/mL

E. cloacae ATCC 13047 (from MH-II media): 1.549 mg/mL

E. aerogenes ATCC 13048 (from LB media): 2.471 µg/mL

E. aerogenes ATCC 13048 (from MH-II media): 1.456 µg/mL

K. pneumoniae MGH78578 (from LB media): low protein yield <50 µg/mL

K. pneumoniae MGH78578 (from MH-II media): low protein yield <50 µg/mL

ACC Cleavage in Periplasmic Extract

Spectroscopic Evaluation of Scarless Linkers. [Note: The assay and all stock solutions were prepared at 4 ° C.] Solutions for substrates 1 and 2 (50 µM) were prepared in Tris (without Tween 20) from 2 mg/mL stock solutions in DMSO. Each 50 µM solution of 1 and 2 (25 µL) was then transferred to a 96-well plate (opaque, 200 µL/well volume) in triplicate over two rows. As a control, each substrate was mixed in triplicate with 50 mM Tris (25 µL, note: 0.01% Tween 20 was contained in Tris) without periplasmic extract. After slow thawing of *E. coli* K12 MG1655 (1.557 mg/mL, 100 µL) and *E. coli* ΔbamBΔtolC BW25113 (1.962 mg/mL, 100 µL) periplasmic extracts over 30 min on ice, they were diluted in Tris (94.6 µL and 145.3 µL, respectively, note: 0.01% Tween 20 was contained in Tris) to provide 800 µg/mL stock solutions of each extract. The 800 µg/mL solutions of periplasmic extract (25 µL) were then transferred to the 96-well plate (opaque, 200 µL/well volume) containing 1 and 2 resulting in a maximum volume of 50 µL/well. The final concentrations of periplasmic extract and substrate were 400 µg/mL and 25 µM, respectively. The plate was sealed with a transparent polyolefin silicone film

(ThermoFisher™ Nuc™ Sealing Tape, 12-565-513) and placed in a plate reader set to 37 ° C with shaking at 225 rpm for 8 h. ACC excitation wavelengths: 300-410 nm at 5 nm intervals. ACC excitation maximum: 355 nm. ACC emission wavelengths: 410-500 nm at 5 nm intervals. ACC Emission maximum is 460 nm. The data is plotted in **Figure 4.2**. Protease inhibitors were pre-incubated with periplasmic extract for 5-10 min at r.t. HPLC traces of peptide 1 at 326 nm (at time t=0 and t=8h) suggests ~100% linker cleavage over the time course of the reaction.

Cleavage of Eperezolid-NH₂ Conjugate (5) and Daptomycin Conjugate (4) in Periplasmic Extract.

The periplasmic extract [25 µL, 400 µg/mL total protein for E. coli K12 MG1655 and A. nosocomialis; see total protein list above in section B for other strains] was mixed with the daptomycin conjugate 7 (25 µL, 117.6 µM) or the eperezolid conjugate 8 (25 µL, 117.6 µM) in a 1.5-mL Eppendorf tube. The reaction mixture was mixed at 1050 rpm in a table-top incubator set at 37 ° C for 11 h. After 11 h, 25 µL was removed and placed in a 400-µL glass insert fitted in a mass-spec vial, which was followed by the addition of MilliQ H₂O (25 µL) and 1 M HCl (2 µL). The reaction mixture was analyzed by HPLC (54 minutes, 0 to 95% CH₃CN/H₂O with 0.1 % TFA, 254 nm). Evidence for unmodified daptomycin release is denoted by peaks that overlap with daptomycin (e.g. A. nosocomialis and A. baumannii). Due to limitations in the mass spec detector, we were unable to assign a mass to peaks overlapping with daptomycin. For cases where daptomycin release was not apparent or insignificant (e.g. E. coli).

In Vitro Translation

The ability of conjugates to inhibit the 70S E. coli ribosome was tested in vitro using the PURExpress, In-Vitro Protein Synthesis Kit (NEB), murine RNase inhibitor (NEB), and 7.5 ng/µl of template DNA encoding the fluorescent protein mEGFP. The volumes of each

component in the reaction mixture were scaled down from the NEB protocol for a final reaction volume of 4 μ L. S78 Analogs were screened at a concentration of 10 μ M (conjugate 8 and eperzolid-NH₂ (5) at 38 μ M), with a final concentration of 1.9% DMSO. All reactions were performed in triplicate. Translation reactions were carried out at 37 °C for 1 hour. To assist in the transfer of reactions to 96-well half-area NBS microplates (Corning 3993) for final measurements, the volume was increased to 50 μ L by adding buffer C (20 mM Tris-HCl pH 7.5, 60 mM NH₄Cl, 6 mM MgCl₂, 0.5 mM EDTA). mEGFP was excited at 485 nm; its emission was recorded at 535 nm. For comparison of analog activities across multiple initial screens, fluorescence readouts were normalized to the blank (containing 1.9% DMSO).

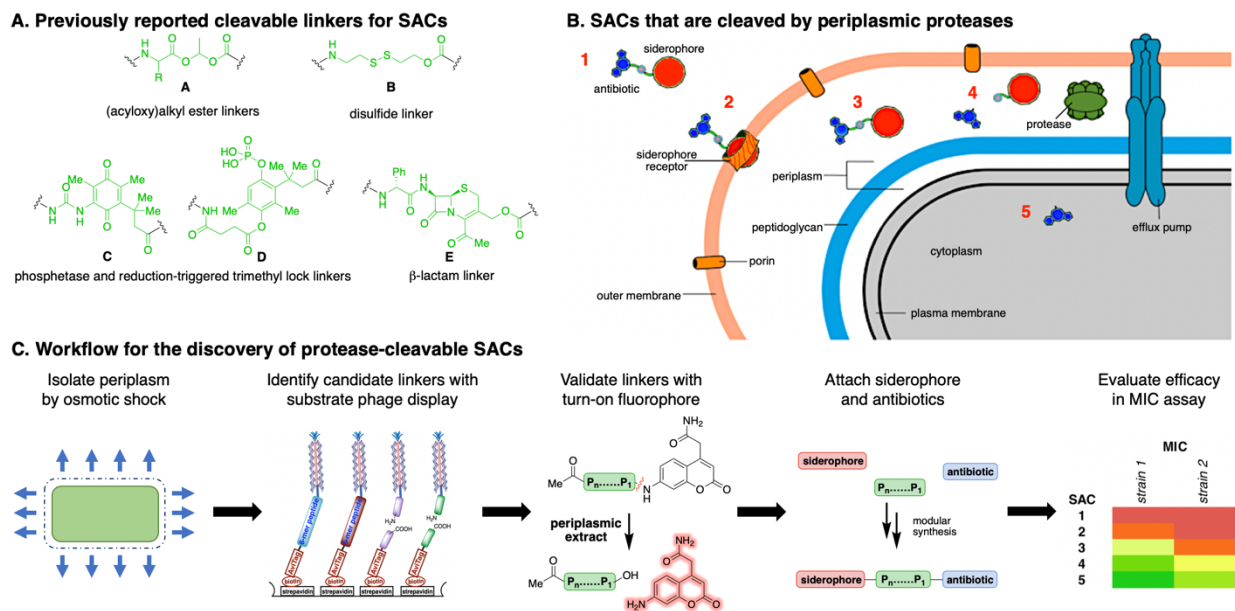


Figure 4.1 | Platform to discover protease activated antibiotics.

(A) Selected cleavable linkers that have previously been used for SACs. (B) Concept for SACs that contain a linker that can be cleaved by periplasmic proteases. (C) Workflow for the development of protease-cleavable SACs.

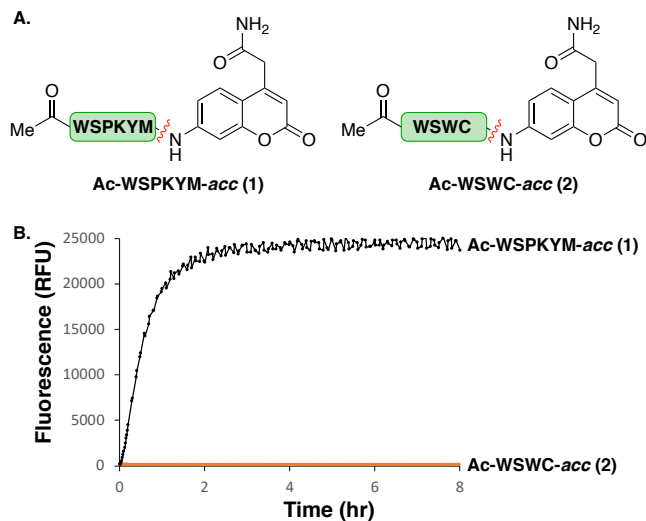


Figure 4.2 | Protease cleavage of acc peptide in periplasmic extract.

(A) Peptides with turn-on fluorophore, *acc*, as an antibiotic surrogate. (B) Evaluation of *acc* cleavage from peptides 1 and 2 in a periplasmic extract of *E. coli* K12 MG1655 (400 μ g/mL) at 37 $^{\circ}$ C.

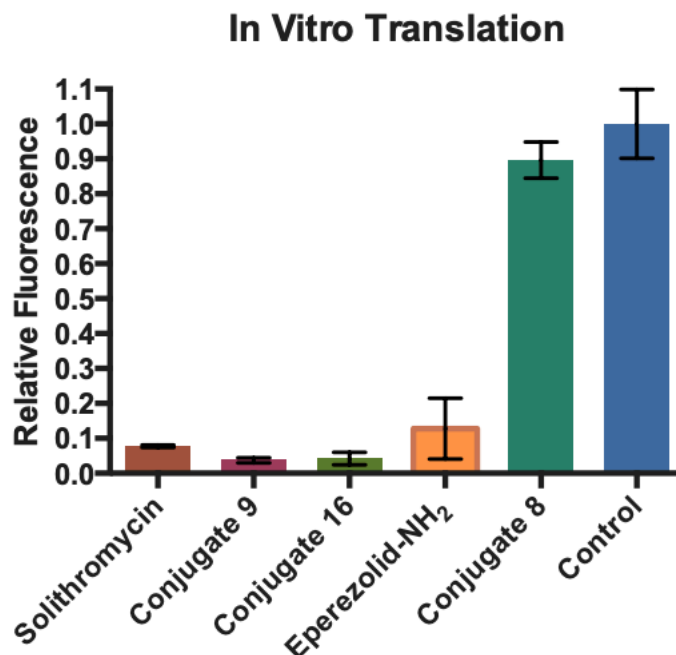


Figure 4.3 | Comparison of inhibition of bacterial translation by several conjugates.

In vitro translation shows the ability of conjugates 8 (38 μ M), 9 (10 μ M), and 16 (10 μ M) to inhibit the 70S *E. coli* ribosome relative to the parent antibiotics eperezolid-NH₂ (5,38 μ M) and solithromycin (6,10 μ M).

Table 4.1 | Highly Enriched Sequences Found through Substrate Phage Display.

Sequence	Reads	Initial reads	Enrichment Factor
KNQSLG	10652	0.5	21304
GSDSSV	9239	0.5	18478
NHADVH	8138	0.5	16276
KSEMLS	7742	0.5	15484
WCKWAS	15307	1	15307
PKYMRF	13192	1	13192

Table 4.2 | Modular Synthetic Platform for SAC Synthesis.

siderophore

 HMM Siderophore
 10 R¹, R² = Ph
 10a R¹, R² = -H

antibiotic

 daptomycin (4) eperezolid-NH₂ (5) solithromycin (6)

Compound Number	Designation	N-terminal Substitution	linker	C-terminal Substitution
1	Ac-WSPKYM- <i>acc</i>	Acetyl	WSPKYM	<i>acc</i>
2	Ac-WSWC- <i>acc</i>	Acetyl	WSWC	<i>acc</i>
7	L-Linker Daptomycin Conjugate	HMM Siderophore	WSPKYM	daptomycin (4)
8	L-Linker Eperezolid-NH ₂ Conjugate	HMM Siderophore	WSPKYM	eperezolid-NH ₂ (5)
9	L-Linker Solithromycin Conjugate	HMM Siderophore	WSPKYM	solithromycin (6)
11	Conjugate Without Antibiotic, Acid	HMM Siderophore	WSPKYM	free acid (-OH)
12	Conjugate Without Antibiotic, Ester	HMM Siderophore	WSPKYM	methyl ester (-OMe)
13	D-Linker Daptomycin Conjugate	HMM Siderophore	wspkym (D-linker)	daptomycin (4)
14	D-Linker Eperezolid-NH ₂ Conjugate	HMM Siderophore	wspkym (D-linker)	eperezolid-NH ₂ (5)
15	Conjugate With Inactive Enantiomer	HMM Siderophore	WSPKYM	<i>ent</i> -eperezolid-NH ₂
16	D-Linker Solithromycin Conjugate	HMM Siderophore	wspkym (D-linker)	solithromycin (6)
17	Conjugate With WSWC Linker	HMM Siderophore	WSWC	eperezolid-NH ₂ (5)
18	Conjugate Without Siderophore	Acetyl	WSPKYM	eperezolid-NH ₂ (5)

Table 4.3 | Antibacterial Activity (MIC in μM) and In Vitro Cleavage of Eperezolid-NH₂ Conjugate 8 and Derivatives Thereof.

Eperezolid Conjugates and Controls	<i>E. coli</i> $\Delta\text{bamB}\Delta\text{tolC}$ efflux knockout	<i>E. coli</i> ΔsurA outer-membrane knockout	<i>S. aureus</i> Newman Gram-positive
Eperezolid-NH ₂ (5)	>171	43	43
L-Linker Eperezolid-NH ₂ Conjugate (8)	1	38	>38
D-Linker Eperezolid-NH ₂ Conjugate (14)	19	>38	>38
Conjugate Without Antibiotic, Acid (11)	48	>48	>48
Conjugate Without Antibiotic, Ester (12)	24	48	>48
Conjugate With Inactive Enantiomer (15)	9	38	>38
Conjugate With WSWC Linker (17)	37	ND	ND
Conjugate Without Siderophore (18)	>77	ND	>77
% Eperezolid Release From 8 In Extract	34 \pm 1.5	ND	ND

Table 4.4 | Antibacterial Activity (MIC in μM) of Daptomycin SAC 7 and Derivatives Thereof.

Daptomycin Conjugates and Controls	<i>E. coli</i> K12 wild type	<i>E. coli</i> $\Delta\text{bamB}\Delta\text{tolC}$ efflux knockout	<i>A. baumannii</i> multidrug resistant	<i>A. nosocomialis</i> pathogenic	<i>E. coli</i> ΔsurA outer-membrane knockout	<i>S. aureus</i> Newman Gram-positive
Daptomycin (4)	>39	>39	>39	>39	0.6	0.6
L-Linker Daptomycin Conjugate (7)	11	11	5	1	>21	>21
D-Linker Daptomycin Conjugate (13)	>23	23	23	11	23	>23
Conjugate Without Antibiotic, Acid (11)	>48	48	>24	>48	>48	>48
Conjugate Without Antibiotic, Ester (12)	>48	24	>24	ND	48	>48

4.6 References

1. Cheng, C.-T., Kuo, C.-Y. & Ann, D. K. KAPtain in charge of multiple missions: Emerging roles of KAP1. *World J. Biol. Chem.* **5**, 308–320 (2014).
2. Anjana Sharma, S. P. G. Fundamentals of Viruses and Their Proteases. *Viral Proteases and Their Inhibitors 1* (2017).
3. Pasquereau, S., Kumar, A., Abbas, W. & Herbein, G. Counteracting Akt Activation by HIV Protease Inhibitors in Monocytes/Macrophages. *Viruses* **10**, (2018).
4. Wang, Q. *et al.* CARD8 is an inflammasome sensor for HIV-1 protease activity. *Science* **371**, (2021).
5. Pablos, I. *et al.* Mechanistic insights into COVID-19 by global analysis of the SARS-CoV-2 3CLpro substrate degradome. *Cell Rep.* **37**, 109892 (2021).
6. Jäger, S. *et al.* Global landscape of HIV–human protein complexes. *Nature* **481**, 365–370 (2012).
7. Zhang, G., Fenyő, D. & Neubert, T. A. Evaluation of the variation in sample preparation for comparative proteomics using stable isotope labeling by amino acids in cell culture. *J. Proteome Res.* **8**, 1285–1292 (2009).
8. Miyamoto, A. *et al.* Subcellular localization of the RNA-binding protein PTBP1 is regulated by post-translational modifications in the RRM2 domain. *FASEB J.* **34**, 1–1 (2020).
9. Han, A. *et al.* De novo prediction of PTBP1 binding and splicing targets reveals unexpected features of its RNA recognition and function. *PLoS Comput. Biol.* **10**, e1003442 (2014).

10. Kosinski, P. A., Laughlin, J., Singh, K. & Covey, L. R. A complex containing polypyrimidine tract-binding protein is involved in regulating the stability of CD40 ligand (CD154) mRNA. *J. Immunol.* **170**, 979–988 (2003).
11. Vavassori, S., Shi, Y., Chen, C.-C., Ron, Y. & Covey, L. R. In vivo post-transcriptional regulation of CD154 in mouse CD4⁺ T cells. *Eur. J. Immunol.* **39**, 2224–2232 (2009).
12. Geng, G. *et al.* PTBP1 is necessary for dendritic cells to regulate T-cell homeostasis and antitumour immunity. *Immunology* **163**, 74–85 (2021).
13. Monzón-Casanova, E. *et al.* The RNA-binding protein PTBP1 is necessary for B cell selection in germinal centers. *Nat. Immunol.* **19**, 267–278 (2018).
14. Florez, P. M., Sessions, O. M., Wagner, E. J., Gromeier, M. & Garcia-Blanco, M. A. The polypyrimidine tract binding protein is required for efficient picornavirus gene expression and propagation. *J. Virol.* **79**, 6172–6179 (2005).
15. Allouch, A. *et al.* The TRIM family protein KAP1 inhibits HIV-1 integration. *Cell Host Microbe* **9**, 484–495 (2011).
16. Van den Bergh, R. *et al.* Transcriptome analysis of monocyte-HIV interactions. *Retrovirology* **7**, 53 (2010).
17. Ait-Ammar, A. *et al.* Inhibition of HIV-1 gene transcription by KAP1 in myeloid lineage. *Sci. Rep.* **11**, 2692 (2021).
18. Robbez-Masson, L. *et al.* The HUSH complex cooperates with TRIM28 to repress young retrotransposons and new genes. *Genome Res.* **28**, 836–845 (2018).
19. Chougui, G. & Margottin-Goguet, F. HUSH, a Link Between Intrinsic Immunity and HIV Latency. *Front. Microbiol.* **10**, 224 (2019).

20. Taura, M., Song, E., Ho, Y.-C. & Iwasaki, A. Apobec3A maintains HIV-1 latency through recruitment of epigenetic silencing machinery to the long terminal repeat. *Proc. Natl. Acad. Sci. U. S. A.* **116**, 2282–2289 (2019).
21. Price, A. J. *et al.* CPSF6 defines a conserved capsid interface that modulates HIV-1 replication. *PLoS Pathog.* **8**, e1002896 (2012).
22. Burdick, R. C. *et al.* HIV-1 uncoats in the nucleus near sites of integration. *Proc. Natl. Acad. Sci. U. S. A.* **117**, 5486–5493 (2020).
23. Selyutina, A., Persaud, M., Lee, K., KewalRamani, V. & Diaz-Griffero, F. Nuclear Import of the HIV-1 Core Precedes Reverse Transcription and Uncoating. *Cell Rep.* **32**, 108201 (2020).
24. Achuthan, V., Perreira, J. M., Ahn, J. J., Brass, A. L. & Engelman, A. N. Capsid-CPSF6 interaction: Master regulator of nuclear HIV-1 positioning and integration. *J. Life Sci.* **1**, 39–45 (2019).
25. Jacques, D. A. *et al.* HIV-1 uses dynamic capsid pores to import nucleotides and fuel encapsidated DNA synthesis. *Nature* **536**, 349–353 (2016).
26. Bonczkowski, P. *et al.* Protein expression from unintegrated HIV-1 DNA introduces bias in primary in vitro post-integration latency models. *Sci. Rep.* **6**, 38329 (2016).
27. Randolph, K., Hyder, U. & D’Orso, I. KAP1/TRIM28: Transcriptional Activator and/or Repressor of Viral and Cellular Programs? *Front. Cell. Infect. Microbiol.* **12**, (2022).
28. Bacon, C. W. *et al.* KAP1 Is a Chromatin Reader that Couples Steps of RNA Polymerase II Transcription to Sustain Oncogenic Programs. *Mol. Cell* **78**, 1133-1151.e14 (2020).

29. Hiragami-Hamada, K. *et al.* Dynamic and flexible H3K9me3 bridging via HP1 β dimerization establishes a plastic state of condensed chromatin. *Nat. Commun.* **7**, 11310 (2016).
30. Impens, F. *et al.* A catalogue of putative HIV-1 protease host cell substrates. *Biol. Chem.* **393**, 915–931 (2012).
31. Crawford, E. D. *et al.* The DegraBase: a database of proteolysis in healthy and apoptotic human cells. *Mol. Cell. Proteomics* **12**, 813–824 (2013).
32. Kumar, A. *et al.* Limited HIV-1 Reactivation in Resting CD4⁺ T cells from Aviremic Patients under Protease Inhibitors. *Sci. Rep.* **6**, 38313 (2016).
33. Hultquist, J. F. *et al.* A Cas9 Ribonucleoprotein Platform for Functional Genetic Studies of HIV-Host Interactions in Primary Human T Cells. *Cell Rep.* **17**, 1438–1452 (2016).
34. chip suspension protocol.pdf.
35. Kit, M. C. I. ChIP-IT Express Enzymatic.
36. NucleoSpin%20Gel%20and%20PCR%20Clean-up%20User%20Manual_Rev_04.pdf.
37. Tsang, M., Gantchev, J., Ghazawi, F. M. & Litvinov, I. V. Protocol for adhesion and immunostaining of lymphocytes and other non-adherent cells in culture. *Biotechniques* **63**, 230–233 (2017).
38. Llaca-Díaz, J. M., Mendoza-Olazarán, S., Camacho-Ortiz, A., Flores, S. & Garza-González, E. One-year surveillance of ESKAPE pathogens in an intensive care unit of Monterrey, Mexico. *Chemotherapy* **58**, 475 (2012).
39. Pendleton, J. N., Gorman, S. P. & Gilmore, B. F. Clinical relevance of the ESKAPE pathogens. *Expert Rev. Anti. Infect. Ther.* **11**, 297 (2013).

40. Breijyeh, Z., Jubeh, B. & Karaman, R. Resistance of Gram-Negative Bacteria to Current Antibacterial Agents and Approaches to Resolve It. *Molecules* **25**, 1340 (2020).
41. Li, X. Z., Plésiat, P. & Nikaido, H. The challenge of efflux-mediated antibiotic resistance in Gram-negative bacteria. *Clin. Microbiol. Rev.* **28**, 337 (2015).
42. Galdiero, S. *et al.* Microbe-host interactions: structure and role of Gram-negative bacterial porins. *Curr. Protein Pept. Sci.* **13**, 843 (2012).
43. Nikaido, H. Molecular basis of bacterial outer membrane permeability revisited. *Microbiol. Mol. Biol. Rev.* **67**, 593 (2003).
44. Choi, U. & Lee, C. R. Distinct Roles of Outer Membrane Porins in Antibiotic Resistance and Membrane Integrity in *Escherichia coli*. *Front. Microbiol.* **10**, 953 (2019).
45. Braun, V. & Braun, M. Active transport of iron and siderophore antibiotics. *Curr. Opin. Microbiol.* **5**, 194 (2002).
46. Livermore, D. M. Antibiotic uptake and transport by bacteria. *Scand. J. Infect. Dis. Suppl.* **74**, 15 (1990).
47. Perlman, D. The roles of the Journal of Antibiotics in determining the future of antibiotic research. *Jpn. J. Antibiot.* **30**, S201 (1977).
48. Diarra, M. S. *et al.* Species selectivity of new siderophore-drug conjugates that use specific iron uptake for entry into bacteria. *Antimicrob. Agents Chemother.* **40**, 2610 (1996).
49. Ji, C., Juárez-Hernández, R. E. & Miller, M. J. Exploiting bacterial iron acquisition: siderophore conjugates. *Future Med. Chem.* **4**, 297–313 (2012).
50. Page, M. G. Siderophore conjugates. *Ann. N. Y. Acad. Sci.* **1277**, 115 (2013).
51. Tillotson, G. S. Trojan Horse Antibiotics-A Novel Way to Circumvent Gram-Negative Bacterial Resistance? *Infect. Dis.: Res. Treat.* **9**, 45 (2016).

52. Zheng, T. & Nolan, E. M. Enterobactin-mediated delivery of β -lactam antibiotics enhances antibacterial activity against pathogenic *Escherichia coli*. *J. Am. Chem. Soc.* **136**, 9677 (2014).
53. Watanabe, N. A., Nagasu, T., Katsu, K. & Kitoh, K. E-0702, a new cephalosporin, is incorporated into *Escherichia coli* cells via the tonB-dependent iron transport system. *Antimicrob. Agents Chemother.* **31**, 497 (1987).
54. Curtis, N. A. *et al.* Iron-regulated outer membrane proteins of *Escherichia coli* K-12 and mechanism of action of catechol-substituted cephalosporins. *Antimicrob. Agents Chemother.* **32**, 1879 (1988).
55. Silley, P., Griffiths, J. W., Monsey, D. & Harris, A. M. Mode of action of GR69153, a novel catechol-substituted cephalosporin, and its interaction with the tonB-dependent iron transport system. *Antimicrob. Agents Chemother.* **34**, 1806 (1990).
56. Hashizume, T., Sanada, M., Nakagawa, S. & Tanaka, N. Comparison of transport pathways of catechol-substituted cephalosporins, BO-1236 and BO-1341, through the outer membrane of *Escherichia coli*. *J. Antibiot.* **43**, 1617 (1990).
57. Nikaido, H. & Rosenberg, E. Y. Cir and Fiu proteins in the outer membrane of *Escherichia coli* catalyze transport of monomeric catechols: study with beta-lactam antibiotics containing catechol and analogous groups. *J. Bacteriol.* **172**, 1361 (1990).
58. McKee, J. A., Sharma, S. K. & Miller, M. J. Iron transport mediated drug delivery systems: synthesis and antibacterial activity of spermidine- and lysine-based siderophore-beta-lactam conjugates. *Bioconjug. Chem.* **2**, 281 (1991).
59. Dolence, E. K., Minnick, A. A., Lin, C. E., Miller, M. J. & Payne, S. M. Synthesis and siderophore and antibacterial activity of N5-acetyl-N5-hydroxy-L-ornithine-derived

- siderophore-beta-lactam conjugates: iron-transport-mediated drug delivery. *J. Med. Chem.* **34**, 968 (1991).
60. Ji, C., Miller, P. A. & Miller, M. J. Iron transport-mediated drug delivery: practical syntheses and in vitro antibacterial studies of tris-catecholate siderophore-aminopenicillin conjugates reveals selectively potent antipseudomonal activity. *J. Am. Chem. Soc.* **134**, 9898 (2012).
61. Kohira, N. *et al.* In Vitro Antimicrobial Activity of a Siderophore Cephalosporin, S-649266, against Enterobacteriaceae Clinical Isolates, Including Carbapenem-Resistant Strains. *Antimicrob. Agents Chemother.* **60**, 729 (2016).
62. Miethke, M. & Marahiel, M. A. Siderophore-based iron acquisition and pathogen control. *Microbiol. Mol. Biol. Rev.* **71**, 413 (2007).
63. Hider, R. C. & Kong, X. Chemistry and biology of siderophores. *Nat. Prod. Rep.* **27**, 637 (2010).
64. Chu, B. C. *et al.* Siderophore uptake in bacteria and the battle for iron with the host; a bird's eye view. *Biometals* **23**, 601 (2010).
65. Ribeiro, M. & Simões, M. Siderophores: A Novel Approach to Fight Antimicrobial Resistance. in *Pharmaceuticals from Microbes: Impact on Drug Discovery* (eds. Arora, D., Sharma, C., Jaglan, S. & Lichtfouse, E.) 99–120 (Springer International Publishing, 2019).
66. Ma, L., Terwilliger, A. & Maresso, A. W. Iron and zinc exploitation during bacterial pathogenesis. *Metallomics* **7**, 1541–1554 (2015).
67. Messenger, A. J. M. & Barclay, R. Bacteria, Iron and Pathogenicity. *Biochem. Educ.* **11**, 54 (1983).

68. Noinaj, N., Guillier, M., Barnard, T. J. & Buchanan, S. K. TonB-dependent transporters: regulation, structure, and function. *Annu. Rev. Microbiol.* **64**, 43 (2010).
69. Wencewicz, T. A. & Miller, M. J. Sideromycins as Pathogen-Targeted Antibiotics. in *Antibacterials: Volume II* (eds. Fisher, J. F., Mobashery, S. & Miller, M. J.) 151–183 (Springer International Publishing, 2018).
70. Page, M. G. P. The Role of Iron and Siderophores in Infection, and the Development of Siderophore Antibiotics. *Clin. Infect. Dis.* **69**, S529 (2019).
71. Schalk, I. J. Siderophore–antibiotic conjugates: exploiting iron uptake to deliver drugs into bacteria. *Clin. Microbiol. Infect.* **24**, 801 (2018).
72. Schalk, I. J. & Guillon, L. Fate of ferrisiderophores after import across bacterial outer membranes: different iron release strategies are observed in the cytoplasm or periplasm depending on the siderophore pathways. *Amino Acids* **44**, 1267 (2013).
73. Schalk, I. J., Mislin, G. L. & Brillet, K. Structure, function and binding selectivity and stereoselectivity of siderophore-iron outer membrane transporters. *Curr. Top. Membr.* **69**, 37 (2012).
74. Faraldo-Gómez, J. D. & Sansom, M. S. P. Acquisition of siderophores in gram-negative bacteria. *Nat. Rev. Mol. Cell Biol.* **4**, 105 (2003).
75. Tonziello, G., Caraffa, E., Pinchera, B., Granata, G. & Petrosillo, N. Present and future of siderophore–based therapeutic and diagnostic approaches in infectious diseases. *Infect. Dis. Rep.* **11**, 8208 (2019).
76. Wilson, B. R., Bogdan, A. R., Miyazawa, M., Hashimoto, K. & Tsuji, Y. Siderophores in Iron Metabolism: From Mechanism to Therapy Potential. *Trends Mol. Med.* **22**, 1077 (2016).

77. Holden, V. I. & Bachman, M. A. Diverging roles of bacterial siderophores during infection. *Metallomics* **7**, 986 (2015).
78. Braun, V., Pramanik, A., Gwinner, T., Köberle, M. & Bohn, E. Sideromycins: tools and antibiotics. *Biometals* **22**, 3 (2009).
79. Pramanik, A. *et al.* Albomycin is an effective antibiotic, as exemplified with *Yersinia enterocolitica* and *Streptococcus pneumoniae*. *Int. J. Med. Microbiol.* **297**, 459 (2007).
80. Stefanska, A. L., Fulston, M., Houge-Frydrych, C. S. V., Jones, J. J. & Warr, S. R. A potent seryl tRNA synthetase inhibitor SB-217452 isolated from a *Streptomyces* species. *J. Antibiot.* **53**, 1346 (2000).
81. Gause, G. F. Recent studies on albomycin, a new antibiotic. *Br. J. Med.* **2**, 1177 (1955).
82. Kaliuzhnaia-Lukashova, G. M. Clinical study of albomycin, colimycin and terramycin. *Klin. Med.* **36**, 30 (1958).
83. Georgievskaja, V. S. Clinical observations on the use of albomycin in purulent mastitis. *Sov. Med.* **22**, 82 (1958).
84. Danovoi, I. D. Use of albomycin in an obstetrical–gynecological clinic. *Akush. Ginekol.* **33**, 37 (1957).
85. Uglova, V. M. Comparative evaluation of the use of albomycin and furacillin in the treatment of infected wounds; experimental study. *Vestn. Khir. Im. I I Grek.* **77**, 73 (1956).
86. Sigal, A. E. Application of albomycin in the treatment of pulmonary suppurations. *Klin. Med.* **33**, 24 (1955).
87. Berent, I. E. & Gil'man, K. Z. Experience in application of the new domestic antibiotic albomycin in dermatovenerology. *Sov. Med.* **18**, 34 (1954).

88. Raikher, E. A. & El'man, E. F. Application of albomycin in pneumonia in infants during their first months of life. *Sov. Med.* **16**, 18 (1952).
89. Gamburg, R. L. Use of albomycin in pneumonia in children. *Pediatriia* **5**, 37 (1951).
90. Antibiotic albomycin in the treatment of pneumonias and toxemias in infants during the first year of life. *Fel'dsher i akusherka* **12**, 38 (1951).
91. Krechmer, B. B., Val'ter, E. M. & Baiandina, S. A. Application of albomycin in pneumonia in infants. *Sov. Med.* **10**, 10 (1951).
92. Lin, Z. *et al.* Total synthesis and antimicrobial evaluation of natural albomycins against clinical pathogens. *Nat. Commun.* **9**, 3445 (2018).
93. Merdanovic, M., Clausen, T., Kaiser, M., Huber, R. & Ehrmann, M. Protein quality control in the bacterial periplasm. *Annu. Rev. Microbiol.* **65**, 149 (2011).
94. Negash, K. H., Norris, J. K. S. & Hodgkinson, J. T. Siderophore – Antibiotic conjugate design: New drugs for bad bugs? *Molecules* **24**, 3314 (2019).
95. Ghosh, M. *et al.* Siderophore conjugates of daptomycin are potent inhibitors of carbapenem resistant strains of *Acinetobacter baumannii*. *ACS Infect. Dis.* **4**, 1529 (2018).
96. Ghosh, M. *et al.* Targeted antibiotic delivery: selective siderophore conjugation with daptomycin confers potent activity against multidrug resistant *Acinetobacter baumannii* both in vitro and in vivo. *J. Med. Chem.* **60**, 4577 (2017).
97. Office of the Commissioner. FDA approves new antibacterial drug to treat complicated urinary tract infections as part of ongoing efforts to address antimicrobial resistance. <https://www.fda.gov/news-events/press-announcements/fda-approves-new-antibacterial-drug-treat-complicated-urinary-tract-infections-part-ongoing-efforts> (2019).

98. Hennard, C. *et al.* Synthesis and Activities of Pyoverdin-Quinolone Adducts: A Prospective Approach to a Specific Therapy Against *Pseudomonas aeruginosa*. *J. Med. Chem.* **44**, 2139 (2001).
99. Rivault, F. *et al.* Synthesis of pyochelin–norfloxacin conjugates. *Bioorg. Med. Chem. Lett.* **17**, 640 (2007).
100. Noël, S. *et al.* Synthesis and biological properties of conjugates between fluoroquinolones and a N3"-functionalized pyochelin. *Org. Biomol. Chem.* **9**, 8288 (2011).
101. Ji, C. & Miller, M. J. Siderophore-fluoroquinolone conjugates containing potential reduction-triggered linkers for drug release: synthesis and antibacterial activity. *Biometals* **28**, 541 (2015).
102. Fardeau, S. *et al.* Synthesis and antibacterial activity of catecholate–ciprofloxacin conjugates. *Bioorg. Med. Chem.* **22**, 4049 (2014).
103. Ji, C. & Miller, M. J. Chemical syntheses and in vitro antibacterial activity of two desferrioxamine B-ciprofloxacin conjugates with potential esterase and phosphatase triggered drug release linkers. *Bioorg. Med. Chem.* **20**, 3828 (2012).
104. Wencewicz, T. A., Möllmann, U., Long, T. E. & Miller, M. J. Is drug release necessary for antimicrobial activity of siderophore-drug conjugates? Syntheses and biological studies of the naturally occurring salmycin “Trojan Horse” antibiotics and synthetic desferridanoxamine-antibiotic conjugates. *Biometals* **22**, 633 (2009).
105. Md-Saleh, S. R. *et al.* Synthesis of citrate–ciprofloxacin conjugates. *Bioorg. Med. Chem. Lett.* **19**, 1496 (2009).

106. Juarez-Hernandez, R. E., Miller, P. A. & Miller, M. J. Syntheses of Siderophore–Drug Conjugates Using a Convergent Thiol–Maleimide System. *ACS Med. Chem. Lett.* **3**, 799 (2012).
107. Wencewicz, T. A. & Miller, M. J. Biscatecholate–Monohydroxamate Mixed Ligand Siderophore–Carbacephalosporin Conjugates are Selective Sideromycin Antibiotics that Target *Acinetobacter baumannii*. *J. Med. Chem.* **56**, 4044 (2013).
108. Wencewicz, T. A., Long, T. E., Möllmann, U. & Miller, M. J. Trihydroxamate Siderophore–Fluoroquinolone Conjugates Are Selective Sideromycin Antibiotics that Target *Staphylococcus aureus*. *Bioconjug. Chem.* **24**, 473 (2013).
109. Milner, S. J. *et al.* Staphyloferrin A as siderophore-component in fluoroquinolone-based Trojan horse antibiotics. *Org. Biomol. Chem.* **11**, 3461 (2013).
110. Souto, A. *et al.* Synthesis and antibacterial activity of conjugates between norfloxacin and analogues of the siderophore vanchrobactin. *Bioorg. Med. Chem.* **21**, 295 (2013).
111. Fardeau, S. *et al.* Probing linker design in citric acid–ciprofloxacin conjugates. *Bioorg. Med. Chem.* **22**, 4049 (2014).
112. Paulen, A., Hoegy, F., Roche, B., Schalk, I. J. & Mislin, G. L. A. Synthesis of conjugates between oxazolidinone antibiotics and a pyochelin analogue. *Bioorg. Med. Chem. Lett.* **27**, 4867 (2017).
113. Liu, R. *et al.* A synthetic dual drug sideromycin induces gram-negative bacteria to commit suicide with a gram-positive antibiotic. *J. Med. Chem.* **61**, 3845 (2018).
114. Miller, M. J., Yun-ming, L. I. N., Ghosh, M., Miller, P. A. & Möllmann, U. Antibacterial sideromycins. *European Patent* (2018).

115. Miller, M. J., Carosso, S., Liu, R. & Miller, P. ANTIBACTERIAL MONOBACTAMS. *World Patent* (2019).
116. Carosso, S. *et al.* Methodology for Monobactam Diversification: Syntheses and Studies of 4-Thiomethyl Substituted β -Lactams with Activity Against Gram-Negative Bacteria, Including Carbapenemase Producing *Acinetobacter baumannii*. *J. Med. Chem.* **60**, 8933 (2017).
117. Zheng, T. & Nolan, E. M. Evaluation of (acyloxy)alkyl ester linkers for antibiotic release from siderophore-antibiotic conjugates. *Bioorg. Med. Chem. Lett.* **25**, 4987 (2015).
118. Neumann, W. & Nolan, E. M. *J. Biol. Inorg. Chem.* **23**, 1025 (2018).
119. Neumann, W., Sassone-Corsi, M., Raffatellu, M. & Nolan, E. M. Esterase-catalyzed siderophore hydrolysis activates an enterobactin-ciprofloxacin conjugate and confers targeted antibacterial activity. *J. Am. Chem. Soc.* **140**, 5193 (2018).
120. Paulen, A. *et al.* Synthesis and antibiotic activity of oxazolidinone-catechol conjugates against *Pseudomonas aeruginosa*. *Org. Biomol. Chem.* **13**, 11567 (2015).
121. Miller, M. J. & Ji, C. REDUCTION-TRIGGERED ANTIBACTERIAL SIDEROMYCINS. *World Patent* (2015).
122. Neumann, W. & Nolan, E. M. Evaluation of a reducible disulfide linker for siderophore-mediated delivery of antibiotics. *J. Biol. Inorg. Chem.* **23**, 1025–1036 (2018).
123. Khan, D. A. *et al.* Cephalosporin Allergy: Current Understanding and Future Challenges. *J. Allergy Clin. Immunol. Pract.* **7**, 2105 (2019).
124. Gupta, K. *et al.* International Clinical Practice Guidelines for the Treatment of Acute Uncomplicated Cystitis and Pyelonephritis in Women: A 2010 Update by the Infectious

- Diseases Society of America and the European Society for Microbiology and Infectious Diseases. *Clin. Infect. Dis.* **52**, e103 (2011).
125. Castro, W., Navarro, M. & Biot, C. Medicinal potential of ciprofloxacin and its derivatives. *Future Med. Chem.* **5**, 81 (2013).
126. Choi, K. Y., Swierczewska, M., Lee, S. & Chen, X. Protease-activated drug development. *Theranostics* **12**, 156 (2012).
127. Baurain, R., Masquelier, M., Deprez-De Campeneere, D. & Trouet, A. Amino acid and dipeptide derivatives of daunorubicin. 2. Cellular pharmacology and antitumor activity on L1210 leukemic cells in vitro and in vivo. *J. Med. Chem.* **23**, 1171 (1980).
128. Poreba, M. Protease-activated prodrugs: strategies, challenges, and future directions. *FEBS J.* **287**, 1936 (2020).
129. Law, C. L. *et al.* Efficient elimination of B-lineage lymphomas by anti-CD20-auristatin conjugates. *Clin. Cancer Res.* **10**, 7842 (2004).
130. Diamantis, N. & Banerji, U. Antibody-drug conjugates—an emerging class of cancer treatment. *Br. J. Cancer* **114**, 362 (2016).
131. Weidle, U. H., Tiefenthaler, G. & Georges, G. Proteases as activators for cytotoxic prodrugs in antitumor therapy. *Cancer Genomics Proteomics* **11**, 67 (2014).
132. Senter, P. D. & Sievers, E. L. The discovery and development of brentuximab vedotin for use in relapsed Hodgkin lymphoma and systemic anaplastic large cell lymphoma. *Nat. Biotechnol.* **30**, 631 (2012).
133. Deeks, E. D. Polatuzumab vedotin: first global approval. *Drugs* **79**, 1467 (2019).
134. Beck, A., Goetsch, L., Dumontet, C. & Corvaia, N. Strategies and challenges for the next generation of antibody-drug conjugates. *Nat. Rev. Drug Discov.* **16**, 315 (2017).

135. Jeffrey, S. C. *et al.* Dipeptide-based highly potent doxorubicin antibody conjugates. *Bioorg. Med. Chem. Lett.* **16**, 358 (2006).
136. Lehar, S. M. *et al.* Novel antibody–antibiotic conjugate eliminates intracellular *S. aureus*. *Nature* **527**, 323 (2015).
137. Mariathasan, S. & Tan, M. W. Antibody-antibiotic conjugates: a novel therapeutic platform against bacterial infections. *Trends Mol. Med.* **23**, 135 (2017).
138. de Groot, F. M. *et al.* Design, synthesis, and biological evaluation of a dual tumor-specific motive containing integrin-targeted plasmin-cleavable doxorubicin prodrug. *Mol. Cancer Ther.* **1**, 901 (2002).
139. Vhora, I., Patil, S., Bhatt, P. & Misra, A. Protein- and peptide-drug conjugates: an emerging drug delivery technology. *Adv. Protein Chem. Struct. Biol.* **98**, 1 (2015).
140. Zheng, G. *et al.* Photodynamic molecular beacon as an activatable photosensitizer based on protease-controlled singlet oxygen quenching and activation. *Proc. Natl. Acad. Sci. U. S. A.* **104**, 8989 (2007).
141. Lo, P. C. *et al.* Photodynamic molecular beacon triggered by fibroblast activation protein on cancer-associated fibroblasts for diagnosis and treatment of epithelial cancers. *J. Med. Chem.* **52**, 358 (2009).
142. Ivry, S. L. *et al.* Global substrate specificity profiling of post-translational modifying enzymes. *Protein Sci.* **27**, 584 (2018).
143. Poreba, M. & Drag, M. Current strategies for probing substrate specificity of proteases. *Curr. Med. Chem.* **17**, 3968 (2012).

144. Janssen, S. *et al.* Screening a combinatorial peptide library to develop a human glandular kallikrein 2-activated prodrug as targeted therapy for prostate cancer. *Mol. Cancer Ther.* **3**, 1439 (2004).
145. Thornberry, N. A. *et al.* A combinatorial approach defines specificities of members of the caspase family and granzyme B. Functional relationships established for key mediators of apoptosis. *J. Biol. Chem.* **272**, 17907 (1997).
146. Choe, Y. *et al.* Substrate profiling of cysteine proteases using a combinatorial peptide library identifies functionally unique specificities. *J. Biol. Chem.* **281**, 12824 (2006).
147. Matthews, D. J. & Wells, J. A. Substrate of protease substrates by monovalent phage display. *Science* **260**, 1113 (1993).
148. Newman, M. R. & Benoit, D. S. In Vivo Translation of Peptide-Targeted Drug Delivery Systems Discovered by Phage Display. *Bioconjug. Chem.* **29**, 2161 (2018).
149. O'Donoghue, A. J. *et al.* Global identification of peptidase specificity by multiplex substrate profiling. *Nat. Methods* **9**, 1095–1100 (2012).
150. Li, H. *et al.* Structure- and function-based design of Plasmodium-selective proteasome inhibitors. *Nature* **530**, 233 (2016).
151. Lapek, J. D. *et al.* Quantitative Multiplex Substrate Profiling of Peptidases by Mass Spectrometry. *Mol. Cell. Proteomics* **18**, 968 (2019).
152. Vizovisek, M. *et al.* Protease specificity: towards in vivo imaging applications and biomarker discovery. *Trends Biochem. Sci.* **43**, 829 (2018).
153. Chen, S., Yim, J. J. & Bogoyo, M. Synthetic and biological approaches to map substrate specificities of proteases. *Biol. Chem.* **401**, 165 (2019).

154. Vizovisek, M., Vidmar, R., Fonovic, M. & Turk, B. Current trends and challenges in proteomic identification of protease substrates. *Biochimie* **122**, 77 (2016).
155. Sobic, B. *et al.* Proteomic identification of cysteine cathepsin substrates shed from the surface of cancer cells. *Mol. Cell. Proteomics* **14**, 2213 (2015).
156. Biniossek, M. L. *et al.* Identification of protease specificity by combining proteome-derived peptide libraries and quantitative proteomics. *Mol. Cell. Proteomics* **15**, 2515 (2016).
157. Laakkonen, P., Porkka, K., Hoffman, J. A. & Ruoslahti, E. A tumor-homing peptide with a targeting specificity related to lymphatic vessels. *Nat. Med.* **8**, 751 (2002).
158. Laakkonen, P. *et al.* Antitumor activity of a homing peptide that targets tumor lymphatics and tumor cells. *Proc. Natl. Acad. Sci. U. S. A.* **101**, 9381 (2004).
159. Jin, W. *et al.* Discovery of PSMA-specific peptide ligands for targeted drug delivery. *Int. J. Pharm.* **513**, 138 (2016).
160. Cieslewicz, M. *et al.* Targeted delivery of proapoptotic peptides to tumor-associated macrophages improves survival. *Proc. Natl. Acad. Sci. U. S. A.* **110**, 15919 (2013).
161. Liu, J. *et al.* Novel peptide-dendrimer conjugates as drug carriers for targeting nonsmall cell lung cancer. *Int. J. Nanomedicine* **6**, 59 (2010).
162. Lempens, E. H., Merckx, M., Tirrell, M. & Meijer, E. W. Dendrimer display of tumor-homing peptides. *Bioconjug. Chem.* **22**, 397 (2011).
163. Hetrick, K. J., Walker, M. C. & van der Donk, W. A. Development and Application of Yeast and Phage Display of Diverse Lanthipeptides. *ACS Cent. Sci.* **4**, 458 (2018).
164. Whitney, M. *et al.* Parallel in vivo and in vitro selection using phage display identifies protease-dependent tumor-targeting peptides. *J. Biol. Chem.* **285**, 22532 (2010).

165. Cloutier, S. M. *et al.* Profiling of proteolytic activities secreted by cancer cells using phage display substrate technology. *Tumor Biol.* **25**, 24 (2004).
166. Dubowchik, G. M. *et al.* Cathepsin B-labile dipeptide linkers for lysosomal release of doxorubicin from internalizing immunoconjugates: model studies of enzymatic drug release and antigen-specific in vitro anticancer activity. *Bioconjug. Chem.* **13**, 855 (2002).
167. Kasperkiewicz, P., Poreba, M., Groborz, K. & Drag, M. Emerging challenges in the design of selective substrates, inhibitors and activity-based probes for indistinguishable proteases. *FEBS J.* **284**, 1518 (2017).
168. Kisselev, A. F. & Goldberg, A. L. Proteasome inhibitors: from research tools to drug candidates. *Chem. Biol.* **8**, 739 (2001).
169. Caculitan, N. G. *et al.* Cathepsin B is dispensable for cellular processing of cathepsin B-cleavable antibody-drug conjugates. *Cancer Res.* **77**, 7027 (2017).
170. Akkari, L. *et al.* Combined deletion of cathepsin protease family members reveals compensatory mechanisms in cancer. *Genes Dev.* **30**, 220 (2016).
171. Kay, B. K., Thai, S., Volgina, V. V. & Doyle, S. A. *High Throughput Protein Expression and Purification*. vol. 498 (2009).
172. Fairhead, M. & Howarth, M. Site-specific biotinylation of purified proteins using BirA. *Methods Mol. Biol.* **1266**, 171 (2015).
173. Neu, H. C. & Heppel, L. A. The release of enzymes from *Escherichia coli* by osmotic shock and during the formation of spheroplasts. *J. Chem. Biol.* **240**, 3685 (1965).
174. Boyce, J. H. *et al.* Platform to discover protease-activated antibiotics and application to siderophore-antibiotic conjugates.

175. Lin, K.-H., Nalivaika, E. A., Prachanronarong, K. L., Yilmaz, N. K. & Schiffer, C. A. Dengue protease substrate recognition: binding of the prime side. *ACS Infect. Dis.* **2**, 734 (2016).
176. Zhong, Y.-J., Shao, L.-H. & Li, Y. Cathepsin B-cleavable doxorubicin prodrugs for targeted cancer therapy. *Int. J. Oncol.* **42**, 373 (2013).
177. Harris, J. L. *et al.* Rapid and general profiling of protease specificity by using combinatorial fluorogenic substrate libraries. *Proc. Natl. Acad. Sci. U. S. A.* **97**, 7754 (2000).
178. Maly, D. J. *et al.* Expedient solid-phase synthesis of fluorogenic protease substrates using the 7-amino-4-carbamoylmethylcoumarin (ACC) fluorophore. *J. Org. Chem.* **67**, 910 (2002).
179. Mensa, B., Howell, G. L., Scott, R. & DeGrado, W. F. Comparative Mechanistic Studies of Brilacidin, Daptomycin, and the Antimicrobial Peptide LL16. *Antimicrob. Agents Chemother.* **58**, 5136 (2014).
180. Beriashvili, D. *et al.* Mechanistic Studies on the Effect of Membrane Lipid Acyl Chain Composition on Daptomycin Pore Formation. *Chem. Phys. Lipids* **216**, 73 (2018).
181. Müller, A. *et al.* Daptomycin Inhibits Cell Envelope Synthesis by Interfering With Fluid Membrane Microdomains. *Proc. Natl. Acad. Sci. U. S. A.* **113**, E7077 (2016).
182. Hill, J. *et al.* Synthesis and Biological Activity of N-Acylated Ornithine Analogues of Daptomycin. *Bioorg. Med. Chem. Lett.* **13**, 4187 (2003).
183. Ghosh, M. & Miller, M. J. Design, synthesis, and biological evaluation of isocyanurate-based antifungal and macrolide antibiotic conjugates: iron transport-mediated drug delivery. *Bioorg. Med. Chem.* **3**, 1519 (1995).

184. Daher, S. S. *et al.* Synthesis and biological evaluation of solithromycin analogs against multidrug resistant pathogens. *Bioorg. Med. Chem. Lett.* **29**, 1386 (2019).
185. Bellenger, J.-P. *et al.* Complexation of oxoanions and cationic metals by the biscatecholate siderophore azotochelin. *J. Biol. Inorg. Chem.* **12**, 367 (2007).
186. Heinisch, L. *et al.* Highly antibacterial active aminoacyl penicillin conjugates with acylated bis-catecholate siderophores based on secondary diamino acids and related compounds. *J. Med. Chem.* **45**, 3032 (2002).
187. Heinisch, L., Moellmann, U., Schnabelrauch, M. & Reissbrodt, R. Synthetic catechol derivatives, method for production and use thereof. *US Patent* (2002).
188. Mollmann, U., Heinisch, L., Bauernfeind, A., Kohler, T. & Ankel-Fuchs, D. Siderophores as drug delivery agents: application of the trojan horse strategy. *Biometals* **22**, 615 (2009).
189. Delorme, D. *et al.* Phosphonated oxazolidinones and uses thereof for the prevention and treatment of bone and joint infections. *World Patent* (2007).
190. Carmona, G., Rodriguez, A., Juarez, D., Corzo, G. & Villegas, E. Improved protease stability of the antimicrobial peptide Pin2 substituted with D-amino acids. *Protein J.* **32**, 456 (2013).
191. Zheng, T., Bullock, J. L. & Nolan, E. M. Siderophore-mediated cargo delivery to the cytoplasm of escherichia coli and pseudomonas aeruginosa: syntheses of monofunctionalized enterobactin scaffolds and evaluation of enterobactin–cargo conjugate uptake. *J. Am. Chem. Soc.* **134**, 18388 (2012).
192. Miller, M. J., McKee, J. A., Minnick, A. A. & Dolence, E. K. The Design, Synthesis and Study of Siderophore-Antibiotic Conjugates. Siderophore Mediated Drug Transport. *Biol. Met.* **4**, 62 (1991).

193. Sklar, J. G., Wu, T., Kahne, D. & Silhavy, T. J. Defining the roles of the periplasmic chaperones SurA, Skp, and DegP in Escherichia coli. *Genes Dev.* **21**, 2473 (2007).
194. Hagan, C. L., Kim, S. & Kahne, D. Reconstitution of Outer Membrane Protein Assembly From Purified Components. *Science* **328**, 890 (2010).
195. Mikkelsen, H., McMullan, R. & Filloux, A. The Pseudomonas aeruginosa reference strain PA14 displays increased virulence due to a mutation in ladS. *PLoS One* **6**, e29113 (2011).
196. Knight, D. B., Rudin, S. D., Bonomo, R. A. & Rather, P. N. Acinetobacter nosocomialis: Defining the role of efflux pumps in resistance to antimicrobial therapy, surface motility, and biofilm formation. *Front. Microbiol.* **9**, 1902 (2018).
197. Chen, T. L. *et al.* Rapid identification of Acinetobacter baumannii, Acinetobacter nosocomialis and Acinetobacter pittii with a multiplex PCR assay. *J. Med. Microbiol.* **63**, 1154 (2014).
198. Mahoney, T. F., Ricci, D. P. & Silhavy, T. J. Classifying β -barrel assembly substrates by manipulating essential Bam complex members. *J. Bacteriol.* **198**, 1984 (2016).
199. Miller, C. G. Peptidases and Proteases of Escherichia Coli and Salmonella Typhimurium. *Annu. Rev. Microbiol.* **29**, 485 (1975).
200. Lazdunski, A. M. Peptidases and proteases of escherichia coli and salmonella typhimurium. *FEMS Microbiol. Rev.* **63**, 265 (1989).
201. Koehbach, J. & Craik, D. J. The vast structural diversity of antimicrobial peptides. *Trends Pharmacol. Sci.* **40**, 517 (2019).
202. Lai, P. K., Tresnak, D. T. & Hackel, B. J. Identification and elucidation of proline-rich antimicrobial peptides with enhanced potency and delivery. *Biotechnol. Bioeng.* **116**, 2439 (2019).

203. Li, W. F., Ma, G. X. & Zhou, X. X. Apidaecin-type peptides: biodiversity, structure-function relationships and mode of action. *Peptides* **27**, 2350 (2006).
204. Dubowchik, G. M. & Firestone, R. A. Cathepsin B-sensitive dipeptide prodrugs. 1. A model study of structural requirements for efficient release of doxorubicin. *Bioorg. Med. Chem. Lett.* **8**, 3341 (1998).
205. Randall, C. P., Mariner, K. R., Chopra, I. & O'Neill, A. J. The target of daptomycin is absent from *Escherichia coli* and other gram-negative pathogens. *Antimicrob. Agents Chemother.* **57**, 637 (2013).
206. Llano-Sotelo, B. *et al.* Binding and action of CEM-101, a new fluoroketolide antibiotic that inhibits protein synthesis. *Antimicrob. Agents Chemother.* **54**, 4961 (2010).

Chapter 5

Structural insights into antibody inhibition of SARS-CoV-2 infectivity and syncytia formation

5.1 Abstract

Infection by SARS-CoV-2 is initiated by binding of viral Spike protein to host receptor angiotensin-converting enzyme 2 (ACE2), followed by fusion of viral and host membranes. While antibodies that block this interaction are in emergency use as early COVID-19 therapies, precise determinants of neutralization potency remain unknown. We discovered a series of antibodies that all potently block ACE2 binding, yet exhibit divergent neutralization efficacy against live virus. Strikingly, these neutralizing antibodies can either inhibit or enhance Spike-mediated membrane fusion and formation of syncytia, which are associated with chronic tissue damage in COVID-19 patients. Multiple cryogenic electron microscopy structures of Spike-antibody complexes reveal distinct binding modes that not only block ACE2 binding, but also alter the Spike protein conformational cycle triggered by ACE2 binding. We show that stabilization of different Spike conformations leads to modulation of Spike mediated membrane fusion, with profound implications in COVID-19 pathology and immunity.

5.2 Introduction

The first step of viral infection by coronaviruses such as SARS-CoV and SARS-CoV-2 is the binding of a Spike protein on the virion to a specific receptor in the membrane of a host cell¹. The virus enters cells by fusion of the viral envelope with cellular plasma membranes and alternatively by endocytosis and subsequent fusion of the viral envelope with endosomal membranes. The SARS-CoV-2 Spike protein, similar to that of other coronaviruses, comprises two subunits, S1 and S2, and is responsible for target recognition and mediating viral entry¹. Upon binding to the host cell receptor through the receptor binding domain (RBD) at the tip of the S1 subunit, the Spike protein undergoes dramatic conformational changes and proteolytic processing. Further shedding of the S1 subunit exposes the S2 subunit fusion peptide, which

inserts into the host cell membrane and induces viral fusion.² Both SARS-CoV-2 and SARS-CoV use the angiotensin converting enzyme 2 (ACE2) as the entry receptor to infect host cells.³⁻⁵ The RBD binds to ACE2 via the receptor binding motif (RBM), a small patch made up of about 20 amino acids.^{6,7}

In addition to mediating viral entry, excess Spike protein in the membranes of coronavirus-infected cells drives neighboring cells expressing ACE2 to fuse and form syncytia (multinucleated giant cells) through a pH-independent mechanism.^{8,9} Syncytia are associated with lung tissue damage in SARS-CoV and MERS-CoV infections, and have been widely observed in autopsies of patients afflicted with severe COVID-19.^{10,11} Preliminary reports also implicate syncytia in chronic cardiovascular injury due to COVID-19.¹²

A common therapeutic strategy against COVID-19 and other coronavirus-related illnesses is blocking of the RBD/ACE2 interaction by antibodies, nanobodies, or soluble ACE2 as a decoy.¹³ Since the first report of COVID-19, many SARS-CoV-2 neutralizing monoclonal antibodies (NAbs) have been discovered from immunized animals^{5,14-16} and COVID-19 convalescent patients.^{14,17-25} Most SARS-CoV-2 NAbs recognize epitopes within the ACE2 binding site, imposing direct competition between the virus-ACE2 interaction^{14,17,18,22,24}, while others bind outside the RBM^{14,15,26} or even the RBD.^{17,19} A number of Nabs in late clinical trials have already been used as experimental treatments for COVID-19¹⁴, with promising efficacy in patients with early-stage infections. Competitive inhibition of receptor binding, denaturation of native Spike conformations,²⁷ and pre-fusion trapping¹⁵ may all contribute to neutralization, but the molecular mechanisms governing neutralization potency of Nabs remain poorly understood, and it is unknown whether receptor-blocking Nabs can also influence Spike mediated cell-cell fusion and syncytia formation.

Neutralizing antibodies against pathogens can also be isolated by *in vitro* selection from highly diverse combinatorial human libraries,²⁸⁻³⁰ and may be distinct from those found in natural infection or by immunization.³¹ We screened a naïve combinatorial human Fab library for antibodies that target the SARS-CoV-2 Spike protein RBD and competitively block ACE2 binding. We discovered a series of antibodies that all exhibit effective receptor blockade, but have strikingly different neutralization potencies against SARS-CoV-2. Taking these antibodies as mechanistic probes, we show that bivalent binding and receptor blockade are not sole determinants of potent neutralization. In addition to blocking ACE2, these antibodies either inhibit or enhance syncytia formation in Vero E6 cells, suggesting that potentiation of cell-cell fusion by antibodies may compromise the effectiveness of viral neutralization in treatment of severe COVID-19. One potentially neutralizing and potentially therapeutic antibody, designated 5A6, uniquely inhibits cell-cell fusion and syncytia formation and blocks receptor binding. High resolution cryogenic electron microscopy (cryo-EM) structures of multiple Spike-antibody complexes provide insight into determinants of viral neutralization potency, and reveal that 5A6 recognizes a cryptic, quaternary epitope that conveys receptor blockade and inhibits syncytia by trapping the pre-fusion state.

5.3 Results

5.3.1 Isolation of SARS-CoV-2 receptor-blocking antibodies from a naïve human library

We identified six antibodies that block the RBD/ACE2 interaction with nanomolar EC_{50} values by phage display of a naïve combinatorial human Fab library comprising 3×10^{10} random heavy and light IgG chain pairs drawn from 22 healthy donors³² (**Figure 5.1, Figure 5.7**).

Whereas the source Fabs had moderate intrinsic affinities for immobilized RBD, as high as 1.6 nM for 3D11 and 7.6 nM for 5A6, clones reformatted as IgGs showed picomolar binding avidity

(**Figure 5.1, Figure 5.8-5.10**). Biolayer interferometry (BLI) of free Fabs and their equivalent IgGs indicates that the greatly enhanced binding of the IgGs is primarily due to slower dissociation, likely due to bivalent binding of both Fab arms to their epitopes (**Figure 5.1**). Stepwise binding BLI assays show that Fab fragments 5A6 and 3D11 have non-overlapping footprints on the RBD, while 5A6 shares at least partially overlapping epitopes with the other four antibodies (**Figure 5.1**).

5.3.2 SARS-CoV-2 neutralization by receptor blocking antibodies

We evaluated the six receptor-blocking antibodies for neutralizing activity against SARS-CoV-2 pseudovirus in CHO-ACE2 cells with a luciferase reporter (**Figure 5.2**) and against live SARS-CoV2³³ in Vero E6 cells by cell viability (**Figure 5.2**). The antibodies neutralize pseudovirus with IC₅₀ values ranging from 75.5 to 428.3 ng/mL, but while neutralization of live virus is 11- to 20-fold less potent for other antibodies, 5A6 retains similar potency with IC₅₀ of 140.7 ng/ml (<2-fold weaker). We speculate that this difference in neutralization potency in live virus and pseudovirus assays is most likely due to the non-replicating nature of pseudoviruses, which are thereby more sensitive to blockade of viral entry. We validated live virus neutralization of a subset of antibodies (2H4, 3D11 and 5A6) using a RT-qPCR to quantify viral replication (**Figure 5.11**), and observed similar trends as obtained from cell viability assays (**Figure 5.2**). To more accurately assess the therapeutic potential of 5A6, we studied its neutralizing potency in SARS-CoV-2 infection of human airway epithelia (HAE).³⁴ SARS-CoV-2 replication in HAE was reduced 1000-fold by 5A6 at 75 ng/mL and 10,000-fold at 150 ng/mL, and 5A6 also helped maintain epithelium integrity (represented by trans-epithelia electrical resistance), supporting its activity in a physiologically relevant *in vitro* model (**Figure 5.2**).

All IgGs effectively block ACE2-RBD binding, with IC_{50} values below 50 nanomolar (**Figure 5.7**). Therefore, the relative viral neutralization potencies of these antibodies cannot be ascribed to competitive receptor blocking alone. In order to interrogate other determinants of neutralization, we next compared the potency of each IgG antibody to their respective monomeric Fab fragments. A bivalent ACE2-Fc fusion protein was included as a reference for multivalent receptor blockade. All antibodies show dramatically increased potency against live virus compared to Fab, which is consistent with bivalent engagement of the Spike trimer by the IgG compared to the monovalent Fab fragment. The affinity or avidity for RBD is generally predictive of viral neutralization IC_{50} , with two striking exceptions (**Figure 5.2**). Antibody 5A6 exhibits far greater viral neutralization potency than other antibodies with superior avidity. Conversely, 3D11 is among the least potent in viral neutralization despite displaying the strongest binding.

We asked if the discrepancy could arise from the differences in the structural arrangement of IgGs bound to the RBDs of intact, trimeric Spike on the virion. We used surface plasmon resonance (SPR) to measure antibody binding to immobilized Spike trimers, as opposed to immobilized RBD (**Figure 5.16**). Although kinetics of binding to trimer were largely similar, we noted that 5A6 IgG binds somewhat more tightly (3.6x) to the intact trimer than to the flexible RBD-Fc construct used for BLI, while 3D11 IgG binds much (18.7x) more weakly (but still apparently bivalently, with 21.7x tighter binding than 3D11 Fab). To further investigate the relationship of the antibodies to intact Spike assemblies, we purified SARS-CoV-2 pseudovirus by gradient centrifugation and immobilized the viral particles on ELISA plates (**Figure 5.2**). The higher optical signal at saturation in concentration-dependent binding curves reveals that 5A6 IgG likely packs with higher density on the viral surface than the other four tested IgG antibodies

or 5A6 Fab. It has been proposed that effective viral neutralization requires antibody packing density exceeding a critical threshold³⁵⁻³⁷ and 5A6 may possess a unique binding mode that accommodates a denser structural arrangement on the viral surface. Notably, 3D11 IgG exhibits a similarly high signal at saturation, but with lower affinity for the pseudoviral particles, despite having *higher* affinity than 5A6 for immobilized RBD or Spike trimer (**Figure 5.2, Figure 5.16**). Finally, 2H4 and 1F4 IgGs saturate immobilized pseudovirus at 1/3 the density of 5A6 or 3D11, while neutralizing live virus slightly more effectively than 3D11. These results suggest at least three different classes of receptor-blocking antibodies with distinct structural relationships to RBDs on viral particles.

5.3.3 Neutralizing antibodies inhibit or enhance Spike-mediated cell fusion

It is widely appreciated that viral proteins often possess multiple critical functions. With receptor-blocking activity and avid binding eliminated as sole determinants of neutralization by prior experiments, we reasoned that 5A6 might interfere with additional functions of the SARS-CoV-2 Spike. The most prominent example is induction of fusion of infected cells with neighboring cells, leading to formation of syncytia (multinucleated giant cells), a phenomenon known to hasten disease progression in respiratory syncytial virus³⁸ and human immunodeficiency virus,^{39,40} and now widely observed in late-stage COVID-19.¹⁰ We therefore assessed whether antibodies discovered in our campaign inhibit Spike-mediated syncytia formation. To directly examine syncytia formation by Spike alone, we expressed Spike protein with a C-terminal fluorescent tag in VeroE6 cells. Addition of trypsin as an exogenous Spike-processing enzyme resulted in cells with a diffuse fluorescent signal and multiple nuclei, indicative of syncytia formation. (**Figure 5.3**). We assayed the impact of receptor-blocking

antibodies on this trypsin-induced cell-cell fusion, using antibodies 2H4, 5A6 and 3D11, which represent different modes of viral neutralization. The 5A6 IgG has a dose-dependent inhibitory effect on syncytia (**Figure 5.3**). By contrast 2H4 IgG has no significant effect. Surprisingly, 3D11 potentiates cell-cell fusion. Furthermore, 5A6 Fabs also enhanced syncytial fusion, albeit weakly (**Figure 5.3**). We conclude that 5A6 IgG directly inhibits Spike-mediated fusion, while other receptor blocking antibodies fail to inhibit or even accelerate this process.

5.3.4 Structures of Spike-Fab complexes

The Spike trimer exists in equilibrium between the closed conformation, with all RBDs nestled closely around the S2 subunit, and “receptor seeking” states featuring one or more open RBDs that become erect and disengage from the S2.^{4,16,41} To provide structural insights into how antibodies targeting different RBD epitopes divergently modulate Spike protein function, we determined structures of the trimeric Spike protein alone (**Figure 5.13**), and in complex with Fab fragments of 3D11, 2H4, and 5A6. Consistent with epitope binning and functional characterization, these Fabs explore different regions of the RBD surface, are compatible with different (open or closed) RBD states in the Spike trimer, and bind with distinct geometries relative to the RBD and ACE2 interface (**Figure 5.4**). This form of three-dimensional epitope mapping provides atomic level understanding of the determinants of viral inhibition.

5.3.5 2H4 is an orthosteric receptor-mimetic antibody

We determined multiple structures of 2H4 Fab bound to Spike with resolution sufficient for unambiguously docking a model of 2H4, but precluding precise modelling of the epitope and complementarity determining regions (CDRs) (**Figure 5.13**). Three major conformational states

were identified by 3D classification, revealing either one, two, or three 2H4 Fabs bound to the Spike trimer. The receptor blocking activity of 2H4 is straightforward, as it recognizes an epitope that overlaps much of the ACE2 interface (**Figure 5.4**). Binding of the 2H4 Fab is compatible with both major RBD conformations, and the structures are drawn from an ensemble of quaternary states reminiscent of those that follow ACE2 binding, and lead to S1 shedding and spike-mediated membrane fusion² (**Figure 5.4**). The first of three predominant states features 2H4 bound to one open RBD, and the other two RBDs closed. The second state adds a second copy of 2H4, on a closed RBD counter-clockwise from the first. Density inspection and 3D variability analysis (3DVA)⁴² reveal that the third RBD is primarily open, and a trajectory of opening states correlate with binding the second Fab. The final state features three Fabs bound, and a strictly open third RBD. This restricted ensemble arises because when the bound RBD is closed, the Fab incurs clashes with the counter-clockwise adjacent RBD that can only be relieved by opening of that RBD and NTD, even beyond the degree of opening in the triple ACE2 complex with three open RBDs² (**Figure 5.4**). These observations suggest 2H4 directly blocks receptor binding, but also acts as a receptor-mimetic that admits the same cycle of Spike conformations as does ACE2. A neutralizing antibody against SARS-CoV has also been reported to engage in orthosteric receptor mimicry,⁴³ suggesting activation of fusion-associated conformational changes may be an intrinsic consequence of direct receptor interface binding in betacoronaviruses.

5.3.6 3D11 allosterically blocks ACE2 binding and triggers Spike opening

The Spike:3D11 complex is relatively homogeneous, with only one major state, and we determined its structure to ~ 3.0 Å resolution (**Figure 5.12**). All three RBDs are bound to 3D11

Fab in the open conformation, with the Fab making a right angle to the long axis of the RBD, via an epitope exposed only in the open state and outside the RBM (**Figure 5.4**). The epitope partly overlaps those of some other antibodies that bind outside the RBM,^{44,45} but is distinct from those^{26,46} that bind freely to a closed RBD (**Figure 5.13**). Clashes between 3D11 and Spike NTDs also prevent 3D11 binding to closed RBDs, indicating 3D11 binds only to open RBDs. This restriction of binding to the subset of Spike conformations with open RBDs might account for lessened avidity of 3D11 IgG for the intact Spike trimer, as compared with RBD (**Figure 5.15**). 3D classification reveals outward motions of the NTD and variation in Fab occupancy, but only open RBDs are observed (**Figure 5.13**). As for 2H4, the 3D11 bound RBDs are “more open” (displaced further outward) than those in the triple ACE2 complex (**Figure 5.4**).

Although its epitope does not significantly overlap with the ACE2-RBD interface, 3D11 nevertheless effectively blocks ACE2 binding and stabilizes a quaternary state of the Spike, with three open RBDs and NTDs, that closely resembles the penultimate stage of ACE2-induced Spike opening.² We therefore term 3D11 an allosteric receptor-mimetic antibody, which does not directly target the ACE2 interface, yet prevents ACE2 binding and enhances Spike-mediated fusion by rapidly advancing the Spike conformational cycle to its final stages.

5.3.7 5A6 traps a pre-fusion conformation to inhibit spike-mediated fusion

Multiple states of the Spike:5A6 complex were resolved to better than 3.0 Å, with local resolution sufficient for accurate modelling of the Fab-RBD interface (**Figure 5.12**). 5A6 recognizes surface loops near the tip of the RBD, which are solvent exposed even when all RBDs are closed. The binding geometry is permissive of any trimer configuration and any stoichiometry, without steric constraints from Spike or Fab. Yet despite this complete

conformational freedom, all 5A6 complexes feature at least two 5A6 Fabs bound to an open RBD counter-clockwise adjacent in turn from a closed RBD (**Figure 5.4**). The hallmark of these states is a cryptic, quaternary epitope in which a region of the Fab V_L domain makes a second interaction with an adjacent, open RBD (**Figure 5.4**). This new interaction is not possible with a closed RBD, and requires an adjustment away from the average positions of open RBDs in other structures (**Figure 5.13**). The closed RBD bound via the main 5A6 interface is also displaced from other closed conformations.

CDR loops H1, H2, H3, and L1 engage the canonical epitope with a buried surface area of 850 Å² (**Figure 5.5**). Partial overlap of the RBM and Fab interface, and a clash induced between ACE2 and the Fab V_L domain, are likely sufficient to exclude ACE2 from the RBD. The second interaction contributes an additional 363 Å² (**Figure 5.5**), and the C_{H1} and C_L domains of 5A6 at the cryptic quaternary epitope induce an even more severe clash with ACE2 (**Figure 5.4**). Two Fabs thus act synergistically to block ACE2 binding, while one Fab is capable of blocking ACE2 at two RBDs simultaneously. The secondary interface must be released in order for the bound RBD to open, and we hypothesize that 5A6 at its quaternary epitope locks one RBD closed, thereby arresting the trimer in its pre-fusion state. Precise conservation of binding mode and the cryptic quaternary epitope from free Fab to IgG is confirmed by a structure of 5A6 IgG complexed with Spike trimer at ~15 Å resolution (**Figure 5.5**). Although the Fc domain is not well resolved due to the flexibility of the hinge region, the structures suggest 5A6 IgG may bind to two RBDs from the same trimer (**Figure 5.13**), and shows that no steric effects preclude binding of three IgGs at sufficient concentration. Noting the weak potentiation of syncytia formation by 5A6 Fab, we deduce that the cryptic epitope likely appears following initial Fab binding, and leads to cooperative action against SARS-CoV-2 by imbuing a second

binding event with enhanced affinity and receptor blockade. We also conclude that the geometry of the quaternary epitope and avidity of 5A6 IgG drive robust pre-fusion conformational trapping and potent inhibition of Spike-mediated fusion and syncytia formation.

5.4 Discussion

Receptor engagement to a Spike RBD locks it in the open conformation and triggers a cooperative process in which the Spike conformational ensemble is driven toward further opening by successive rounds of receptor binding.² The process culminates in unsheathing of the S2 subunit and, following proteolytic cleavage, shedding of the S1-ACE2 subcomplex. S1 shedding, in turn, facilitates the post-fusion state transition, leading to membrane fusion and virus entry. The Spike protein on the surface of infected cells can also mediate ACE2-dependent fusion of neighboring cells to form multinucleated giant cells, presumably through the same cycle of proteolysis and conformational transitions. Genetic variation in Spike, in and outside of the RBM, can influence function by altering the conformational equilibrium of the trimer, as seen for the D614G variant, which more readily populates states with multiple open RBDs⁴¹ and exhibits heightened infectivity.⁴⁷ We identified six receptor-blocking antibodies that exhibit differences in avidity, binding mode, and neutralization of the live virus despite the fact that all of them have similarly high affinities for the RBD of the viral Spike protein. Strikingly, one highly potent neutralizing antibody inhibits Spike-mediated syncytium formation, whereas another, more weakly neutralizing antibody actually potentiates cell-cell fusion. These findings suggest that the potential effectiveness of a neutralizing antibody is influenced by a number of possibly countervailing factors, highlighting a complex basis for viral neutralization potency, contra a simplistic view where receptor blocking and affinity enhancement through avidity are the sole determinants of viral neutralization. Cryo-EM structures reveal the conformational

landscapes of three Spike Fab complexes and provide 3D mapping of antibody-Spike epitopes, from which we can draw mechanistic insights that explain their distinct bioactivities in terms of the known intermediates in Spike opening (**Figure 5.6**). Certain receptor-blocking antibodies, such as 2H4, may function as orthosteric receptor mimetics conducive to the same cooperative processes as receptor binding. Another class of antibodies, exemplified by 3D11, act as allosteric effectors that advance the Spike directly to the final stages of S2 unsheddung. In contrast, 5A6 possesses a unique binding mode that stabilizes a Spike conformation that prohibits S1 shedding and traps the pre-fusion state. We hypothesize that synergy between receptor blockade and pre-fusion trapping allows 5A6 to prevent targeted viral fusion and Spike mediated cell-cell fusion. Directly comparing the monovalent Fabs and bivalent IgGs also provides insight into the nature of avidity. The magnitude of binding and neutralization enhancement in the IgG format supports bivalent binding for all six antibodies.⁴⁸ This result may be counterintuitive because modeling studies suggest that the hinge linking IgG Fc and Fab domains may have difficulty bridging the gaps seen in our structures of Spike:Fab complexes (**Figure 5.10**). On the other hand, our structure of the 5A6 IgG complex confirms that 5A6 Fab and IgG forms do bind with congruent geometries, and a morph between 5A6 Fab bound to closed and open RBDs shows that shorter distances between Fabs do obtain for intermediate RBD conformations. These results may imply that high-affinity bivalent binding to intermediate RBD conformations is replaced by high-density monovalent binding as the concentration of 5A6 IgG increases. In contrast to 5A6, 3D11 and 2H4 Spike:IgG complexes were not tractable for single-particle cryo-EM (**Figure 5.10**). Qualitative image analysis suggests that these species do not trap defined conformational states of the Spike trimer, and that 3D11 in particular may achieve virus neutralization by destabilizing the Spike, as does the CR3022 antibody with a similar epitope.²⁷ Intriguingly, we found that

3D11 has greatly reduced potency against the pseudovirus bearing D614G Spike, whereas that of 5A6 is slightly improved, although position 614 is outside of the RBD and far from the epitope of either antibody in the RBD (**Figure 5.12**). The D614G mutant Spike is known to occupy states with multiple open RBDs⁴¹ and has been found to shed the S1 subunit less readily than the original SARS-CoV-2 Spike protein.⁴⁹ We can thus understand altered neutralization of D614G pseudovirus by 3D11 and 5A6 in terms of the model in Figure 5.6 because the effects of both antibodies are mediated by open RBD conformations that represent immediately available binding sites for 3D11 and present the full quaternary epitope of 5A6. The reduced S1 shedding of the more stable D614G Spike may also assist with the pre-fusion trapping activity of 5A6 while conveying resistance against trimer denaturation by 3D11. The quaternary epitope recognized by 5A6 conveys cooperative binding as well as avidity, and both aspects may hinder virus escape via mutations in Spike protein.⁴⁶ In summary, our work establishes a platform for exploring allosteric control surfaces across the SARS-CoV-2 Spike protein. Although we employ syncytium formation as a general model for Spike protein function, pre-fusion trapping by 5A6 may convey greater efficacy against late-stage or severe illness because of the role of syncytia in COVID-19 pathology.¹⁰ Notably, cell-cell fusion during respiratory syncytial virus (RSV) infection also leads to severe tissue damage, and the therapeutic antibody palivizumab is known to trap a pre-fusion state of the fusogenic F protein of RSV.⁵⁰ Uncovering the particular modes of action and functional consequences of Spike binders in general may deepen our understanding of avidity, virus neutralization, and disruption of syncytium formation and play a role in development of therapeutic agents or vaccines during the ongoing COVID-19 pandemic.

5.5 Materials and Methods

Antibody discovery from phage display library

Anti-SARS-CoV-2 Spike RBD antibodies were isolated from an HX02 human Fab phage display library (Humanyx Pte Ltd) via *in vitro* selection. Briefly, biopanning was performed using SARS-CoV-2 RBD (YP_009724390.1) (Arg319-Phe541) with a mouse Fc tag (Sino Biological, 40592-V05H) biotinylated using the EZ-Link NHS-PEG4-Biotin labelling kit (Thermo Fisher Scientific, #A39259). In both rounds of biopanning, biotinylated SARS-CoV-2 RBD-mFc protein was immobilized on M280 streptavidin-coated magnetic beads (Life Technologies, #11205D); 3.5×10^{12} cfu phage in 1mL 1% casein-PBS blocking buffer was used in the first round, and 1.64×10^{11} cfu phage were used in the second round. During the biopanning process, binders to mouse Fc were removed by pre-incubation of phage with 2 μ M mouse IgG before mixing with the RBD-mFc antigen. After two rounds of biopanning, the Fabs of selected clones were expressed in *E. coli* HB2151 cells (Stratagene) to screen for RBD binders by ELISA. Unique clones were identified by DNA sequencing.

IgG expression and purification

Fabs were reformatted into human IgG in the pTT5 vector (National Research Council of Canada) and the IgG antibodies were expressed using ExpiCHO expression system (Thermo Fisher Scientific) by transient co-transfection of plasmids expressing the heavy and light chain of each antibody clone. Eight days after transfection, ExpiCHO-S cell suspension was centrifuged for 10 min at 2000 rpm and filtered with 0.22 μ m filter to remove the cells and debris.

Antibodies were then purified from the culture supernatant using Protein G resin (Merck Millipore) following the manufacturer's instructions. After elution, the purified antibodies were

dialyzed at 4°C for 4-20 hours against 1x PBS, for 3 times and concentrated to 1-2 mg/ml using 10MWCO Vivaspin 20 (Sartorius).

Fab production and purification

The tag-less Fab fragments were produced using the ExpiCHO transient expression system. Eight days after transfection, ExpiCHO-S cell suspension was centrifuged and filtered; and Fab was purified from the filtered culture supernatant using cation exchange chromatography (CIEX) on AKTA FPLC System (GE Healthcare). In brief, the supernatant was concentrated to 2 ml using 10MWCO Vivaspin 20 (Sartorius), diluted 1:20 in Buffer A (20 mM Sodium Acetate, pH 5.2), filtered through 0.22 µm filter, and loaded onto Mono-S 5/50 GL column at a flow rate of 1ml/min. Fab fragments were eluted in Buffer B (20 mM Sodium Acetate, pH 5.2 with 1 M Sodium Chloride) with a sequential linear gradient of 0% to 5% in 5 min, 5% to 15% in 30 min, and 15% to 100% in 20 min of Buffer B injection at a flow rate of 1 ml/min. The resulting purified Fab fragments were dialyzed at 4°C for 4-20 hours against 4 liters of 20 mM Histidine, 150 mM NaCl, pH 6.6, for 3 times and concentrated to 1-2 mg/ml using 10MWCO Vivaspin 6 (Sartorius).

Avidity binding ELISA to recombinant RBD proteins

Anti-SARS-CoV-2 Spike RBD IgG antibodies were tested in an ELISA against biotinylated recombinant SARS-CoV-2 Spike protein RBD-mFc (Sino Biological, 40592-V05H) or SARS-CoV Spike protein RBD-His (Sino Biological, 40150-V08B2) to assess binding avidity for the target. In brief, NeutrAvidin protein (Thermo Fisher Scientific, #31000) was coated at 5 µg/ml onto 96-well ELISA plates in coating buffer (8.4 g/L NaHCO₃, 3.56 g/L Na₂CO₃, pH 9.5) overnight at 4°C. After blocking with 1% Casein (Thermo Fisher Scientific, #A37528) for two hours, biotinylated antigen at 0.2 µg/ml was added to the plates and captured by NeutrAvidin

during one-hour incubation at room temperature. After washing with 0.05% PBST for 5 times, the IgG antibodies were added at different concentrations with 3-fold dilutions in triplicate and incubated for one hour. The wells were then washed again with 0.05% PBST, followed by addition of HRP conjugated anti-human Fc antibody (1:3000). Finally, the wells were washed and the HRP activity was measured at 450 nm with addition of 3,3',5,5'-tetramethylbenzidine (TMB) substrate (Surmodics, BioFX®, TMBW-1000-01).

Avidity binding ELISA to purified pseudoviral particles

Anti-SARS-CoV-2 Spike RBD IgG antibodies were tested in an ELISA against iodixanol-gradient-purified SARS-CoV-2 pseudoviruses with an isotype IgG used as a negative control antibody. In brief, 1 µg/ml of pseudoviral particles were coated in coating buffer onto 96-well ELISA plates overnight at 4°C. After blocking with 1% Casein (Thermo Fisher Scientific, #A37528) for two hours, serially diluted IgG antibodies starting from 100 nM with five-fold dilutions were added to the plates and incubated for an hour at room temperature. The wells were then washed again with 0.05% PBST, followed by addition of HRP conjugated anti-human Fc antibody (Thermo Fisher Scientific, #A21445, 1:3000) for one-hour incubation before HRP activity was measured at 450 nm with addition of TMB substrate.

Competition ELISA

Anti-SARS-CoV-2 Spike RBD IgG antibodies were tested in a competition ELISA to assess their ability to block the Spike protein RBD from binding to human ACE2 protein. In brief, the recombinant human ACE2 protein with a human Fc tag (ACE2-Fc) was coated onto the 96-well ELISA plates in coating buffer overnight at 4°C and blocked with 1% Casein. Then different concentrations of anti-SARS-CoV-2 Spike RBD IgG antibodies were pre-incubated with 0.5 nM biotinylated Spike protein RBD-mFc for one hour at room temperature before they were added to

the ELISA plates coated with ACE2-Fc. After one-hour incubation, the wells were washed with 0.05% PBST for five times and HRP conjugated streptavidin was added at a dilution of 1:3000, and incubated for another one hour before HRP activity was measured at 450 nm with addition of TMB substrate.

Cell lines and cell culture

The human embryonic kidney epithelial cell 293T (ATCC, CRL-3216) was cultured in Dulbecco's modified Eagle's medium (Hyclone, SH30022.01) supplemented with 10% heat-inactivated FBS (Gibco, 10270-106). A stable cell line expressing human ACE2, CHO-ACE2 (a kind gift from Professor Yee-Joo Tan, IMCB, A*Star) (Ng et al., 2014) was maintained in Dulbecco's modified Eagle's medium supplemented with 10% heat-inactivated FBS, 1% MEM Non-Essential Amino Acids Solution (Gibco, 11140-050) and 0.5 mg/ml of Geneticin™ Selective Antibiotic (Gibco, 10131-027). Every 2-3 days, cells were passaged by dissociating the cells with StemPro™ Accutase™ Cell Dissociation Reagent (Gibco, A1110501).

Conversion of IgG antibodies to Fab fragments

Digestion reaction for each IgG was prepared using immobilized FabALACTICA microspin columns (Genovis). 100 µL of IgG at 5 mg/mL concentration in digestion buffer (150 mM sodium phosphate, pH 7.0) were incubated overnight on each column. Digested sample was further purified using a HiTrap Protein L column followed by size-exclusion chromatography (Superdex 75 10/300 GL) using an Äkta Pure FPLC (all GE Healthcare).

Soluble SARS-CoV-2 Spike Production and Purification

The expression plasmid containing the prefusion S ectodomain as used in Wrapp, et al.¹⁶ was kindly provided by Prof. Jason McLellan (University of Texas at Austin). This construct was

used to transiently transfect high-density Chinese Hamster Ovary (ExpiCHO) cells with ExpiFectamine per the “Max Titer” protocol provided (Thermo Fisher). Six days post-transfection, 0.2 μm -filtered supernatant was collected and incubated with Ni-Sepharose Excel (Cytiva Life Sciences) for batch purification. Eluate was collected, concentrated in a 50 MWCO Amicon Ultra-15 centrifugal filter unit (MilliporeSigma), and injected onto a Superose6 10/300 GL column equilibrated in 10 mM HEPES, 200 mM NaCl, pH 8.0 to isolate trimeric, monodisperse material for Fab/IgG complexing.

Cryo-EM sample preparation and imaging

2.5 μL of Spike-Fab complex at a concentration of 0.4 mg/mL was applied to a 300 mesh gold Quantifoil 1.2/1.3 holey carbon grid that was glow discharged for 30 sec at 15 mA immediately before sample application. Grids were blotted using Whatman #1 filter paper for 8 or 10 seconds at a blot force of 0 at 4°C and 100% humidity using a Mark IV Vitrobot (Thermo Fisher) and plunge frozen into liquid ethane. Samples were loaded onto a Titan Krios transmission electron microscope (Thermo Fisher) equipped with a Gatan K3 direct electron detector (Gatan) and a Quantum GIF energy filter (Gatan) operated with a 20 eV slit width during image acquisition. The K3 camera was operated in CDS mode using super resolution. A nominal magnification of 105,000x was used, for a pixel size of 0.835 Å (0.4175 Å super resolution pixel size) at the sample. A dose rate of 8 $\text{e}^-/(\text{pix} \cdot \text{sec})$, or 11.5 $\text{e}^-/(\text{Å}^2 \cdot \text{sec})$, and a frame rate of 0.05 sec/frame was used with a total exposure time of 5.9 sec, for a total dose of 67.7 $\text{e}^-/\text{Å}^2$. Automated data collection was performed using SerialEM.⁵¹

Image processing

Dose-weighted, motion-corrected sums down-sampled to the physical pixel size were obtained from the super-resolution DED movies using UCSF Motioncor2.⁵² For the Spike trimer, CTF

estimation was performed in cryoSPARC⁵³ followed by blob-based particle picking, 2D classification, *ab initio* modelling, 3D classification, and 3D refinement. For images of antibody complexes, particles were instead picked using templates generated from the apo trimer structure, and the apo trimer was likewise used as an initial model in 3D classification. The resolution of the interface between the Spike RBD and the 5A6 Fab was further improved using naïve focused refinements. Processing details are given in **Table 5.1** and **Figure 5.14**.

Molecular modeling

For each Spike:Fab complex, a previously determined structure of the SARS-CoV-2 Spike protein, along with a full-length Fab homology model computed by MODELER,⁵⁴ were simultaneously docked into cryo-EM density using UCSF Chimera.⁵⁵ Spike with one open RBD and one copy of ACE2 bound (PDB: 7a94) was used with 5A6, Spike with three open RBDs and three copies of ACE2 bound (PDB: 7a98) was used with 3D11, and Spike with two open RBDs and one copy of ACE2 bound (PDB: 7a95) was used with 2H4. Missing segments and side chains in the RBDs were built using Coot. Interactive, density-restrained molecular dynamics simulations in ChimeraX⁵⁶ and ISOLDE⁵⁷ were used to finalize the models, and atomic b-factors were calculated using PHENIX.⁵⁸ Models for the Spike:5A6 and Spike:3D11 complexes were first built into density maps from whole-particle cryo-EM reconstructions, and then further refined using maps from focused refinements of the Fab and Spike RBD. Maps of Spike:2H4 complexes were of lower resolution and model building was terminated after the docking step described above. Model statistics and density fit information are presented in **Table 5.3** and **Figure 5.11**.

Generation of pseudovirus particles

Pseudotyped viral particles expressing SARS-CoV-2 Spike protein were produced by transfecting of 30 million 293T cells with 12 mg pMDLg/pRRE (a gift from Didier Trono, Addgene #12251), 6 mg pRSV-Rev (a gift from Didier Trono, Addgene #12253), 24 mg pHIVLuc-ZsGreen (a gift from Bryan Welm, Addgene #39196) and 12 mg pTT5LnX-CoV-SP (expressing SARS-CoV-2 Spike protein, GenBank: YP_009724390.1, a kind gift from DSO National Laboratories) using Lipofectamine 2000 transfection reagent (Invitrogen, Cat#11668-019). The transfected cells were cultured at 37C incubator for 3 days. Viral supernatant was harvested, centrifuged at 700 g for 10min to remove cell debris and filtered through a 0.45 mm filter unit (Sartorius, Cat#16555). Lenti-X p24 rapid titer kit (Takara Bio, Cat#632200) was used to quantify the viral titers following the manufacturer instructions. pTT5LnX-CoV-SP plasmid with D614G mutation was generated using QuickChange Lightning Multi Site-Directed Mutagenesis Kit (Agilent, Cat#210513) and was used to generate mutant pseudovirus expressing SARS-CoV-2 Spike protein carrying D614G mutation.

Purification of pseudovirus particles

To concentrate and purify the pseudovirus particles expressing the SARS-CoV-2 Spike glycoproteins, pre-cleared 40 mL viral supernatant was concentrated by 20% sucrose gradient centrifugation at 10,000 g for 4 hours at 4C in an SW41 Ti rotor with no brake. Upon removal of supernatant, 1mL of PBS was added to the virus pellet and left at 4C overnight. Concentrated virus was further purified by an OptiPrep (60% [wt/vol] iodixanol, STEMCELL Technologies, Cat#07820) velocity gradient. Iodixanol gradients were prepared in PBS in 1.2% increments ranging from 6 to 18%. Pseudoviruses were layered onto the top of the gradient and centrifuged

for 1.5 hours at 200,000 g in an SW41 Ti rotor. Gradient fraction that contained pseudovirus pellet was collected.

Pseudovirus neutralization assay

CHO-ACE2 cells were seeded at a density of 3.2×10^4 cells in 100 mL of complete medium without Geneticin in 96-well Flat Clear Bottom Black Polystyrene TC-treated Microplates (Corning, Cat#3904). Serially diluted IgG or Fab antibodies were incubated in a 96-well flat-bottom cell culture plate (Costar, Cat#3596) with an equal volume of pseudovirus (12 ng of p24) at the final volume of 50 mL at 37C for one hour, and the mixture was added to the monolayer of pre-seeded CHO-ACE2 cells in triplicate. After one hour of pseudovirus infection at 37C, 150 ml of culture medium was added to each well and the cells were further incubated for another 48 hours. Upon removal of culture medium, cells were washed twice with sterile PBS, and then lysed in 20 mL of 1x Passive lysis buffer (Promega, Cat#E1941) with gentle shaking at 37C for 30 minutes. Luciferase activity was then assessed using a Luciferase Assay System (Promega, Cat#E1510) on a Promega GloMax Luminometer. The relative luciferase units (RLU) were converted to percent neutralization and plotted with a non-linear regression curve fit using GraphPad PRISM.

Live virus neutralization assay in Vero E6 cells

The potency of the IgG or Fab antibodies were determined in neutralizing live SARS-CoV-2 virus assays. In brief, 25 ml of 100 TCID₅₀ of SARS-CoV-2 live virus (isolated from a nasopharyngeal swab of a patient in Singapore) was mixed with an equal volume of serially diluted IgG or Fab antibodies and incubated at 37C for one hour before the mixture was added to 50 ml of Vero E6 C1008 cells in suspension. The infected cells were incubated at 37C incubator for four days and the cell viability was determined using Viral ToxGlo™ Assay (Promega,

Cat#G8941). The potency of 2H4, 3D11 and 5A6 IgG antibodies in neutralizing live SARS-CoV-2 virus assays was also determined by measuring the viral genome copy number (GCN). 25 ml of 100 TCID₅₀ of SARS-CoV-2 live virus (isolated from a nasopharyngeal swab of a patient in Singapore) was mixed with an equal volume of serially diluted 2H4, 3D11 or 5A6 IgG antibodies and incubated at 37C for one hour before the mixture was added to 50 ml of 4x10⁵ Vero E6 C1008 cells in suspension. The infected cells were incubated at 37C incubator for 48 hr after which supernatant was harvested and viral GCN was determined by subsequent RT-qPCR targeting the N gene using the RESOLUTE 2.0 kit as per manufacturer's instructions. Briefly, 2.5 ml of supernatant was diluted with 2.5 ml of Milli-Q water and added to 20 ml of RT-PCR master mix. PCR was carried out as follows: reverse transcription at 55C for 15min, inactivation at 95C for 4min, followed by 45 cycles of amplification consisting of denaturation at 95C for 3 s and annealing/extension at 62C for 30 s and GCN values determined by comparing Ct values against a logGCN standard curve.

Live virus neutralization assay in HAE

The potency of 5A6 IgG was tested in neutralizing a live virus strain (BetaCoV/France/IDF0571/2020) using MucilAir™ HAE (human airway epithelia) model. Briefly, the apical poles of HAE were gently washed twice with warm Opti-MEM medium (GIBCO, Thermo Fisher Scientific) and then infected directly with a 150 mL dilution of live SARS-CoV-2 virus strain (BetaCoV/France/IDF0571/2020) in Opti-MEM medium, at a multiplicity of infection (MOI) of 0.1. Viral suspensions were pre-incubated for 60 min with antibody 5A6 IgG (75 ng/ml or 150 ng/ml) or an anti-Ebola glycoprotein control antibody (150 ng/ml) before infection. A control infection was performed in absence of antibody. For mock infection, the same procedure was followed using Opti-MEM as inoculum. Viral replication was

quantified as the measured copy number of the viral genomes inside, and at the apical poles of, nasal and bronchial HAE. Samples collected from apical washes at 48 hours post-infection were separated into 2 tubes: one for TCID₅₀ viral titration (stored at 80C) and one for RT-qPCR. HAE cells were harvested in RLT buffer (QIAGEN) and total RNA was extracted using the RNeasy Mini Kit (QIAGEN) for subsequent RT-qPCR. Primer and probe sequences targeting the ORF1b-nsp14 (forward primer HKU-ORF1b-nsp14F: 5' -TGGGGYTTTACRGGTAACCT-3' ; reverse primer HKU-ORF1b-nsp14R: 5' -AACRCGCTTAACAAAGCACTC-3' ; probe HKU-ORF1b-nsp14IP: 5' -FAM-TAGTTGTGATGCWATCATGACTAG-TAMRA-3') were selected from those designed by the School of Public Health/University of Hong Kong (Leo Poon, Daniel Chu and Malik Peiris) and synthesized by Eurogentec. Real-time one-step RT-qPCR was performed using the EXPRESS One-Step Superscript qRT-PCR Kit (Invitrogen, Cat#1178101K). Variations in trans epithelial electrical resistance (DTEER) were measured using a dedicated volt-ohm meter (EVOM2, Epithelial Volt/Ohm Meter for TEER) and expressed as Ohm/cm².

Cell-cell fusion assay

Vero E6 cells were transfected with S protein bearing furin recognition mutation (R682RAR to A682AAR) with C-terminal GFP tag by Lipofectamin 2000 (Invitrogen) and were cultured on m-Slide 8 well chamber slides (Ibidi, Cat#80826). The transfection efficiency was monitored by percentage of GFP positive cells and optimized within 15%–30% to achieve the best signal-to-noise ratio in the following cell-cell fusion assay. After 48 hours, cells were treated with various antibodies diluted in DMEM without FBS for 1 hour at 37C. Cells were then treated with 15 mg/ml trypsin and incubated at 37C for another 2 hours. After trypsin treatment, cells were fixed

with 4% PFA at room temperature for 15 mins and the cell nuclei were stained with DAPI. Images were taken by Olympus confocal microscope.

Fab affinity measurement by BLI

Binding affinity of purified Fab to RBD was measured on the Octet96Red system (ForteBio). Anti-human IgG Fc (AHC) sensors were first loaded with 1 mg/ml of Fc-RBD for 10 min, followed by kinetics buffer (phosphate-buffered saline buffer supplemented with 0.1% Tween-20 and 0.1% BSA) for 5 min to establish a stable baseline. The sensors were then dipped into different concentrations of each Fab from 100 nM to 3.125 nM in two-fold dilutions for 6 min, and then in kinetics buffer again for 10 min to measure association and dissociation. Assays were run at 25°C and data was analyzed on the Octet System Data Acquisition Software version 9.0.0.4. using the 1:1 Langmuir binding model.

Avidity binding by BLI

Avidity of anti-SARS-CoV-2 Spike RBD IgG antibodies for RBD was measured on the Octet96Red system. Anti-hIgG Fc capture (AHC) sensors were used. The sensors were loaded with 1 mg/ml of Fc-RBD (made in-house) in assay buffer (phosphate-buffered saline buffer supplemented with 0.1% Tween-20 and 0.1% BSA) for 10 min, quenched in 0.5 mg/ml of isotype IgG in assay buffer for 10 min, then dipped in assay buffer for 12 min for the system to stabilize. To measure the association of 5A6, the sensors were dipped in a range of 5A6 IgG concentrations (25-0.39 nM in 2-fold serial dilutions) in assay buffer for 6 min. To measure dissociation, the sensors were dipped in assay buffer for 10 min. The experiment was conducted at 25°C. Data analysis was done in the Octet System Data Acquisition Software version 9.0.0.4. using the 1:2 bivalent model.

Epitope binning by BLI

Epitope binning was done using a classical sandwich assay. The AR2G sensor tips (ForteBio) were activated in freshly prepared 20mM EDC (1-ethyl-3-[3-dimethylaminopropyl]-carbodiimide hydrochloride), 10mM NHS (N-hydroxysuccinimide) solution and the 5A6 antibody was immobilized to the sensor tips using a concentration of 7.5 mg/ml of 5A6 in 10 mM sodium acetate pH 6 buffer. After quenching in 1M ethanolamine, the 5A6-immobilized sensor tips were dipped in 5 mg/ml of tagless RBD for 600 s, then in 10mg/ml of the second antibody for 300 s. The assay was run at 25C. Sensor tips were regenerated in 10 mM glycine at pH 2.7 and neutralized in PBS with 0.1% Tween-20 before another cycle of sandwich assay was performed. Each sensor tip was used in a total of 3 cycles. Data analysis was done in the Octet System Data Acquisition Software version 9.0.0.4.

IgG and Fab affinity for Spike trimer by SPR

StreptagII-tagged prefusion S ectodomain, diluted to 10 mg/mL in 10 mM HEPES, 150 mM NaCl, 3 mM EDTA, 0.05% PS-20, pH 7.4, was captured on a StreptactinXT-immobilized (Iba Life Sciences) CM5 Series S sensor chip at an average level of 224 or 347 RU (response units) for IgG and Fab kinetics measurements, respectively using a Biacore T200 (Cytiva Life Sciences). 2-fold serial dilutions of purified IgG from 12.5 nM to 0.39 nM or Fab from 100 nM to 3.125 nM were flowed over the captured prefusion S ectodomain at 30 mL/minute for 90 s followed by 420 s of dissociation flow. Following each cycle, the chip surface was regenerated with 3 M guanidine hydrochloride. The resulting reference flow cell and blank-injection subtracted sensorgrams were fit to a 1:1 Langmuir binding model using the Biacore T200 Evaluation Software (Cytiva Life Sciences).

Statistical analysis

Data were analyzed using GraphPad Prism version 7.03. Statistical tests are indicated in the figure legends. EC50 values were calculated by non-linear regression analysis on the binding curves using GraphPad Prism and IC50 values were calculated either using the [Inhibitor] versus response variable slope four parameter non-linear regression model of GraphPad Prism, or the four parameter logistic regression model in the Quest Graph IC50 Calculator from AAT Bioquest, Inc (<https://www.aatbio.com/tools/ic50-calculator>). One-way analysis of variance (ANOVA) was used to compare differences between groups. Differences were considered statistically significant at confidence levels * $p < 0.05$ or ** $p < 0.01$, *** $p < 0.001$.

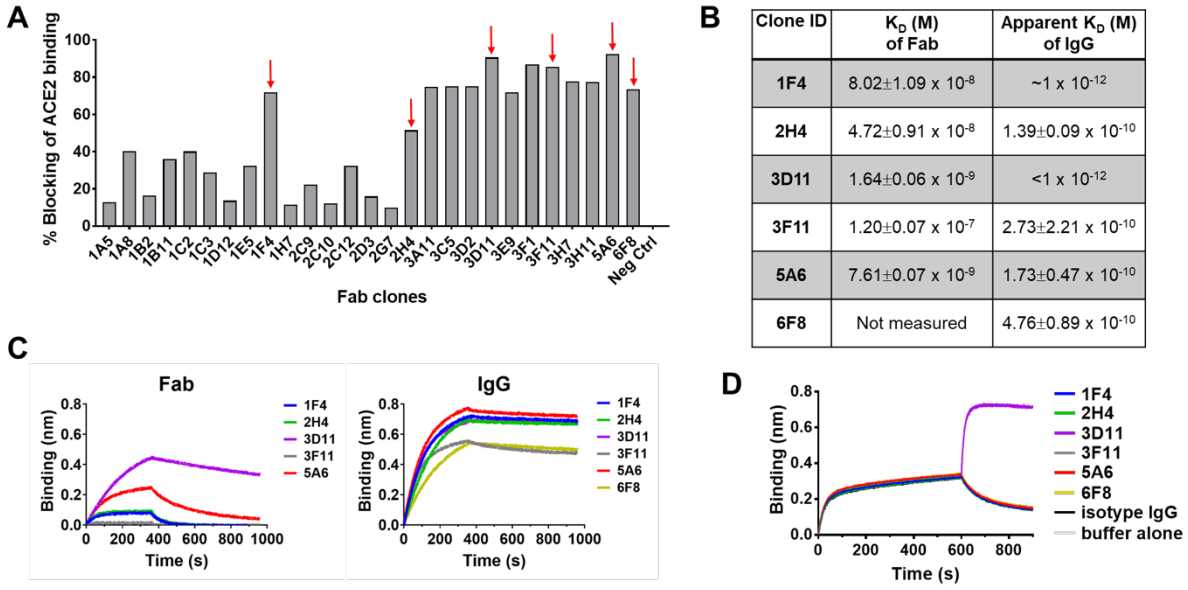


Figure 5.1 | Isolation of SARS-CoV-2 receptor-blocking antibodies from a naïve human library

(A) Blocking of ACE2/RBD (SARS-CoV-2) interactions by 27 Fab clones, tested by competition ELISA. The samples used in the assays were unpurified Fab from bacterial supernatant, hence the percentages of blocking were not indicative of their true potency. Red arrows indicate the 6 clones in subsequent studies.

(B) K_D of Fab based on 1:1 Langmuir fitting and apparent K_D of IgG based on 1:2 bivalent analyte fitting of BLI sensorgrams for immobilized RBD-Fc. Values are the mean and standard deviation of two independent experiments.

(C) Binding and dissociation of Fabs and IgGs to and from immobilized RBD-Fc by BLI. The concentration of Fabs and IgGs shown is 12.5 nM.

(D) Epitope binning of 5A6 by BLI analysis. Buffer alone, an isotype IgG and 5A6 IgG were included as controls.

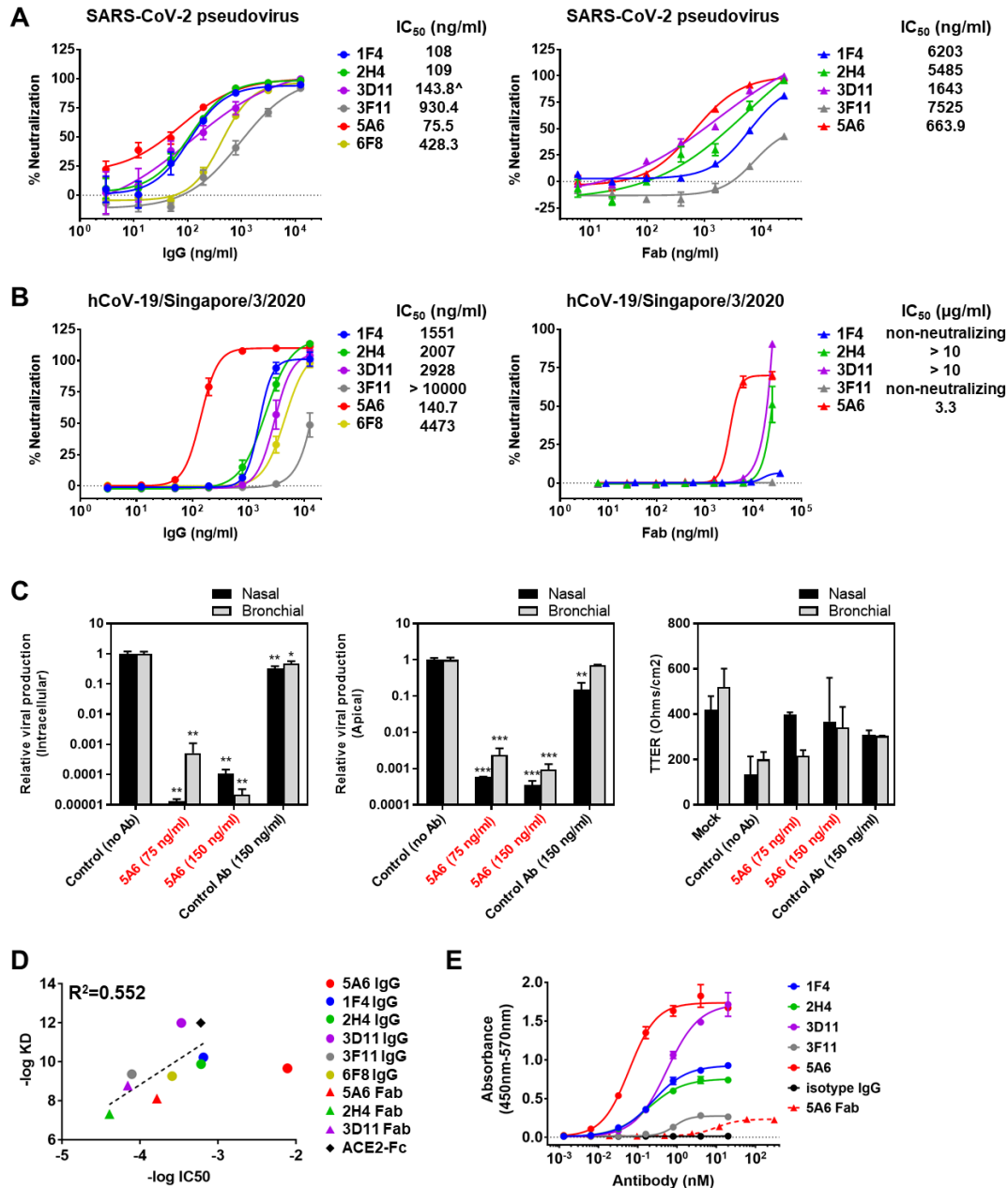


Figure 5.2 | SARS-Cov-2 neutralization by receptor blocking antibodies.

(A) Infection of CHO-ACE2 cells by SARS-CoV-2 pseudovirus were determined in the presence of receptor blocking IgGs (left panel) or Fabs (right panel). Luciferase activities in the CHO-ACE2 cells were measured, and the percent neutralization was calculated. Data are presented as means \pm SEM in triplicates and are representative of two independent experiments. The IC₅₀ was calculated by a variable slope four parameter non-linear regression model using Graphpad PRISM 7 Software, or ([^]) by a four parameter logistic linear regression model using the Quest Graph™ IC₅₀ Calculator from AAT Bioquest, Inc (<https://www.aatbio.com/tools/ic50-calculator>).

(B) Infection of Vero E6 C1008 cells by SARS-CoV-2 live virus (hCoV-19/Singapore/3/2020) were determined in the presence of receptor blocking IgGs (left panel) or Fabs (right panel). Infection induced cytopathic effect was determined by detecting the amount of ATP present in the uninfected live cells from which the percent neutralization was calculated. Data are presented as means \pm SEM in triplicates and are representative of two independent experiments. The IC₅₀ was calculated by a variable slope four parameter non-linear regression model in Graphpad PRISM 7 Software. Pseudo- and live virus neutralization assays were not performed for 6F8 Fab due to 6F8 IgG's low and similar potency to other clones.

(C) Evaluation of antiviral activity of 5A6 in a model of reconstituted human airway epithelia (HAE). Viral genome quantification was performed using RT-qPCR, and results presenting relative viral production (intracellular or apical) are expressed compared to control. Bars represent the means \pm SD in duplicates. *** $P < 0.001$, ** $P < 0.01$ and * $P < 0.05$ compared to the control (no Ab) by one-way ANOVA. The trans-epithelial resistance (TEER in Ω/cm^2) was measured at 48hpi.

(D) Correlation curve of affinity/avidity for RBD and live virus neutralization potency (IC₅₀) of receptor blocking IgG antibodies (circles), Fab antibodies (triangles) and ACE2-Fc (black diamond). The IC₅₀ values were calculated using a four parameter logistic linear regression model in the Quest Graph™ IC₅₀ Calculator from AAT Bioquest, Inc.

(E) Binding of the IgG (solid lines, circles) and 5A6 Fab (dashed line, red triangle) to the purified SARS-CoV-2 pseudovirus.

A

antibody	-	-	5A6 IgG	5A6 Fab	3D11 IgG	2H4 IgG
trypsin	-	+	+	+	+	+

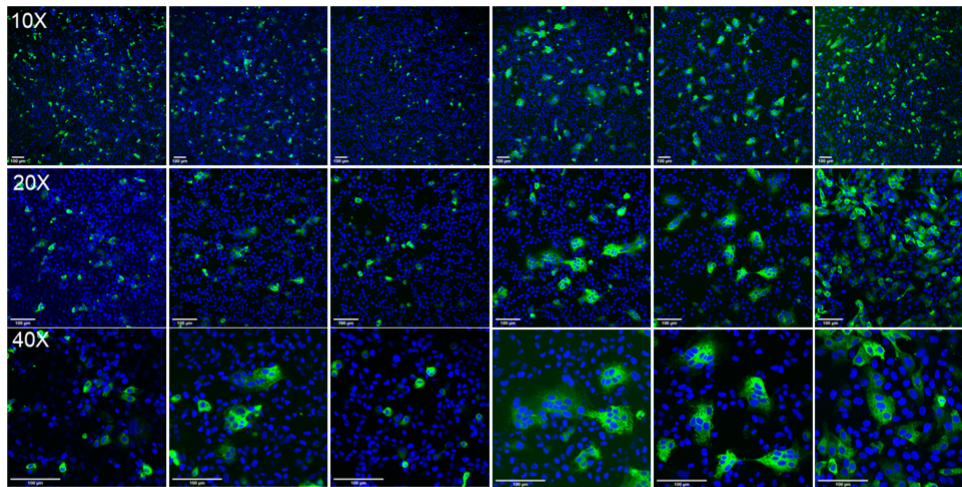
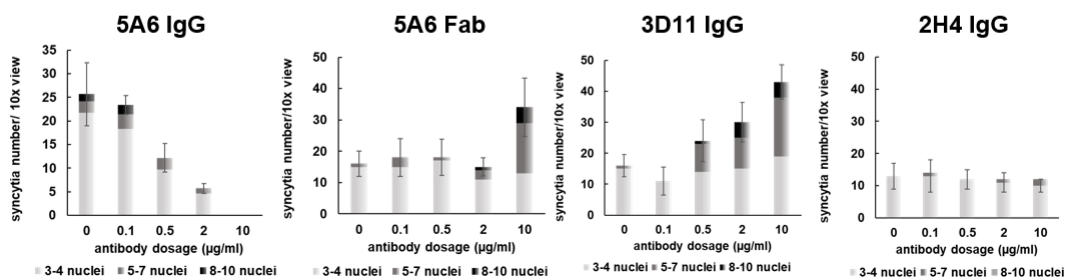
**B**

Figure 5.3 | Anti-SARS-CoV-2 Spike RBD IgG antibodies affect trypsin induced cell syncytia formation.

Vero E6 cells were transfected with furin recognition mutation of SARS-CoV-2 S-protein (R682RAR to A682AAR)-GFP. After 48 hours, the cell culture medium was changed to DMEM (no serum) and treated WT/WO antibodies and incubated for 1 hour at 37°C. The cells were then treated WT/WO trypsin 15 µg/ml for 2 hours at 37°C. Cells were fixed with 4%PFA and stained with DAPI.

(A) 5A6 IgG (20 µg/ml), 5A6 Fab (20 µg/ml), 3D11 IgG (20 µg/ml) and 2H4 IgG (20 µg/ml) treated S-protein expressing Vero E6 cell images in 10x, 20x and 40x objective view. Images were taken by Olympus confocal microscope.

(B) Dosage response of 5A6 IgG, 5A6 Fab, 3D11 IgG and 2H4 IgG. S-protein expressing Vero E6 were treated with 0, 0.1, 0.5, 2, 10 µg/ml of each antibody. 2×10^5 cells/sample were used for transfection of 5A6 IgG dosage response. 1.6×10^5 cells/sample were used for transfection of 5A6 Fab and 3D11 IgG. Data quantification were calculated on syncytia numbers and nuclei number presented in each syncytium.

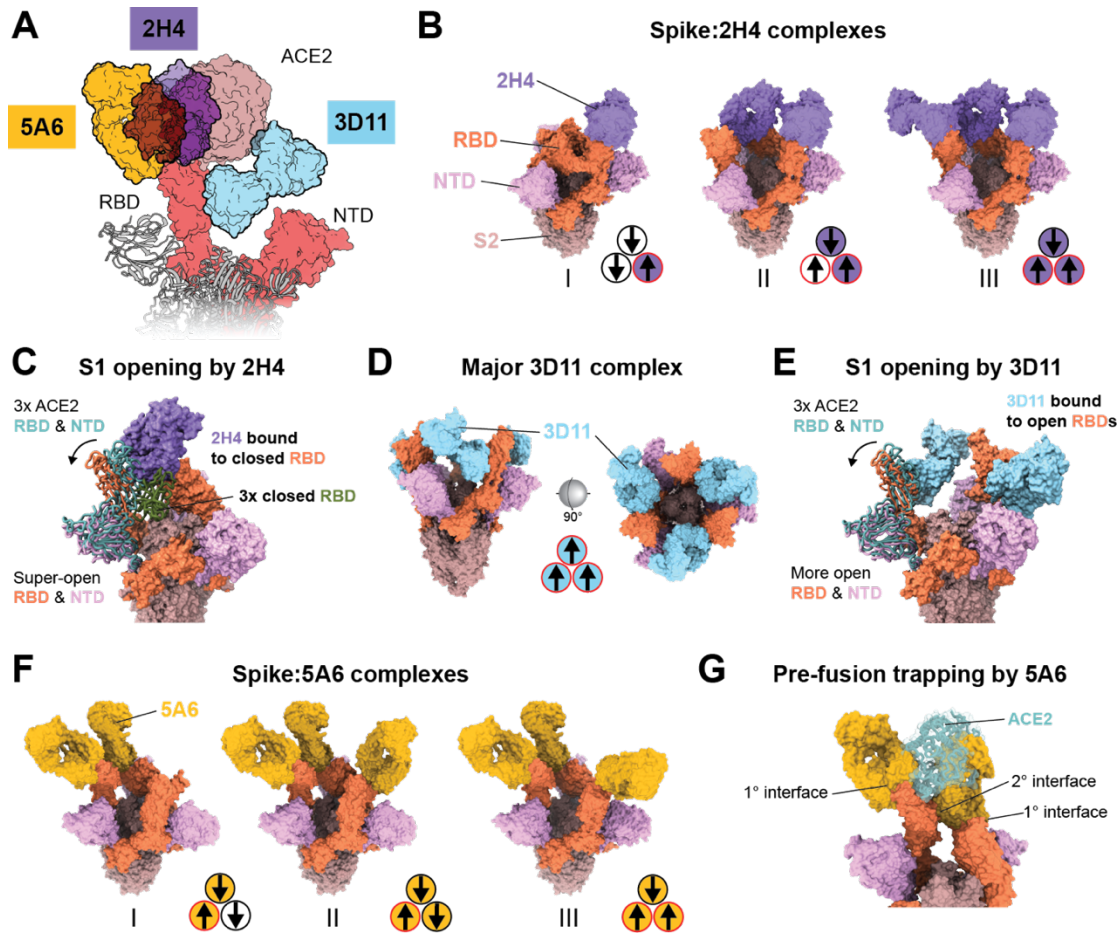


Figure 5.4 | Structures of Spike-Fab complexes

(A) Schematic representation of three Fabs, 5A6 (goldenrod), 2H4 (purple), and 3D11 (sky blue), bound to the SARS-CoV-2 Spike protein. All Fabs are shown in relation to the complex formed by an open RBD (red) and the extracellular domain of ACE2 (rose brown).

(B) Spike:2H4 complexes depicted as surface models, with 2H4 in purple, RBDs in coral, NTDs in plum, and the S2 core in rose brown. A triad of small circles to the lower left of each complex figure represent the three RBDs, with an inset arrow indicating the open (up) or closed (down) conformation, and purple fill indicated a bound Fab. The ensemble of Spike:2H4 complexes is reminiscent of several intermediates in the conformational cycle triggered by serial binding of ACE2.

(C) A cut-away of Spike:2H4 complex II highlighting the steric effect of 2H4 bound to a closed RBD on the counter-clockwise adjacent RBD and NTD. The 2H4-bound RBD clashes with both RBDs from either the fully closed trimer conformation (PDB: 6zgi; dark green) and the fully opened conformation with three ACE2 molecules (PDB: 7a98; cadet blue).

(D) The single major Spike:3D11 complex, colors as in B. (3D11 in sky blue). All RBDs are open, resembling the open trimer bound to three copies of ACE2. At right, the extracellular view along the Spike trimer axis reveals its S2 core essentially unsheathed.

(E) A cut-away of the Spike:3D11 complex showing its effect on the neighboring RBD is similar to that of 2H4, but less pronounced. Colors as in C., 3D11 in sky blue.

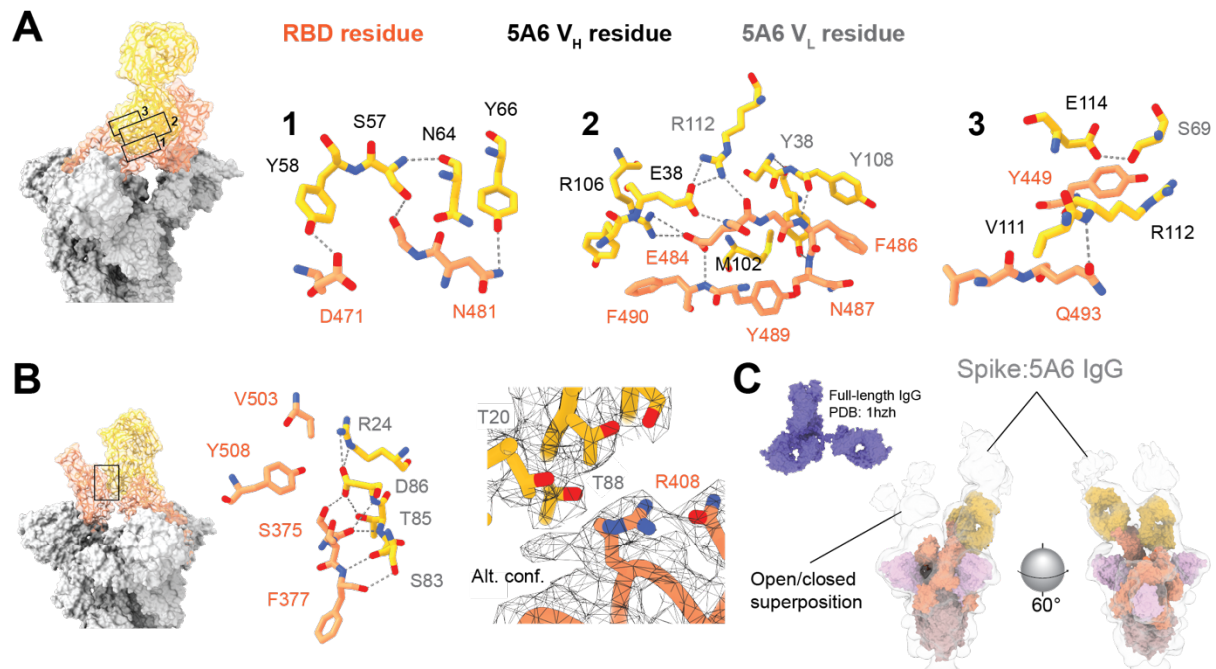


Figure 5.5 | Binding mode and epitope of 5A6

(A) A tour through the primary interface between Spike RBD and 5A6, using three immediately adjacent cross-sections along the viewing axis. Spike residues and labels are colored in coral or by heteroatom, and 5A6 residues are colored goldenrod, with labels for V_H residues in black and V_L residues in gray. Fab residue labels use the IGMT numbering system (Lefranc et al., 2003). Predicted hydrogen bonds are shown as dashed gray lines. The interface features extensive hydrogen bonding, numerous hydrophobic contacts, and multiple salt bridges. A aromatic cluster formed by 5A6 V_L Y38 and Y108, and RBD F486, a salt bridge between 5A6 V_H R98 and RBD E484, and a cation- π interaction between Fab V_H R112 and RBD Y449 are particularly notable.

(B) The secondary interface between 5A6 and the neighboring open RBD comprises mostly hydrogen bonds, many of which involve main-chain atoms. Atom and label colors are as in (A). An interesting feature is stabilization of an alternate conformation of RBD R408 by 5A6 V_L T20 and T88.

(C) Two views of the Spike:5A6 IgG complex cryo-EM map (translucent gray) overlaid on the surface model of Spike:5A6 Fab complex I (colors as in Figure 4). The docked Fab complex model and the IgG complex cryo-EM density reveal a congruent epitope binding geometry in both formats, with two RBDs in the characteristic open/closed trapped conformation. Fc domains are visible as unmodeled blobs to the back of each Fab, and are like a superposition of multiple possible stoichiometries. The third RBD seems to be a superposition of open and closed RBDs with IgG bound. The surface model of a full-length human IgG x-ray crystal structure (PDB: 1hzh) is shown for scale (comparison is facilitated by use of orthographic projection).

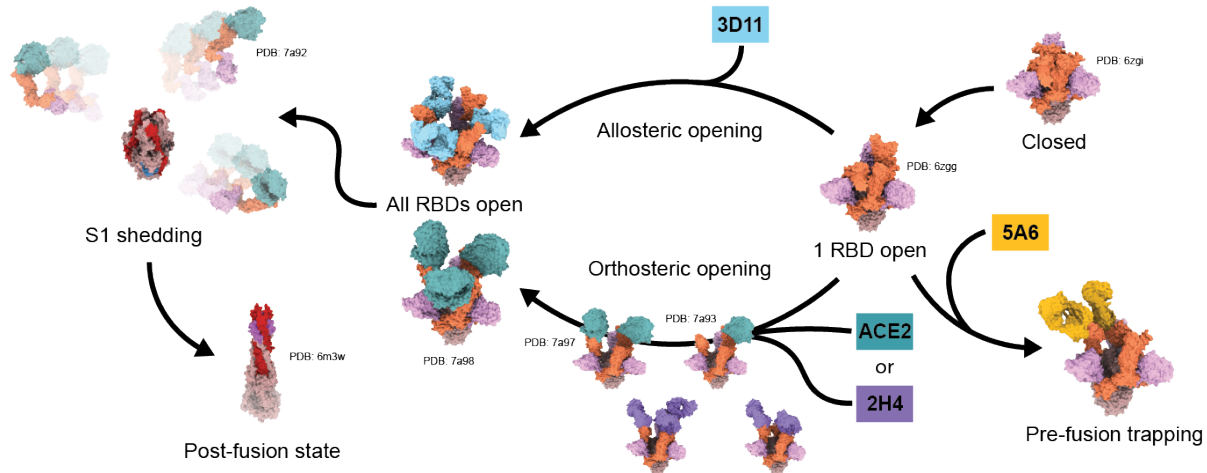


Figure 5.6 | Spike functional modulation by receptor-blocking antibodies

A schematic model representing the possible effects of receptor-blocking antibodies, and ACE2 itself, on the conformational cycle of the SARS-CoV-2 Spike trimer. On the viral surface, the Spike is found predominantly in either the closed conformation, or a “receptor seeking” conformation with one RBD open. When serially bound by ACE2 or an orthosteric mimetic antibody like 2H4, the Spike trimer passes through a series of conformations that eventually permit S1 shedding and the S2 post-fusion transition that mediates membrane fusion. Alternatively, allosteric antibodies such as 3D11 can advance the trimer directly to the end of the opening process, potentiating formation of syncytia through fusion of neighboring cells. Allosteric opening most likely contributes to lower potency in a high-affinity receptor-blocking antibody, and might even suggest the possibility antibody-dependent enhancement of infection. Finally, the Spike might instead be recognized by 5A6, which inhibits membrane fusion and syncytia formation by preventing S1 shedding and trapping the pre-fusion trimer. By enjoining the exposure and conformational transition of the S2 subunit, the 5A6 complex represents an unproductive dead-end for the Spike trimer.

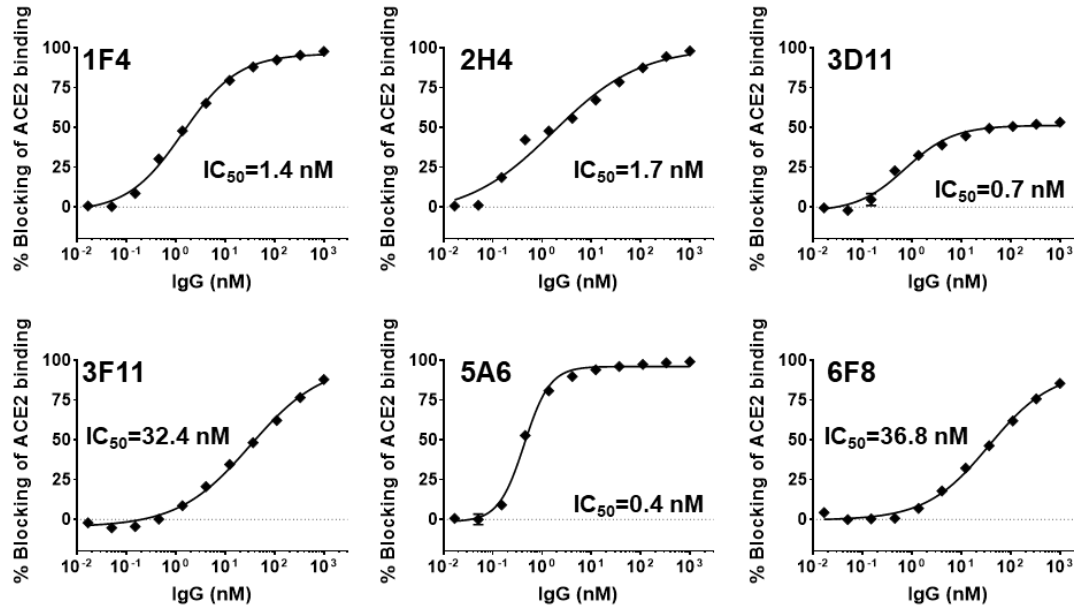


Figure 5.0.7 | Blocking of ACE2/SARS-CoV-2 RBD interaction by 1F4, 2H4, 3D11, 3F11, 5A6 and 6F8 IgGs tested by competition ELISA.

Data are presented as means ± SD in triplicates and are representative of two independent experiments.

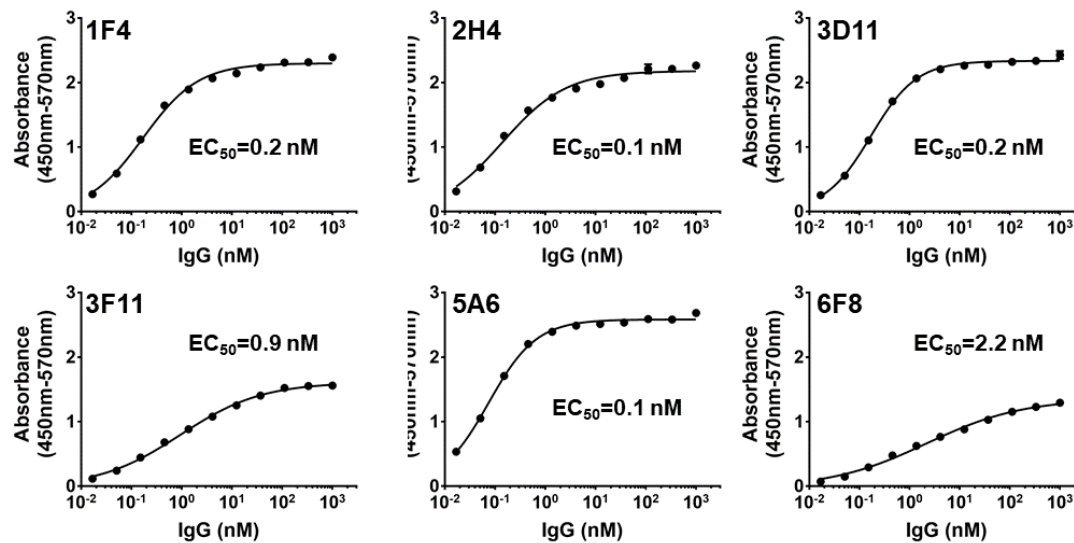


Figure 5.8 | Binding avidity of 1F4, 2H4, 3D11, 3F11, 5A6 and 6F8 IgG antibodies to SARS-CoV-2 Spike RBD proteins tested by ELISA.

Data are presented as means ± SD in triplicates and are representative of two independent experiments.

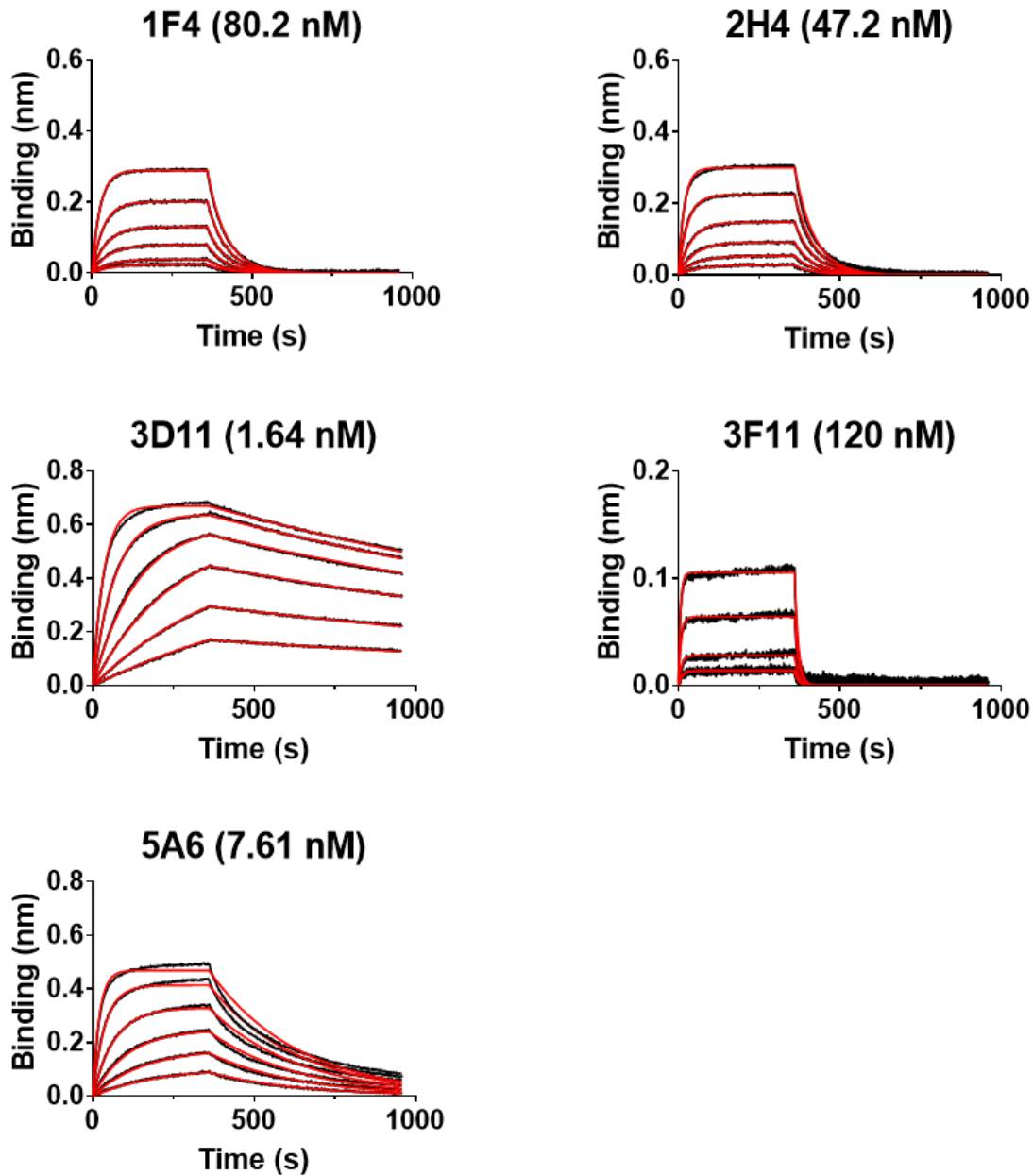


Figure 5.9 | Binding affinity of five Fab clones to SARS-CoV-2 Spike RBD protein measured by biolayer interferometry.

Fab binding to immobilized RBD-Fc was tested using a range of Fab concentrations from 100 nM to 3.125 nM (in 2-fold dilution). A representative set of measurements is shown with sensorgrams in black and curve fittings in red.

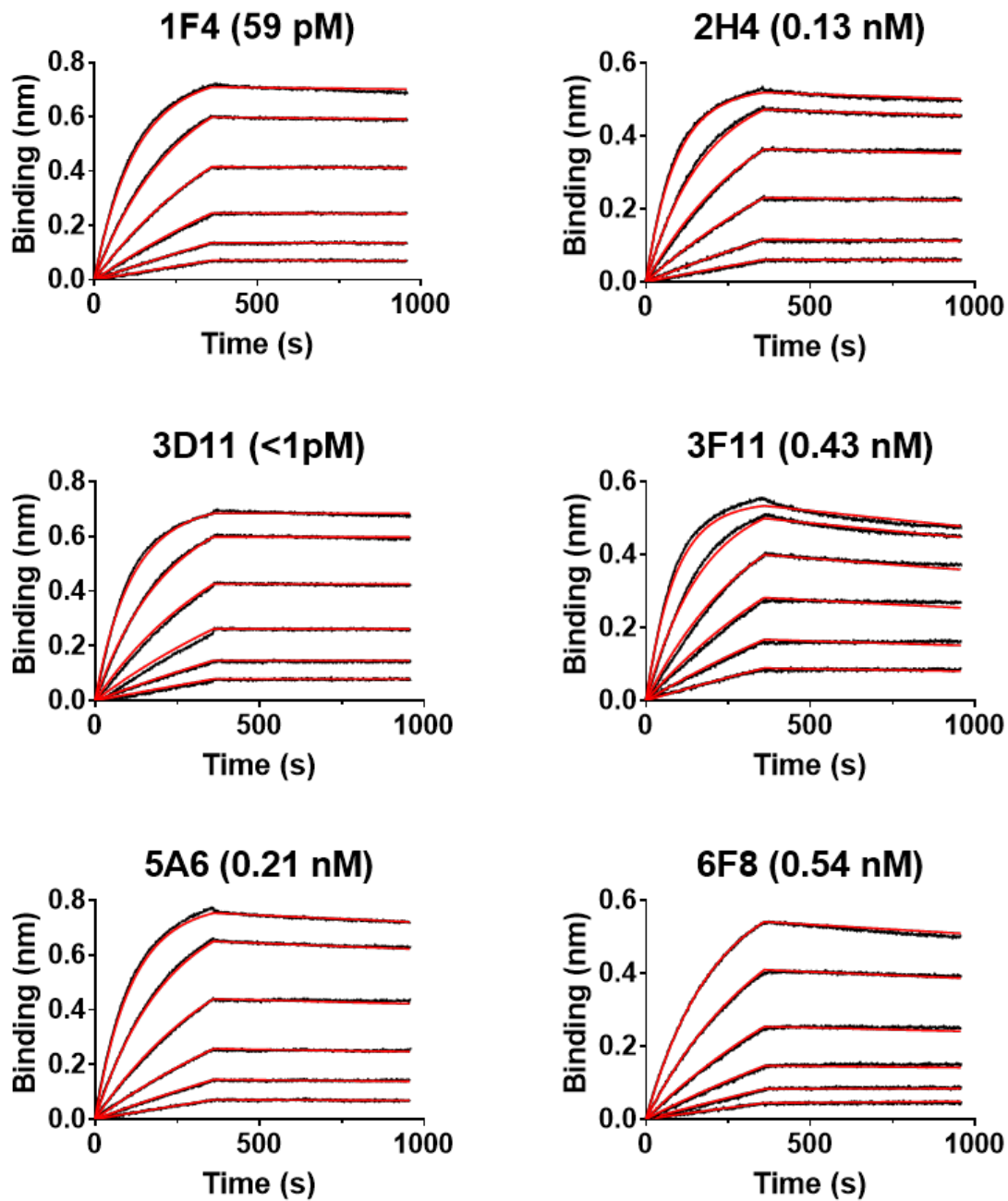


Figure 5.10 | Binding avidity of six IgGs to the RBD by biolayer interferometry.

IgG Binding to immobilized RBD-Fc was tested using a range of IgG concentrations from 12.5 nM to 0.39 nM (in 2-fold dilutions). The anti-Fc sensor chip was quenched with excess irrelevant, same-isotype IgG to prevent confounding from antibody binding directly to the chip. Representative sensorgrams are shown in black, with curve fittings in red.

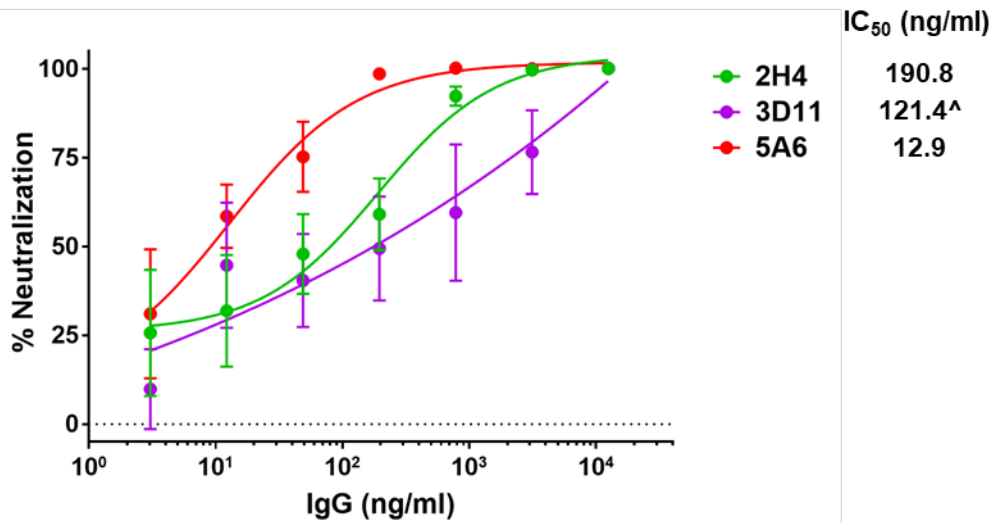


Figure 5.11 | The potency of 2H4, 3D11 and 5A6 IgG antibodies in neutralizing live SARS-CoV-2 virus assays determined by measuring the viral genome copy number (GCN).

Infection of Vero E6 C1008 cells by SARS-CoV-2 live virus (hCoV-19/Singapore/3/2020) were determined in the presence of receptor blocking IgGs 2H4, 3D11 and 5A6. 48 hours post infection, culture supernatant was harvested and viral GCN was determined by RT-qPCR targeting the E gene and GCN values were determined by comparing Ct values against a logGCN standard curve. The GCN values were then converted to percent neutralization and plotted with a non-linear regression curve fit using PRISM. IC₅₀ was calculated by a variable slope four parameter non-linear regression model in Graphpad PRISM 7, or by a four parameter logistic regression model using Quest Graph™ IC₅₀ Calculator from AAT Bioquest, Inc (<https://www.aatbio.com/tools/ic50-calculator>). Data are presented as means ± SEM from 6 replicates.

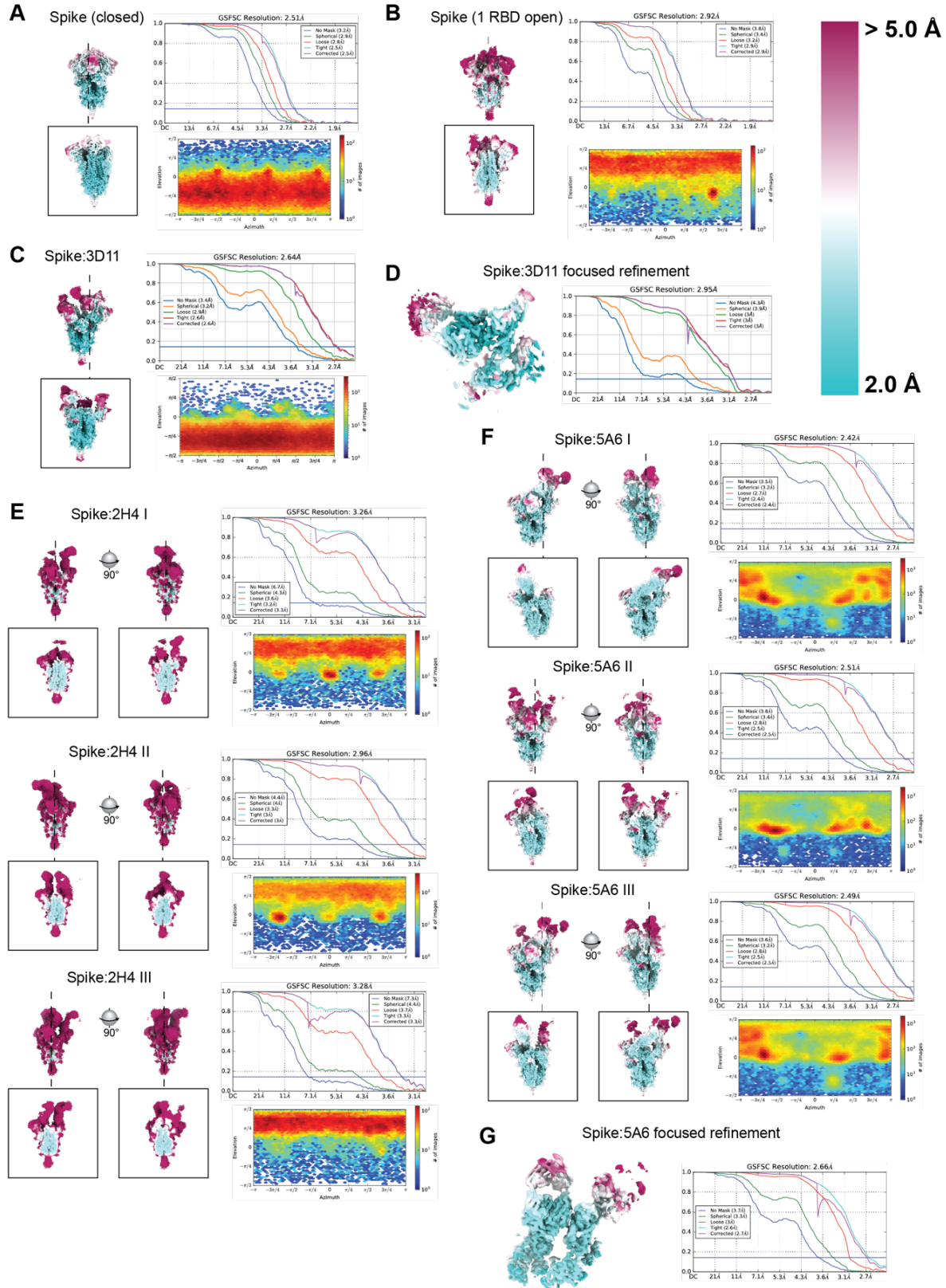


Figure 5.12 | Cryo-EM densities and resolution estimation

Density maps colored by local resolution, Fourier shell correlation curves, and particle orientation distributions for the structures reported in this work. All maps use the same local resolution scale, shown at the top right of the figure.

(A) The apo Spike, with all RBDs closed.

(B) The apo Spike, with one RBD open.

(C) The Spike:3D11 complex.

(D) Refinement of Spike:3D11, focused on the Fab variable domains and RBD epitope.

(E) Spike:2H4 complexes with one, two, or three Fabs bound.

(F) Spike:5A6 complexes.

(G) Refinement of Spike:5A6 complex I, focused on the Fab variable domains and quaternary epitope involving two RBDs (one open, with the clockwise adjacent RBD trapped closed).

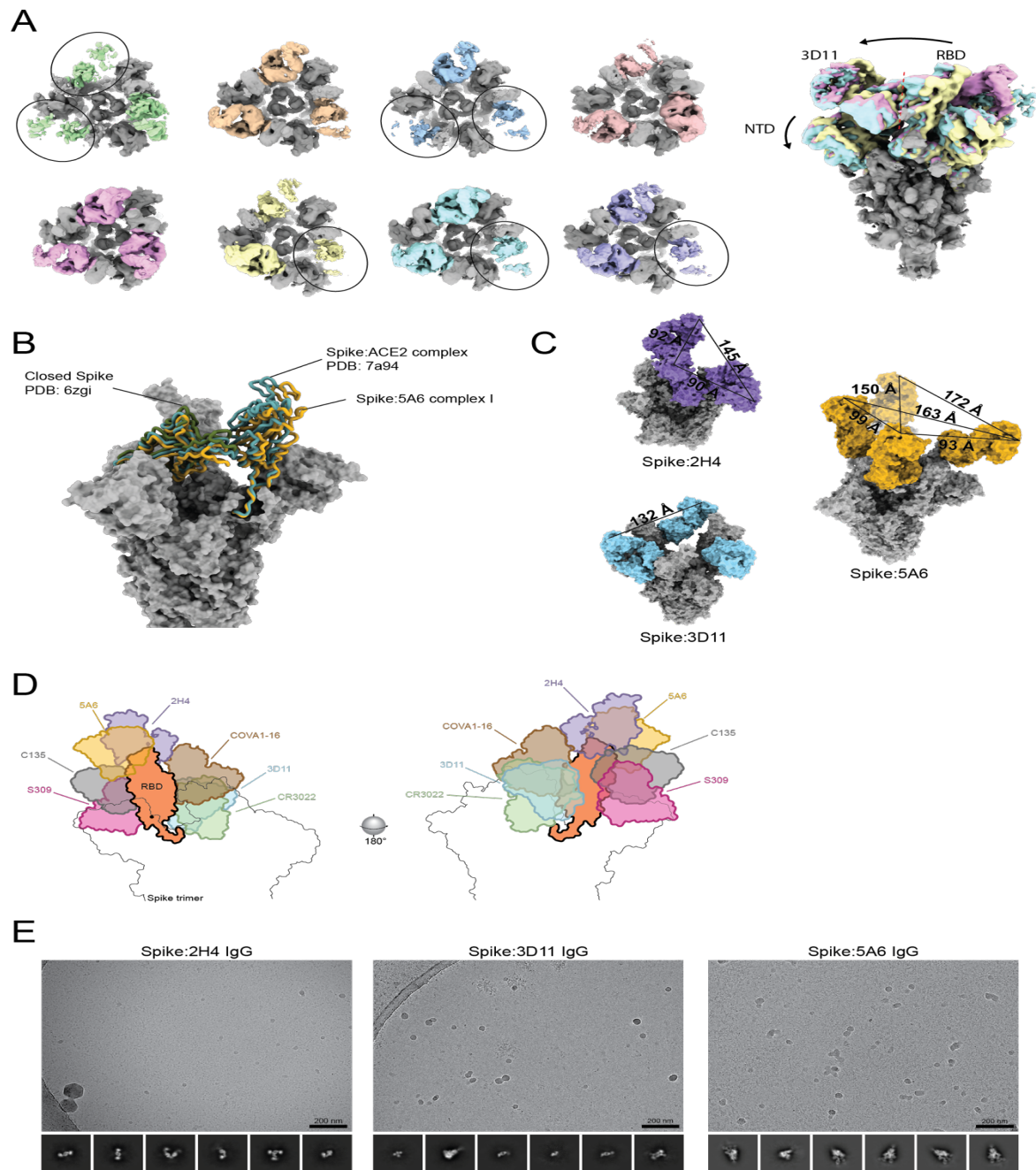


Figure 5.13 | Additional structural details

(A) Eight subclasses of the Spike:3D11 complex, determined using symmetry relaxation in Relion 3.1. At left, top views show that these classes vary in the occupancy of Fab at each RBD. Only Fabs are colored, with missing or weak Fab densities are indicated by black ellipses. At right, two extremum classes and one intermediate show relative motion of the RBDs and NTDs, relaxations which likely contribute to the S2 unsheathing that eventually permits Spike-mediated membrane fusion. Fabs, RBDs, and NTDs are colored, and a dashed line delineates Fab and RBD. The general direction of S2-opening movements, as observed in the classes, are indicated by black arrows.

(B) The quaternary epitope bound by 5A6 is cryptic because the Fab stabilizes unique conformations of RBDs, observed only in the complex, that contribute to the epitope. RBDs from Spike:5A6 complex I (goldenrod) are shown relative to the fully closed Spike (PDB: 6zgi, forest green) and to the Spike with one RBD open and bound to ACE2 (PDB: 7a94, cadet blue). Interestingly, the open RBD bound to 5A6 is more open than that bound to ACE2, yet the neighboring RBD trapped closed by 5A6 is more closed than in the singular ACE2 complex or the fully closed Spike.

(C) The hinge regions connecting the Fc domain of an IgG antibody to each of its two Fabs are 23 residues long, approximately 10 of which are flexible due to disulfide bonds. Assuming a standard polypeptide length of about 3.5 Å per residue, each hinge might extend as far as 35 Å, allowing for some 70 Å separation between the two Fabs. As shown, the shortest gaps between Fabs in the Spike:2H4 and Spike:5A6 complexes are ~90 Å, however variation of the elbow angles between Fab V and C domains could reduce the effective separation. Different Fab clones have elbow angles across just over 90° (Stanfield et al., 2006), and changes as great as 37° have been observed between multiple structures of the same clone (Wilson and Stanfield, 1994). For example, a 15° elbow bend might reduce separation by 10 Å at each Fab (20 Å total), to about the maximum length of the hinge. Bivalent, IgG-bound states thus likely differ in Fab elbow angle and feature some relaxation of the RBDs, in order to support the avid binding of IgG antibodies to Spike trimer observed in our experiments.

D) Comparison of 2H4, 3D11, and 5A6 to non-receptor binding motif antibodies reported in literature. The 2D representation of molecular surface models, with superposed RBDs, shows that C135 and S309 bind to the outward face of the RBD, which is exposed in the closed state, while our antibodies 5A6 and 2H4 bind to the tip of the RBD at epitopes that partially overlap the RBS. Finally, COVA1-16, CR3022, and our 3D11 clone all bind to the inward face of the RBD, which is hidden in the closed state. These last three have overlapping epitopes, but different binding geometries such that, unlike COVA1-16 and 3D11, CR3022 actually clashes severely with the NTD even when the bound RBD is open.

E) Example cryo-EM images and selected 2D class averages for Spike incubated with 2H4 IgG (left), 3D11 IgG (center), or 5A6 IgG (right). Images were collected on a Talos Arctica at 200 keV and low-pass filtered to 20 Å. The Spike:2H4 IgG sample contains numerous, relatively small particles, and some of its 2D class averages resemble monomeric Spike (classes 4 and 6) or two Spike monomers crosslinked by antibody (class 3). In the Spike:3D11 IgG sample, much of the protein is contained within stereotypical aggregates approximately 150 nm in size. Notable 2D averages resemble a Fab bound to Spike RBD (classes 3-5), rare Spike trimers in the closed conformation (class 2), and a potential Spike dimer or pair of monomers crosslinked by antibody (class 6). In contrast to the others, Spike:5A6 IgG is a well behaved sample (despite the crowded micrograph). The 2D class averages are easily recognizable as intact Spike trimer, as is the unique binding mode of 5A6.

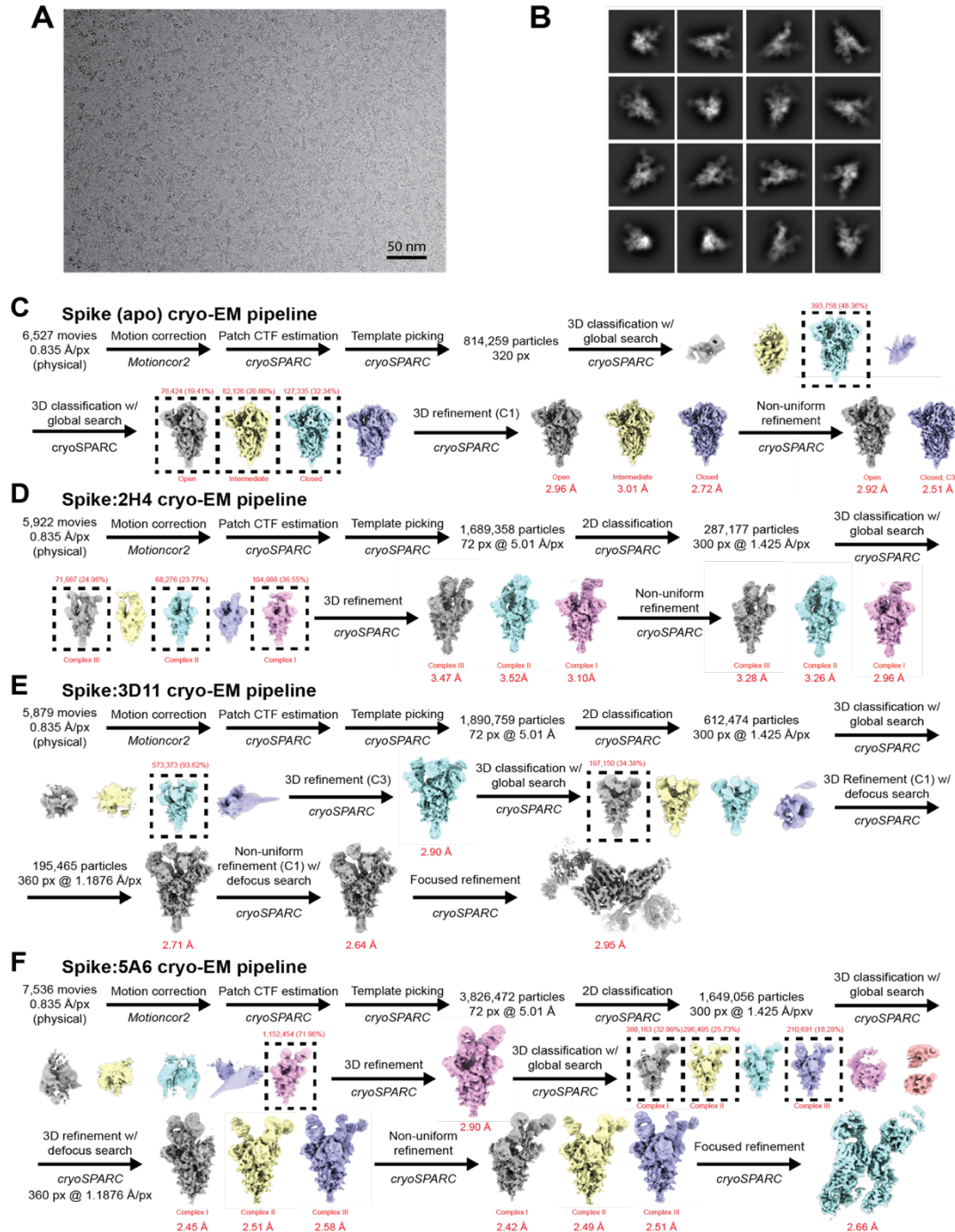


Figure 5.14 | Cryo-EM processing

(A) A micrograph drawn from the Spike:5A6 complex dataset, representative of those obtained for the Fab complexes.

(B) Selected 2D class averages of Spike:5A6 particles, evincing clear secondary structure and multiple Fabs bound to the RBDs.

(C) Cryo-EM image processing workflow for Spike alone, leading to structures of the trimer with all RBDs closed, and with one RBD open or in an intermediate state.

(D) Processing workflow for the Spike:2H4 complex, resulting in structures with one, two, or three Fabs bound, as presented in the text.

(E) Processing workflow for the Spike:3D11 complex, culminating in a high-resolution structure of the Fab and RBD epitope.

(F) Processing workflow for the Spike:5A6 complex, resulting in the complexes presented in the text. Note the fourth class found during the second 3D classification step is a lower resolution duplicate of Spike:5A6 complex III. Processing culminates in a high-resolution of the Fab and its quaternary epitope involving two RBDs.

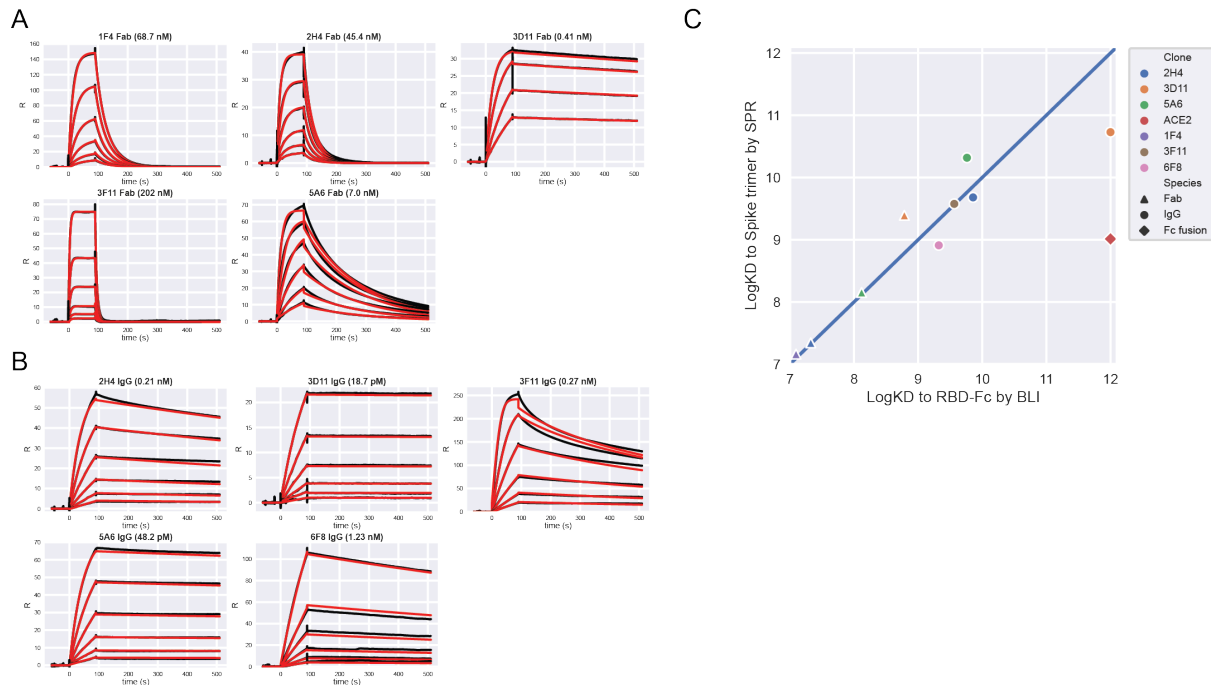


Figure 5.15 | Antibody binding to Spike trimer measured by surface plasmon resonance.

(A) Binding affinity of Fab clones 1F4, 2H4, 3D11, 3D11, and 5A6 for intact Spike trimer measured by SPR. A range of Fab concentrations from 100 nM to 3.125 nM (in 2-fold serial dilution) are shown, with sensorgrams in black and curve fits in red.

(B) Binding avidity of IgG clones 2H4, 3D11, 3F11, 5A6, and 6F8 for intact Spike trimer measured by SPR. A range of IgG concentrations from 12.5 nM to 0.39 nM (in 2-fold serial dilution) are shown, with sensorgrams in black and curve fits in red.

(C) Log-log scatter plot comparing antibody binding constants for RBD-Fc (X axis) to those for Spike trimer (Y axis). Affinity or avidity of antibodies or Fab fragments for the flexible RBD-Fc construct represent binding without geometric constraints, while measurements using immobilized Spike trimers represent binding with the specific geometries afforded by the Spike:antibody complexes. For most species, SPR and BLI measurements are similar, however 3D11 IgG and ACE2-Fc bind significantly more weakly to relatively unrestricted RBD-Fc than to Spike trimer (note that the 3D11 IgG binds >10x more tightly than 3D11 Fab in both sets of experiments, indicating avid binding). 5A6 IgG binds somewhat more tightly to Spike trimer than to RBD-Fc, perhaps indicating that RBDs within a Spike trimer have particularly favorable geometries for binding.

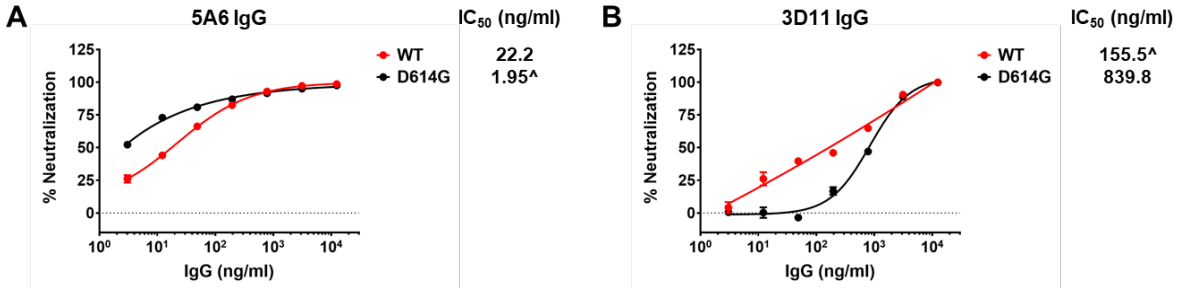


Figure 5.16 | Neutralization of the SARS-CoV-2 pseudovirus with Spike mutant D614G.

A) Neutralization by 5A6 of SARS-CoV-2 pseudovirus bearing either wild-type Spike protein (red), or Spike with the D614G mutation (black). The efficacy of 5A6 IgG is against D614G mutant Spike is improved over wild-type.

B) Neutralization by 3D11 of SARS-CoV-2 pseudovirus bearing either wild-type Spike protein (red), or Spike with the D614G mutation (black). 3D11 IgG suffers a severe loss of efficacy against the mutant pseudovirus (more than 5-fold weaker IC₅₀).

Data are presented as means ± SEM in triplicates and are representative of two independent experiments. IC₅₀ was calculated by variable slope four parameter non-linear regression model using Graphpad PRISM 7 Software or ([^]) by four parameter logistic linear regression model using Quest Graph™ IC₅₀ Calculator from AAT Bioquest, Inc (<https://www.aatbio.com/tools/ic50-calculator>).

5.6 References

1. Tortorici, M. A. & Veesler, D. Structural insights into coronavirus entry. *Adv. Virus Res.* **105**, 93–116 (1 2019).
2. Benton, D. J. *et al.* Receptor binding and priming of the spike protein of SARS-CoV-2 for membrane fusion. *Nature* **588**, 327–330 (12 2020).
3. Hoffmann, M. *et al.* SARS-CoV-2 Cell Entry Depends on ACE2 and TMPRSS2 and Is Blocked by a Clinically Proven Protease Inhibitor. *Cell* **181**, 271-280.e8 (2020).
4. Walls, A. C. *et al.* Structure, Function, and Antigenicity of the SARS-CoV-2 Spike Glycoprotein. *Cell* **181**, 281-292.e6 (4 2020).
5. Zhou, P. *et al.* A pneumonia outbreak associated with a new coronavirus of probable bat origin. *Nature* **579**, 270–273 (3 2020).
6. Lan, J. *et al.* Structure of the SARS-CoV-2 spike receptor-binding domain bound to the ACE2 receptor. *Nature* **581**, 215–220 (5 2020).
7. Tai, W. *et al.* Characterization of the receptor-binding domain (RBD) of 2019 novel coronavirus: implication for development of RBD protein as a viral attachment inhibitor and vaccine. *Cellular and Molecular Immunology* **17**, 613–620 (6 2020).
8. Musarrat, F. *et al.* The anti-HIV drug nelfinavir mesylate (Viracept) is a potent inhibitor of cell fusion caused by the SARSCoV-2 spike (S) glycoprotein warranting further evaluation as an antiviral against COVID-19 infections. *J. Med. Virol.* **92**, 2087–2095 (10 2020).
9. Shulla Ana *et al.* A Transmembrane Serine Protease Is Linked to the Severe Acute Respiratory Syndrome Coronavirus Receptor and Activates Virus Entry. *J. Virol.* **85**, 873–882 (2011).

10. Bussani, R. *et al.* Persistence of viral RNA, pneumocyte syncytia and thrombosis are hallmarks of advanced COVID-19 pathology. *EBioMedicine* **61**, (11 2020).
11. Xu, Z. *et al.* Pathological findings of COVID-19 associated with acute respiratory distress syndrome. *The Lancet Respiratory Medicine* **8**, 420–422 (4 2020).
12. Schneider, J. *et al.* SARS-CoV-2 direct cardiac damage through spike-mediated cardiomyocyte fusion. (2020) doi:10.21203/rs.3.rs-95587/v1.
13. Zhou, G. & Zhao, Q. Perspectives on therapeutic neutralizing antibodies against the novel coronavirus sars-cov-2. *Int. J. Biol. Sci.* **16**, 1718–1723 (2020).
14. Hansen, J. *et al.* Studies in humanized mice and convalescent humans yield a SARS-CoV-2 antibody cocktail. *Science* **369**, 1010–1014 (8 2020).
15. Wang, C. *et al.* A human monoclonal antibody blocking SARS-CoV-2 infection. *Nat. Commun.* **11**, 2251 (2020).
16. Wrapp, D. *et al.* Structural Basis for Potent Neutralization of Betacoronaviruses by Single-Domain Camelid Antibodies. *Cell* **181**, 1004-1015.e15 (5 2020).
17. Brouwer, P. J. M. *et al.* Potent neutralizing antibodies from COVID-19 patients define multiple targets of vulnerability. *Science* **369**, 643–650 (8 2020).
18. Cao, Y. *et al.* Potent Neutralizing Antibodies against SARS-CoV-2 Identified by High-Throughput Single-Cell Sequencing of Convalescent Patients' B Cells. *Cell* **182**, 73-84.e16 (7 2020).
19. Chi, X. *et al.* A neutralizing human antibody binds to the N-terminal domain of the Spike protein of SARS-CoV-2. *Science* **369**, 650–655 (8 2020).
20. Ju, B. *et al.* Human neutralizing antibodies elicited by SARS-CoV-2 infection. *Nature* **584**, 115–119 (8 2020).

21. Rogers, T. F. *et al.* Isolation of potent SARS-CoV-2 neutralizing antibodies and protection from disease in a small animal model. *Science* **369**, 956–963 (8 2020).
22. Shi, R. *et al.* A human neutralizing antibody targets the receptor-binding site of SARS-CoV-2. *Nature* **584**, 120–124 (8 2020).
23. Wan, J. *et al.* Human-IgG-Neutralizing Monoclonal Antibodies Block the SARS-CoV-2 Infection. *Cell Rep.* **32**, (7 2020).
24. Wu, Y. *et al.* A noncompeting pair of human neutralizing antibodies block COVID-19 virus binding to its receptor ACE2. *Science* **368**, 1274–1278 (6 2020).
25. Lou, Y. *et al.* Cross-neutralization antibodies against SARS-CoV-2 and RBD mutations from convalescent patient antibody libraries. *bioRxiv* 2020.06.06.137513 (2020)
doi:10.1101/2020.06.06.137513.
26. Pinto, D. *et al.* Cross-neutralization of SARS-CoV-2 by a human monoclonal SARS-CoV antibody. *Nature* **583**, 290–295 (7 2020).
27. Huo, J. *et al.* Neutralization of SARS-CoV-2 by Destruction of the Prefusion Spike. *Cell Host Microbe* **28**, 445-454.e6 (9 2020).
28. Frenzel, A. *et al.* Designing Human Antibodies by Phage Display. *Transfus. Med. Hemother.* **44**, 312–318 (9 2017).
29. Lu, R.-M. *et al.* Development of therapeutic antibodies for the treatment of diseases. *J. Biomed. Sci.* **27**, 1 (2020).
30. Vaughan, T. J., Osbourn, J. K. & Tempest, P. R. Human antibodies by design. *Nat. Biotechnol.* **16**, 535–539 (1998).
31. Saphire, E. O. *et al.* Structural insight into SARS-CoV-2 neutralizing antibodies and modulation of syncytia - ScienceDirect. *Cell* **174**, 938-952.e13 (8 2018).

32. Goh, A. X. H. *et al.* A novel human anti-interleukin-1 β neutralizing monoclonal antibody showing in vivo efficacy. *MAbs* **6**, 765–773 (2014).
33. Young, B. E. *et al.* Epidemiologic Features and Clinical Course of Patients Infected with SARS-CoV-2 in Singapore. *JAMA - Journal of the American Medical Association* **323**, 1488–1494 (4 2020).
34. Pizzorno, A. *et al.* Characterization and Treatment of SARS-CoV-2 in Nasal and Bronchial Human Airway Epithelia. *Cell Reports Medicine* **1**, (7 2020).
35. Burton, D. R., Saphire, E. O. & Parren, P. W. H. I. A model for neutralization of viruses based on antibody coating of the virion surface. *Curr. Top. Microbiol. Immunol.* **260**, 109–143 (2001).
36. Dowd, K. A. & Pierson, T. C. Antibody-mediated neutralization of flaviviruses: A reductionist view. *Virology* **411**, 306–315 (3 2011).
37. Flamand, A., Raux, H., Gaudin, Y. & Ruigrok, R. B. H. Mechanisms of rabies virus neutralization. *Virology* **194**, 302–313 (1993).
38. McNamara, P. S. & Smyth, R. L. The pathogenesis of respiratory syncytial virus disease in childhood. *Br. Med. Bull.* **61**, 13–28 (2002).
39. Koot, M. *et al.* Prognostic value of HIV-1 syncytium-inducing phenotype for rate of CD4+ cell depletion and progression to AIDS. *Ann. Intern. Med.* **118**, 681–688 (5 1993).
40. Sylwester, A., Murphy, S., Shutt, D. & Soll, D. R. HIV-induced T cell syncytia are self-perpetuating and the primary cause of T cell death in culture. *J. Immunol.* **158**, 3996–4007 (1997).
41. Yurkovetskiy, L. *et al.* Structural and Functional Analysis of the D614G SARS-CoV-2 Spike Protein Variant. *Cell* **183**, 739-751.e8 (10 2020).

42. Punjani, A. & Fleet, D. J. 3D variability analysis: Resolving continuous flexibility and discrete heterogeneity from single particle cryo-EM. *J. Struct. Biol.* **213**, (6 2021).
43. Walls, A. C. *et al.* Unexpected Receptor Functional Mimicry Elucidates Activation of Coronavirus Fusion. *Cell* **176**, 1026-1039.e15 (2 2019).
44. Liu, H. *et al.* Cross-Neutralization of a SARS-CoV-2 Antibody to a Functionally Conserved Site Is Mediated by Avidity. *Immunity* **53**, 1272-1280.e5 (12 2020).
45. Yuan, M. *et al.* A highly conserved cryptic epitope in the receptor binding domains of SARS-CoV-2 and SARS-CoV. *Science* **368**, 630–633 (5 2020).
46. Barnes, C. O. *et al.* SARS-CoV-2 neutralizing antibody structures inform therapeutic strategies. *Nature* **588**, 682–687 (12 2020).
47. Korber, B. *et al.* Tracking Changes in SARS-CoV-2 Spike: Evidence that D614G Increases Infectivity of the COVID-19 Virus. *Cell* **182**, 812-827.e19 (8 2020).
48. Vauquelin, G. & Charlton, S. J. Exploring avidity: Understanding the potential gains in functional affinity and target residence time of bivalent and heterobivalent ligands. *Br. J. Pharmacol.* **168**, 1771–1785 (4 2013).
49. Zhang, L. *et al.* SARS-CoV-2 spike-protein D614G mutation increases virion spike density and infectivity. *Nat. Commun.* **11**, 6013 (2020).
50. Huang, K., Incognito, L., Cheng, X., Ulbrandt, N. D. & Wu, H. Respiratory syncytial virus-neutralizing monoclonal antibodies motavizumab and palivizumab inhibit fusion. *J. Virol.* **84**, 8132–8140 (2010).
51. Mastronarde, D. N. Automated electron microscope tomography using robust prediction of specimen movements. *J. Struct. Biol.* **152**, 36–51 (10 2005).

52. Zheng, S. Q. *et al.* MotionCor2: Anisotropic correction of beam-induced motion for improved cryo-electron microscopy. *Nat. Methods* **14**, 331–332 (2017).
53. Punjani, A., Rubinstein, J. L., Fleet, D. J. & Brubaker, M. A. CryoSPARC: Algorithms for rapid unsupervised cryo-EM structure determination. *Nat. Methods* **14**, 290–296 (2 2017).
54. Webb, B. & Sali, A. Comparative Protein Structure Modeling Using MODELLER. *Curr. Protoc. Bioinformatics* **54**, 5.6.1-5.6.37 (2016).
55. Pettersen, E. F. *et al.* UCSF Chimera--a visualization system for exploratory research and analysis. *J. Comput. Chem.* **25**, 1605–1612 (2004).
56. Goddard, T. D. *et al.* UCSF ChimeraX: Meeting modern challenges in visualization and analysis. *Protein Sci.* **27**, 14–25 (1 2018).
57. Croll, T. I. ISOLDE: A physically realistic environment for model building into low-resolution electron-density maps. *Acta Crystallographica Section D: Structural Biology* **74**, 519–530 (6 2018).
58. Afonine, P. V. *et al.* Real-space refinement in PHENIX for cryo-EM and crystallography. *Acta Crystallographica Section D: Structural Biology* **74**, 531–544 (6 2018).

Publishing Agreement

It is the policy of the University to encourage open access and broad distribution of all theses, dissertations, and manuscripts. The Graduate Division will facilitate the distribution of UCSF theses, dissertations, and manuscripts to the UCSF Library for open access and distribution. UCSF will make such theses, dissertations, and manuscripts accessible to the public and will take reasonable steps to preserve these works in perpetuity.

I hereby grant the non-exclusive, perpetual right to The Regents of the University of California to reproduce, publicly display, distribute, preserve, and publish copies of my thesis, dissertation, or manuscript in any form or media, now existing or later derived, including access online for teaching, research, and public service purposes.

DocuSigned by:

Beatrice Any

87BFF8C2870042C...

Author Signature

3/14/2022

Date